Supporting and Augmenting Experimental Observation via ab initio Quantum Chemistry

by

Henry Mull

(Under the Direction of Henry Schaefer III)

Abstract

Ab initio quantum chemistry provides many benefits to experimental studies through verification and prediction of experimental results. Several examples are given of quantum chemistry methods being used to direct experimental discovery. Through canonical transition state theory, methylamine was found to have greater reactivity with the simplest, *anti*-methylated, and *syn*-methylated Criegee intermediates relative to more abundant atmospheric species. This was true for both addition orientations, but the naturally low concentration of methylamine makes it unlikely to be an important contributor to the consumption of Criegee intermediates under typical conditions. The kinetics of pentazole decomposition were also investigated to determine its potential as a high-energy-density material. A decomposition barrier of 18.8 kcal mol^{-1} makes it unsuitable as an HEDM candidate at room temperature. A temperature of 180 K or lower is required to achieve a half-life of 35 years. Anharmonic frequencies were calculated for four In_2H_2 isomers and their deuterated counterparts. Numerous agreements and some disagreements were found between our results and those of previous studies. Each of these theoretical studies either provided insight for future experimental discovery or sought to verify current data.

Index Words: Quantum Chemistry, *Ab Initio* Methods, Criegee Intermediates, Pentazole, Indium Hydrides

Supporting and Augmenting Experimental Observation via ab initio Quantum Chemistry

by

Henry Mull

B.S., California Polytechnic State University, San Luis Obispo, 2019

A Dissertation Submitted to the Graduate Faculty of The University of Georgia in Partial

Fulfillment of the Requirements for the Degree

Doctor of Philosophy

Athens, Georgia

2023

Supporting and Augmenting Experimental Observation via ab initio Quantum Chemistry

by

Henry Mull

Major Professor: Henry Schaefer III

Committee: Steven Wheeler
Susanne Ullrich

Electronic version approved:

Ron Wolcott
Vice Provost for Graduate Education and Dean of the Graduate School
The University of Georgia
May 2023

Dedication

This dissertation is dedicated to my family and friends who watched me drag myself through graduate school, especially to Mom and Dad for your endless support throughout the entirety of my life and my academic career, and to Emily for being my closest companion, confidant, and source of inspiration. Thank you all for the love and support you have given me.

Acknowledgements

I would like to thank my advisor, Dr. Schaefer, for his support in my research and the community he cultivated in his research group. Additional thanks must also be given to Dr. Turney, without whom my research would be fraught with many more questions. To the members of the CCQC, thank you for your constant support and even more so for your constant criticism.

I would also like to thank my committee for their time and their feedback to help me become a more well-rounded scientist.

Finally, I must express endless gratitude to Emily Wearing for helping me become a better scientist as well as making sure I met all my deadlines.

Table of Contents

Chapter 1

Introduction

Over the last century, quantum chemistry has become and indispensable field of study to the larger chemistry community. From its humble beginnings as a controversial theory and through its contentious development, quantum chemistry has taken its place as a proper sub-discipline of chemistry. It allows us to rationalize and understand the most fundamental properties of matter and energy through a combination of physics, mathematics, and chemistry. On its own, quantum chemistry provides useful insight, though sometimes it may be unclear or unintuitive; however, much of its worth is found in collaboration with experiment. Even the most elegant and rigorous theory will remain questionable until it can be proven with experimental data. In the early stages of quantum chemistry, this collaboration was only achievable for the smallest and simplest of systems. Now, quantum chemistry methods are used in a wide variety of applications to both support experimental evidence as well as make predictions about yet unstudied systems.

One of the most important ways in which quantum chemistry is used towards this end is calculating spectroscopic data. Many different realms of spectroscopy can benefit from the additional confirmation of their peak assignments from quantum mechanical frequency calculations.[1–3] Such calculations are useful for both helping to identify peaks from complicated spectra as well as understanding splitting patterns. This is particularly true in the case of astrochemistry,[4] as the low-density, low-temperature conditions of the interstellar medium are well represented by typical quantum chemistry calculations. Due to the nature of the calculations involved, high-accuracy frequency calculations faced many barriers and limitations for large or complex molecules, but modern techniques[5] seek to reduce many of these hurdles.

While less directly related, the quality of theoretical kinetic information is largely dependent on the accuracy of the methods used to determine the energetics of the system. In this sense, high-level *ab initio* quantum chemistry methods are essential to obtain reliable rate constants.[6] A calculated rate constant increases exponentially with an increasing barrier height, so even a small difference in the energy barrier of a reaction can result in a significant change in the rate constant. Quantum chemistry methods are especially needed for kinetic systems with thousands of interconnected reactions, many of which may be impossible to directly measure.[7] These methods can also be utilized for enzyme studies[8] where a detailed understanding of the catalysis mechanism is required to make sense of the resulting kinetics, though for large biological systems, the methods used are often a mix of *ab initio* and approximate methods for the sake of feasibility.

Perhaps supporting experimental observations is the most common role of quantum chemistry, but occasionally theory may support a different result than that which has been put forward by experimentalists. In these cases, quantum chemistry calculations suggest alternatives to, or even contradict, the established experimental results. A particularly well-known example is the controversy over the bond angle of methylene,[9,10] where *ab initio* calculations consistently suggested a bent structure rather than the linear structure championed by experimentalists. These claims faced significant criticism at the time, but now they mark a shift in perspective which brought theoretical chemistry into a similar prestige as experiment. This was not an isolated incident, and time proved other theoretical results to be more accurate than their experimental counterparts.[11–13] Beyond merely just acting as a support for experiment, quantum chemistry plays a role in both leading experimental discovery as well as verifying the reliability of experimental data.

Here, three computational chemistry studies are presented, all of which sought to provide new information and insight towards the properties of specific molecules to

develop deeper understanding of current or future experimental observations. First, the role of atmospheric methylamine in the consumption of Criegee intermediate will be investigated through the calculation of rate constants and comparison to other atmospheric species. Next, the potential of pentazole as a high-energy-density material will be determined by calculating the energetics of the decomposition pathway. Finally, the discrepancies between the IR peaks of indium dihydride isomers from two separate studies will be resolved via the calculation of anharmonic frequencies. In each of these cases, *ab initio* quantum chemistry methods will be used to calculate the basic properties of the molecules involved. With these calculations as a basis, predictions about the experimental bulk properties of the molecules can be made.

Chapter 2

Theory

The discussion in this chapter revolves around the theory used in various quantum chemistry methods. Much of this information can be found expanded upon in numerous texts. Unless otherwise noted by a citation, the information presented here is specifically cited from a few texts.[14–16] For electronic structure methods, see *Modern Quantum Chemistry* by Attila Szabo and Neil S. Ostlund and *Molecular Electronic-Structure Theory* by Trygve Helgaker, Poul Jørgensen and Jeppe Olsen. For kinetics and statistical mechanics, see *Statistical Mechanics* by Donald A. McQuarrie.

2.1 Hartree-Fock Theory

Hartree-Fock (HF) theory is the simplest form of *ab initio* method for calculating the electronic energy of a molecule and serves as the basis for many extended theories which incorporate correlation. The goal of HF theory is to solve the time-independent Schrödinger equation.

$$\hat{H}\,|\Psi\rangle = E\,|\Psi\rangle \tag{2.1}$$

The Hamiltonian can be separated into constituent operators which correspond to classical energy equations. This includes the kinetic energy of both the electrons and the nuclei as well as the pair-wise potential energy for the electron-electron repulsion, the nuclear repulsion, and the electron-nuclear attraction terms. In total, the Hamiltonian can be written as

$$\hat{H} = -\frac{1}{2}\sum_i \nabla_i^2 - \frac{1}{2}\sum_A \nabla_A^2 - \sum_{iA} \frac{Z_A}{\mathbf{R}_A - \mathbf{r}_i} + \sum_{i<j} \frac{1}{\mathbf{r}_{ij}} + \sum_{A<B} \frac{Z_A Z_b}{\mathbf{R}_{AB}} \tag{2.2}$$

where i and j represent indices for electrons and A and B represent nuclei. If we apply the Born-Oppenheimer approximation to eq 2.2, we can treat the nuclei as stationary which eliminates the nuclear kinetic energy term and reduces the nuclear repulsion term to a constant, V_{nuc}.

$$\hat{H} = -\frac{1}{2}\sum_{i}\nabla_i^2 - \sum_{iA}\frac{Z_A}{\mathbf{R}_A - r_i} + \sum_{i<j}\frac{1}{r_{ij}} + V_{\text{nuc}} \tag{2.3}$$

The first two terms of eq 2.3 are often grouped into a one-electron term, the third term is left as the two-electron term, and the final term is calculated separately and not included in the Hamiltonian.

$$\hat{H} = \hat{h}(i) + \hat{g}(i,j) \tag{2.4}$$

The wave function being acted on in eq 2.1 is a mathematical representation of a set of electrons which obey the spin statistic rules of fermions. Hence, we require the wave function to be antisymmetric which is accomplished by representing it as a Slater determinant. A Slater determinant is an antisymmetric linear combination of the Hartree product permutations of the molecular orbitals. This can be compactly written as

$$\Psi = \frac{1}{\sqrt{N!}}\begin{vmatrix} \psi_1^1 & \psi_2^1 & \psi_3^1 & \cdots & \psi_N^1 \\ \psi_1^2 & \psi_2^2 & \psi_3^2 & \cdots & \psi_N^2 \\ \psi_1^3 & \psi_2^3 & \psi_3^3 & \cdots & \psi_N^3 \\ \vdots & \vdots & \vdots & \ddots & \vdots \\ \psi_1^N & \psi_2^N & \psi_3^N & \cdots & \psi_N^N \end{vmatrix} = \sqrt{N!}\hat{A}[\psi_1^1\psi_2^2\cdots\psi_N^N] \tag{2.5}$$

$$\hat{A} = \frac{1}{N!}\sum_{P\in S_N}(-1)^{\pi}\hat{P} \tag{2.6}$$

where N is the number of electrons and molecular orbitals, ψ_p^q corresponds to the

electron q occupying molecular spin-orbital p, and the operator $\hat{A}$ is the antisymmetrizer which acts on a Hartree product to permute ($\hat{P}$) the indices and multiply the terms with an odd number of permutations by -1.

With this, we can get an equation for the electronic energy of a system. Equation 2.1 can be rearranged to solve for the energy by left multiplying both sides by $\langle\Psi|$. If eq 2.5 is inserted, we can take advantage of the orthonormality of the molecular orbitals to simplify the equation.

$$\begin{aligned} E &= \langle\Psi|\hat{H}|\Psi\rangle \\ &= N! \int \hat{A}[\psi_1^{1*}\psi_2^{2*}\cdots\psi_N^{N*}] \left[\sum_i \hat{h}(i) + \sum_{i<j} \hat{g}(i,j)\right] \hat{A}[\psi_1^1\psi_2^2\cdots\psi_N^N] d\tau_1 d\tau_2 \cdots d\tau_N \\ &= \sum_i \langle\psi_i^i|\hat{h}(i)|\psi_i^i\rangle + \sum_{i<j} \langle\psi_i^i\psi_j^j|\hat{g}(i,j)|\psi_i^i\psi_j^j\rangle - \langle\psi_i^i\psi_j^j|\hat{g}(i,j)|\psi_j^i\psi_i^j\rangle \end{aligned} \tag{2.7}$$

Though Ψ has $N!$ terms when expanded, only the certain integrals will be non-zero. In the case of the one-electron operator, if the bra and the ket are the same then the remaining terms which are not affected by $\hat{h}(i)$ will integrate to be 1. Otherwise, at least one electron integral will include different orthonormal molecular orbitals which integrate to 0. For similar reasons, the only non-zero terms left by the two-electron operator are those between identical Hartree products or a permutation of electrons i and j. This result is known as the first Slater-Condon rule and is often written as

$$E = \sum_i h_{ii} + \frac{1}{2}\sum_{ij} \langle ij||ij\rangle \tag{2.8}$$

where the antisymmetrized two-electron integral is $\langle ij||ij\rangle = \langle ij|ij\rangle - \langle ij|ji\rangle$ and uses a condensed notation of the occupied indices $i, j, ...$ to denote the orbitals being integrated ($\langle i|\hat{h}(i)|i\rangle = h_{ii}$, $\langle ij|\hat{g}(i,j)|ij\rangle = \langle ij|ij\rangle$).

The result of eq 2.7 can be spin integrated to give the restricted Hartree-Fock (RHF) energy expression which simplifies calculations on closed-shell molecules. When each molecular orbital is separated into their spin and spatial functions, the spin functions can be separated out and reduced using the integration results of the spin states $\omega(i) = \alpha, \beta$.

$$\langle \alpha | \alpha \rangle = 1 \tag{2.9a}$$

$$\langle \beta | \beta \rangle = 1 \tag{2.9b}$$

$$\langle \alpha | \beta \rangle = \langle \beta | \alpha \rangle = 0 \tag{2.9c}$$

Substituting $\psi_i^i = \phi_i^i \omega(i)$ into eq 2.7, we can reduce the summation terms by considering orbital occupancy of a closed shelled system where all of the orbitals are doubly occupied. The number of terms in the sum reduces by half and the integrals between identical Hartree products are doubled.

$$\begin{aligned} E = & \sum_i \langle \phi_i^i \omega(i) | \hat{h}(i) | \phi_i^i \omega(i) \rangle \\ & + \frac{1}{2} \sum_{i,j} \langle \phi_i^i \omega(i) \phi_j^j \omega(j) | \hat{g}(i,j) | \phi_i^i \omega(i) \phi_j^j \omega(j) \rangle - \langle \phi_i^i \omega(i) \phi_j^j \omega(j) | \hat{g}(i,j) | \phi_j^i \omega(i) \phi_i^j \omega(j) \rangle \\ & = 2 \sum_i^{N/2} \langle \phi_i | \hat{h}(i) | \phi_i \rangle + \sum_i^{N/2} \sum_j^{N/2} 2 \langle \phi_i \phi_j | \hat{g}(i,j) | \phi_i \phi_j \rangle - \langle \phi_i \phi_j | \hat{g}(i,j) | \phi_j \phi_i \rangle \end{aligned} \tag{2.10}$$

The coefficients in front of each term are a result of the possible combinations of spin functions that the term can have. The one-electron term would give rise to a single spin integral with the same spin function on each side, leaving two of the same spatial integrals from the α and β spin orbitals. In the first half of the two-electron term, there are four combinations possible from the α and β spin of each orbital. Since the electrons lie in the same spin orbital on each side of the integral, the separated spin

integral would reduce simply to 4. In the final term of the two-electron integral, there are again four possible combinations; however, because the electrons lie in different spin orbitals on each side of the integral, only the terms in which the two electrons have the same spin will be non-zero giving a total integration of 2.

The two parts of the two-electron term are referred to as the coulomb and exchange integrals respectively. The coulomb integral represent the coulombic repulsion experience by the electrons as a result of the other electrons in their environment. This aligns well with a classical view of the electrons as it ignores spin in accounting for the repulsion of two similarly charged particles. The exchange integral represents a property that does not have a classical counterpart which is the lowering of energy due to the exchange of indistinguishable electrons. In a closed-shell system, we would not expect the exchange term to be doubled for a given molecular orbital because the exchange would only be able to occur between electrons of the same spin. The coulomb and exchange integrals are common represented as $\hat{J}_j$ and $\hat{K}_j$ where

$$\hat{J}_j \left|\phi_i\right\rangle = \langle\phi_j|\hat{g}(i,j)|\phi_j\phi_i\rangle \tag{2.11}$$

$$\hat{K}_j \left|\phi_i\right\rangle = \langle\phi_j|\hat{g}(i,j)|\phi_i\phi_j\rangle \tag{2.12}$$

This representation allows these two-electron integrals to act as one-electron integrals which can be easily grouped with $\hat{h}$ to create the Fock operator, $\hat{f}$, which defines the Hartree-Fock (HF) equations

$$\hat{f}\phi_i = \left[\hat{h} + \sum_{j}^{N/2}(2\hat{J}_j - \hat{K}_j)\right]\phi_i = \epsilon_i\phi_i \tag{2.13}$$

where ϵ_i is the energy of orbital i.

The Hartree-Fock equations are a compact and elegant way of calculating the energy of the molecular orbitals, but they are more complex than a simple eigenvalue

problem. While the orbital energies are eigenvalues of the Fock operator, the Fock operator is also dependent on the orbital wave functions. The coulomb and exchange operators are represented as one-electron operators in the HF equations, but the two-electron integrals constructed by those operators include the same molecular orbitals for which the HF equations calculate the orbital energies. In this way, these operators represent the field experienced by each electron as a result of the other electrons. The main consequence of this is that solving the HF equations will return a new set of molecular orbitals which can also be used in the HF equations. Repeating this process results in a set of molecular orbitals which have converged towards a pre-defined threshold of precision. At each iteration, the orbitals are optimized within the constraint of the current field and returns a new set of orbitals. When the new set of molecular orbitals are sufficiently similar to those from which they were optimized, the orbitals are said to have converged. Hence, this method is often referred to as the self-consistent field (SCF) procedure.

While the SCF procedure itself is relatively easy to implement, there are other practical issues which prevent the HF equations from being used. The orbitals present in the HF equations, $\{\phi_i\}$, are molecular orbitals. Aside from very simple systems like small atoms, molecular systems give rise to molecular orbitals which we cannot represent analytically due to the correlation between the electrons. To address this issue, we can represent the molecular orbitals with basis functions, specifically as linear combinations of atomic orbitals (LCAOs)

$$\phi_i = \sum_q C_{qi}\chi_q \tag{2.14}$$

where χ_q are atomic orbitals and C_{qi} are the orbital coefficients which correspond to the extent to which ϕ_i is comprised of χ_q. By substituting eq 2.14 into eq 2.13, we can get the Roothaan-Hall equations.

$$\hat{f} \sum_q C_{qi}\chi_q = \epsilon_i \sum_q C_{qi}\chi_q \tag{2.15a}$$

$$\sum_q C_{qi} \langle \chi_p | \hat{f} | \chi_q \rangle = \epsilon_i \sum_q C_{qi} \langle \chi_p | \chi_q \rangle \tag{2.15b}$$

The integral $\langle \chi_p | \hat{f} | \chi_q \rangle$ requires further work because the expanded form

$$\langle \chi_p | \hat{f} | \chi_q \rangle = \langle \chi_p | \hat{h} | \chi_q \rangle + \sum_j^{N/2} 2 \langle \chi_p | \hat{J}_j | \chi_q \rangle - \langle \chi_p | \hat{K}_j | \chi_q \rangle \tag{2.16}$$

still includes the operators $\hat{J}_j$ and $\hat{K}_j$ which are defined in terms of molecular orbitals, not LCAOs. Further substituting in eq 2.14, we can redefine this integral entirely with atomic orbitals.

$$\langle \chi_p | \hat{f} | \chi_q \rangle = \langle \chi_p | \hat{h} | \chi_q \rangle + \sum_j^{N/2} \sum_r \sum_s C^*_{rj} C_{sj} (2 \langle \chi_p \chi_r | \hat{g} | \chi_q \chi_s \rangle - \langle \chi_p \chi_r | \hat{g} | \chi_s \chi_q \rangle) \tag{2.17}$$

We can then introduce the density matrix

$$D_{pq} = \sum_j^{N/2} C^*_{pj} C_{qj} \tag{2.18}$$

to simplify our final expression

$$\langle \chi_p | \hat{f} | \chi_q \rangle = \langle \chi_p | \hat{h} | \chi_q \rangle + \sum_r \sum_s D_{rs} (2 \langle \chi_p \chi_r | \hat{g} | \chi_q \chi_s \rangle - \langle \chi_p \chi_r | \hat{g} | \chi_s \chi_q \rangle) \tag{2.19}$$

The Roothaan-Hall equations can be neatly written in matrix form as

$$\mathbf{FC} = \mathbf{SC}\epsilon \tag{2.20}$$

where $\mathbf{F}$ represents the Fock matrix with element F_{pq} being the integral $\langle \chi_p | \hat{f} | \chi_q \rangle$, $\mathbf{C}$ is a matrix where the ith column holds the expansion coefficients for the ith orbital,

$\mathbf{S}$ is the overlap matrix with element S_{pq} being the integral $\langle \chi_p | \chi_q \rangle$, and ϵ is a column vector which holds the orbital energies. To start solving the Roothaan-Hall equations, the atomic orbitals which make up the basis functions need to be orthogonalized. This requires a unitary transformation $\mathbf{U}$ which can diagonalize our overlap matrix $\mathbf{S}$. There are multiple ways of accomplishing this, but only symmetric orthogonalization will be discussed here. For symmetric orthogonalization, $\mathbf{U}$ is chosen to be $\mathbf{S}^{-1/2}$ which gives

$$\mathbf{U}^T\mathbf{S}\mathbf{U} = \mathbf{S}^{-1/2}\mathbf{S}\mathbf{S}^{-1/2} = \mathbf{I} \tag{2.21}$$

Using this result requires some matrix manipulation of left multiplying each side of eq 2.20 by $\mathbf{S}^{-1/2}$ and additionally expanding the identity matrix $\mathbf{I} = \mathbf{S}^{1/2}\mathbf{S}^{-1/2}$ in the middle of each side.

$$\mathbf{S}^{-1/2}\mathbf{F}\mathbf{S}^{-1/2}\mathbf{S}^{1/2}\mathbf{C} = \mathbf{S}^{-1/2}\mathbf{S}\mathbf{S}^{-1/2}\mathbf{S}^{1/2}\mathbf{C}\epsilon \tag{2.22}$$

Because the orthogonalizer $\mathbf{S}^{-1/2}$ transforms the matrices into a new orthonormal basis, we can redefine our terms to reflect that by introducing the terms $\tilde{\mathbf{F}}$ and $\tilde{\mathbf{C}}$ where

$$\tilde{\mathbf{F}} = \mathbf{S}^{-1/2}\mathbf{F}\mathbf{S}^{-1/2} \tag{2.23}$$

$$\tilde{\mathbf{C}} = \mathbf{S}^{1/2}\mathbf{C} \tag{2.24}$$

The final equation is simply

$$\tilde{\mathbf{F}}\tilde{\mathbf{C}} = \tilde{\mathbf{C}}\epsilon \tag{2.25}$$

which is a standard eigenvalue problem. Equation 2.25 can be easily solved to give the orbital energies ϵ and the coefficient matrix $\tilde{\mathbf{C}}$ can be back-transformed to the original basis to use in the next iteration of the SCF procedure.

Finally, we can write an energy equation in terms of our basis atomic orbitals by employing the first Slater-Condon rule (eq 2.8) and substituting in eq 2.14

$$\begin{aligned} E &= 2\sum_{pq} D_{pq} \langle \chi_p | \hat{h} | \chi_q \rangle + \sum_{pqrs} D_{pq} D_{rs} [2 \langle \chi_p \chi_r | \hat{g} | \chi_q \chi_s \rangle - \langle \chi_p \chi_r | \hat{g} | \chi_s \chi_q \rangle] \\ &= \sum_{pq} D_{pq} (H_{pq} + F_{pq}) \end{aligned} \tag{2.26}$$

where H_{pq} is an element of the matrix form of the one-electron operator. In a practical implementation of the SCF procedure, the energy and density matrix are compared between successive iterations for the convergence criteria. As the orbitals themselves begin to converge, the energies corresponding to those orbitals should similarly converge. The wave functions are not compared directly, but the room-mean-squared deviation of the density matrix elements, which are constructed from the wave function coefficients, provides a reliable metric for the convergence of the orbitals. From the SCF procedure, we obtain both the energy and the wave function of our system at the HF level which can then be expanded on with post-HF methods.

2.2 Perturbation Theory

Often in physics, a system of interest is very closely related to a well-defined or analytically defined system with the addition of a small change or perturbation. In these cases, perturbation theory can offer an approximate solution to a problem with either an overly complex analytic solution or even with no analytic solution at all.

2.2.1 Rayleigh-Schrödinger Perturbation Theory

Rayleigh-Schrödinger perturbation theory (RSPT) is a general solution for a perturbed system and begins by defining the Hamiltonian, $\hat{H}$, as a sum of a simpler Hamiltonian for which we know the solutions, $\hat{H}_0$, and some perturbative potential,

$\hat{V}$. This can then be substituted into our basic energy equation.

$$\hat{H} = \hat{H}_0 + \hat{V} \tag{2.27}$$

$$(\hat{H}_0 + \hat{V})\,|\Psi_i\rangle = E_i\,|\Psi_i\rangle \tag{2.28}$$

Next, a continuous parameter, λ, is introduced as a modifier of the perturbation.

$$(\hat{H}_0 + \lambda\hat{V})\,|\Psi_i\rangle = E_i\,|\Psi_i\rangle \tag{2.29}$$

From HF theory, we know that both the energy and the wave function of a system are dependent on the Hamiltonian, so both E_i and $|\Psi_i\rangle$ could be considered functions of λ. Because λ is continuous, we can expand E_i and $|\Psi_i\rangle$ as Taylor series around $\lambda = 0$.

$$E_i = E_i^{(0)} + \lambda E_i^{(1)} + \lambda^2 E_i^{(2)} + \ldots \qquad E_i^{(k)} = \frac{1}{k!}\frac{\delta^k E_i}{\delta\lambda^k}\bigg|_{\lambda=0} \tag{2.30}$$

$$|\Psi_i\rangle = |\Phi_i^{(0)}\rangle + \lambda\,|\Phi_i^{(1)}\rangle + \lambda^2\,|\Phi_i^{(2)}\rangle + \ldots \qquad |\Phi_i^{(k)}\rangle = \frac{1}{k!}\frac{d^k\,|\Psi_i\rangle}{d\lambda^k}\bigg|_{\lambda=0} \tag{2.31}$$

In addition to all of the terms of the wave function expansion being normalized, the expansion is also defined such that $\langle\Psi_i|\Phi_i^{(0)}\rangle = 1$. This is called intermediate normalization and it follows then that $\langle\Phi_i^{(0)}|\Phi_i^{(k)}\rangle = 0$ where $k > 0$ in order for the previous integral to be true for all values of λ. It's worth noting that the zeroth order terms in these expansions correspond to the energy and wave function of the base Hamiltonian, $\hat{H}_0$. In RSPT, the parameter λ can act as a switch for the perturbation. Setting $\lambda = 0$ in eq 2.28 simply returns the original Hamiltonian with its familiar solutions. Similarly, the Taylor expansions would no longer be infinite sums and they would only contain the zeroth order solutions.

Substituting eqs 2.30 and 2.31 into eq 2.28, we can bring all the terms to one side and group them by their order of λ.

$$\begin{aligned} 0 = &\left(\hat{H}_0 \left|\Phi_i^{(0)}\right\rangle - E_i^{(0)} \left|\Phi_i^{(0)}\right\rangle\right) \\ &+\lambda \left(\hat{H}_0 \left|\Phi_i^{(1)}\right\rangle + \hat{V} \left|\Phi_i^{(0)}\right\rangle - E_i^{(0)} \left|\Phi_i^{(1)}\right\rangle - E_i^{(1)} \left|\Phi_i^{(0)}\right\rangle\right) \\ &+\lambda^2 \left(\hat{H}_0 \left|\Phi_i^{(2)}\right\rangle + \hat{V} \left|\Phi_i^{(1)}\right\rangle - E_i^{(0)} \left|\Phi_i^{(2)}\right\rangle - E_i^{(1)} \left|\Phi_i^{(1)}\right\rangle - E_i^{(2)} \left|\Phi_i^{(0)}\right\rangle\right) \\ &+ \dots \end{aligned} \tag{2.32}$$

While this is an infinite sum, each set of terms in the parentheses must be 0 in order for the equation to be true for all values of λ. This gives an infinite number of equations which can be used to solve for each of the terms in the Taylor expansions. From these equations, it is simple to find equations for arbitrary order energy terms by left multiplying by $\langle\Phi_i^{(0)}|$. Doing so for the first set of terms once again just returns the original Hamiltonian with its familiar solutions. For a general solution for an equation corresponding to the kth order of λ where $k > 0$, only two terms remain. The only surviving energy term is $E_i^{(k)}$ because the intermediate normalization of the wave function ensures that the other integrals with energy terms go to 0. Additionally, the integral involving the zeroth order Hamiltonian will be 0 because $\hat{H}_0$ is Hermitian and can effectively act on the bra of the integral to give an overlap integral that is 0 by intermediate normalization. All that remains is the term involving the perturbation, giving us a general energy expression.

$$E_i^{(k)} = \langle\Phi_i^{(0)}|\hat{V}|\Phi_i^{(k-1)}\rangle \tag{2.33}$$

Determining the higher-order wave function terms requires a more complicated approach. To obtain the kth order contribution to the wave function, left multiply the equation corresponding to by the term $\langle\Phi_n^{(0)}|$ where $n \neq i$. Because this wave function corresponds to a different solution of the Hamiltonian, we cannot take advantage of

intermediate normalization, but we can take advantage of the orthonormality of the zeroth order wave functions. Doing this for the equation corresponding to the zeroth order of λ is not useful because the zeroth order wave functions should already be known, but we can theoretically obtain an arbitrary order wave function correction this way. We can see this for the first order equation

$$\langle\Phi_n^{(0)}|\hat{H}_0|\Phi_i^{(1)}\rangle + \langle\Phi_n^{(0)}|\hat{V}|\Phi_i^{(0)}\rangle = \langle\Phi_n^{(0)}|E_i^{(0)}|\Phi_i^{(1)}\rangle + \langle\Phi_n^{(0)}|E_i^{(1)}|\Phi_i^{(0)}\rangle \tag{2.34a}$$

$$\langle\Phi_n^{(0)}|\Phi_i^{(1)}\rangle = -\frac{\langle\Phi_n^{(0)}|\hat{V}|\Phi_i^{(0)}\rangle}{E_n^{(0)} - E_i^{(0)}} \tag{2.34b}$$

If the first order wave function contribution is expanded using the zeroth order wave functions as a basis,

$$|\Phi_i^{(1)}\rangle = \sum_m c_{m,i}^{(1)} |\Phi_m^{(0)}\rangle \tag{2.35}$$

we can see by left multiplying by $\langle\Phi_m^{(0)}|$ that the coefficients must be

$$c_{m,i}^{(1)} = \langle\Phi_m^{(0)}|\Phi_i^{(1)}\rangle \tag{2.36}$$

which means that eq 2.35 is equivalent to

$$|\Phi_i^{(1)}\rangle = \sum_{n\neq i} -\frac{\langle\Phi_n^{(0)}|\hat{V}|\Phi_i^{(0)}\rangle}{E_n^{(0)} - E_i^{(0)}} |\Phi_n^{(0)}\rangle \tag{2.37}$$

This result can be substituted into eq 2.33 where $k = 2$ to give a second order energy correction

$$E_i^{(2)} = \langle\Phi_i^{(0)}|\hat{V}|\Phi_i^{(1)}\rangle = \sum_{n\neq i} -\frac{\langle\Phi_n^{(0)}|\hat{V}|\Phi_i^{(0)}\rangle \langle\Phi_i^{(0)}|\hat{V}|\Phi_n^{(0)}\rangle}{E_n^{(0)} - E_i^{(0)}} = \sum_{n\neq i} -\frac{|\langle\Phi_i^{(0)}|\hat{V}|\Phi_n^{(0)}\rangle|^2}{E_n^{(0)} - E_i^{(0)}} \tag{2.38}$$

By repeating this process, any order energy or wave function correction can be calculated, but this expansion is typically truncated at second order.

2.2.2 Møller-Plesset Perturbation Theory

We can apply RSPT to the problem of calculating electronic energies by carefully choosing the zeroth order Hamiltonian and perturbation. They are defined as the Fock operator and the electronic potential not in the HF potential.

$$\hat{H}_0 = \sum_i \hat{f} = \sum_i \left[\hat{h} + \sum_j (\hat{J}_j - \hat{K}_j) \right] \tag{2.39}$$

$$\hat{V} = \sum_{i<j} \hat{g}(i,j) - \sum_{i,j} (\hat{J}_j - \hat{K}_j) \tag{2.40}$$

This choice of Hamiltonian and perturbation is referred to as either Møller-Plesset Perturbation Theory (MPn) or as Many-Body Perturbation Theory (MBPT). Here, only MP2 will be discussed and energy corrections will only be determined up to second order. With the Fock operator as the zeroth order Hamiltonian, the zeroth order energy solutions are the molecular orbital energies.

$$E_i^{(0)} = \langle \Phi_i^{(0)} | \hat{f} | \Phi_i^{(0)} \rangle = \epsilon_i \tag{2.41}$$

However, if the first order correction is included, we get the HF energy.

$$E_i^{(1)} = \langle \Phi_i^{(0)} | \hat{V} | \Phi_i^{(0)} \rangle = \frac{1}{2} \sum_{i,j} \langle ij||ij \rangle - \sum_{i,j} \langle ij||ij \rangle = -\frac{1}{2} \sum_{i,j} \langle ij||ij \rangle \tag{2.42}$$

$$E_i^{\mathrm{HF}} = E_i^{(0)} + E_i^{(1)} = \sum_i h_{ii} + \frac{1}{2} \sum_{i,j} \langle ij||ij \rangle \tag{2.43}$$

Thus, for MP2, the only energy correction which needs to be calculated is the second order correction. The numerator of eq 2.38 is similar to the first order energy correction except that one of the states is an excited wave function of the zeroth order ground state. Because the perturbation only includes two-electron operators, the only excited wave functions which will return non-zero values will be those with exactly

two excitations relative to the reference state. The resulting integral will then be

$$\langle \Phi_n^{(0)} | \hat{V} | \Phi_i^{(0)} \rangle = \langle ij||ab \rangle \tag{2.44}$$

where $i, j, ...$ represent the orbitals of the reference wave function and $a, b, ...$ represent the newly filled orbitals of the excited wave function. Because the summation runs over all wave functions other than the reference state, the summation can be rewritten to include all combinations of orbitals which are included in the integral. The integral itself is then also symmetric in i and j as well as a and b, so the equation can included a full summation with a factor of $1/4$ to account for duplicates.

$$E_i^{(2)} = \frac{1}{4} \sum_{ijab} \frac{| \langle ij||ab \rangle |^2}{E_i^{(0)} - E_n^{(0)}} \tag{2.45}$$

The denominator is simply the difference between the zeroth order energies of the two states which is only the energy difference of the newly occupied orbitals of the excited state and the originally occupied orbitals of the ground state.

$$E_i^{(2)} = \frac{1}{4} \sum_{ijab} \frac{| \langle ij||ab \rangle |^2}{\epsilon_i + \epsilon_j - \epsilon_a - \epsilon_b} \tag{2.46}$$

This energy correction is one of the simplest ways to account for correlation energy beyond the HF level. However, it requires some conditions to be met in order to work well. In general, perturbation theory requires small perturbations. If the true Hamiltonian is greatly different from the zeroth order approximation, it no longer makes sense to use the zeroth order wave functions as a basis for higher order contributions. Additionally, the form of the denominator in eq 2.46 requires that the energies of the states be well-separated, otherwise the energy could become unphysically large.

2.3 Coupled Cluster

To further improve the electronic wave function and energy, the correlation energy can be calculated using coupled cluster theory (CC). In CC theory, the clusters refer to specific groups of excited states which are accessed via cluster operators. The excited states are grouped by their total level of excitation, so solitary terms of higher excitation will be grouped with products of lower excitation terms. These clusters of excited states are mixed into the wave function to provide flexibility and account for electron correlation. In this way, it is better alternative to truncated full configuration interaction, because CC theory retains the size consistency of FCI which is lost in truncated FCI.

2.3.1 Full Configuration Interaction

Discussing coupled cluster theory is easiest with an understanding of full configuration interaction (FCI). In FCI, the total wave function, $|\Psi\rangle$, is represented by a linear combination of all of the possible electron configurations of some reference wave function

$$|\Psi\rangle = c_0 |\Phi\rangle + \left(\frac{1}{1!}\right)^2 \sum_{ia} c_i^a |\Phi_i^a\rangle + \left(\frac{1}{2!}\right)^2 \sum_{\substack{ij \\ ab}} c_{ij}^{ab} |\Phi_{ij}^{ab}\rangle + \left(\frac{1}{3!}\right)^2 \sum_{\substack{ijk \\ abc}} c_{ijk}^{abc} |\Phi_{ijk}^{abc}\rangle + \cdots \tag{2.47}$$

where indices $i, j, k, \ldots$ corresponds to the occupied orbitals in the reference wave function and the indices $a, b, c, \ldots$ correspond to the newly occupied orbitals of the excited wave functions, and the pre-factors account for equivalent terms. With intermediate normalization, the wave function can be written as collection of operators acting on a reference wave function

$$|\Psi\rangle = (1 + \hat{C}_1 + \hat{C}_2 + \hat{C}_3 + \ldots) |\Phi\rangle \tag{2.48}$$

where $\hat{C}_n$ is an operator which constructs a sum of all possible wave functions of excitation level n with the appropriate coefficient and symmetry factor.

$$\hat{C}_n \left|\Phi\right\rangle = \left(\frac{1}{n!}\right)^2 \sum_{\substack{ijk...n \\ abc...m}} c_{ijk...n}^{abc...m} \left|\Phi_{ijk...n}^{abc...m}\right\rangle \tag{2.49}$$

FCI energies and coefficients can be calculated by constructing the Hamiltonian matrix where each element is

$$\mathbf{H}_{ij} = \langle \Phi_i | \hat{H} | \Phi_j \rangle \tag{2.50}$$

where Φ_i and Φ_j can be any possible electron configurations of any excitation level. The Hamiltonian matrix can be thought of as a collection of smaller matrix blocks that correspond to two collections of excitation levels. These matrix elements are relatively easily calculated using the Slater-Condon rules, but the number of elements that need to be calculated, even for simpler systems, makes this method unpractical.

One solution is to truncate the terms in eq 2.47 so as to only include the most important excited states. In a well-behaved system, many of the coefficients will be close to 0, and can be safely ignored. Some common forms of truncated FCI are CID and CISD which use only the double excitations or single and double excitations, respectively. However, by truncating the FCI ansatz, it is no longer size consistent. This can be easily seen in a dimer system. For some monomer A, CID would include all of the double excitations of the single molecule wave function. In the case of the dimer at some large distance (i.e. two non-interacting monomers), only double excitations on a single molecule A would be included. No wave functions would be included where each monomer had a double excitation, and to do so would require the inclusion of quadruple excitations. Additionally, the dimer would included single excitations on separate monomers, a state not accounted for in the single monomer case. The resulting wave functions for these two cases would included different sets of excitations, so the energy would not scale linearly with the number of monomers.

2.3.2 General Coupled Cluster Theory

Conceptually, the CC approximation is very similar to FCI, but it approximates the contributions of higher excited states as products of lower excited states. The CC ansatz can be compactly written as

$$|\Psi\rangle = e^{\hat{T}} |\Phi\rangle \tag{2.51}$$

where the cluster operator $\hat{T}$ is a sum of smaller cluster operators

$$\hat{T} = \hat{T}_1 + \hat{T}_2 + \hat{T}_3 + \cdots + \hat{T}_n \tag{2.52}$$

These smaller cluster operators are similar to the operators of FCI and have the form

$$\hat{T}_n |\Phi\rangle = \left(\frac{1}{n!}\right)^2 \sum_{\substack{i_1<\cdots<i_n \\ a_1<\cdots<a_n}} t_{a_1\ldots a_n}^{i_1\ldots i_n} |\Phi_{i_1\ldots i_n}^{a_1\ldots a_n}\rangle \tag{2.53}$$

where $t_{a_1\ldots a_n}^{i_1\ldots i_n}$ are the amplitudes of the excitation they are associated with. To fully write out the CC ansatz, the exponential is expanded as a Taylor series

$$e^{\hat{T}} = 1 + \frac{1}{1!}\hat{T} + \frac{1}{2!}\hat{T}^2 + \frac{1}{3!}\hat{T}^3 + \ldots \tag{2.54}$$

and the final result depends on the form of $\hat{T}$. The cluster operator $\hat{T}$ could have as many terms as there are electrons, but it is typically truncated to make the method computationally feasible. For example, in coupled cluster with doubles (CCD), the cluster operator is truncated as $\hat{T} = \hat{T}_2$, so only double excitations are mixed into the wave function. Thus, eq 2.54 becomes

$$e^{\hat{T}} = 1 + \hat{T}_2 + \frac{1}{2}\hat{T}_2^2 + \frac{1}{6}\hat{T}_2^3 + \ldots \tag{2.55}$$

and the wave function is

$$|\Psi\rangle = (1 + \hat{T}_2 + \frac{1}{2}\hat{T}_2^2 + \frac{1}{6}\hat{T}_2^3 + \dots)\,|\Phi\rangle \tag{2.56}$$

where $\langle\Phi|\Psi\rangle = 1$. While the Taylor series is infinite, only a finite number of terms are needed to calculate the CC energy and amplitudes. From the Slater-Condon rules, Hamiltonian matrix elements of wave functions that differ by more than two occupations vanish. Energy equations can be found by substituting the CC wave function into the Schrödinger equation and left multiplying by $\langle\Phi|$. In CCD, this is very straightforward

$$\langle\Phi|E|\Psi\rangle = \langle\Phi|\hat{H}|\Psi\rangle \tag{2.57a}$$

$$E = \langle\Phi|\hat{H}(1 + \hat{T}_2)|\Phi\rangle \tag{2.57b}$$

and only requires the amplitudes associated with the operator $\hat{T}_2$. In general, amplitudes can be calculated with the wave function which is found in the same manner as the energy, only instead left multiplying by $\langle\Phi^{a_1\dots a_n}_{i_1\dots i_n}|$ where n corresponds to the excitation level of the cluster operator. Doing this to calculate t^{ij}_{ab} which is needed for the CCD energy, gives

$$\langle\Phi^{ab}_{ij}|\mathcal{E}^{ij}_{ab}|\Psi\rangle = \langle\Phi^{ab}_{ij}|\hat{H}|\Psi\rangle \tag{2.58a}$$

$$t^{ij}_{ab} = (\mathcal{E}^{ij}_{ab})^{-1}\,\langle\Phi^{ab}_{ij}|\hat{H}(1 + \hat{T}_2 + \frac{1}{2}\hat{T}_2^2)|\Phi\rangle \tag{2.58b}$$

which also is only dependent on the amplitudes t^{ij}_{ab}. Here, $\mathcal{E}^{ij}_{ab}$ is the energy of the excited state in the bra which corresponds to the amplitudes being calculated.

However, if $\hat{T}$ was not truncated, or if it was truncated at a later term, this equation would be greatly expanded. In the case of coupled cluster with singles and

doubles (CCSD), the wave function would instead be

$$|\Psi\rangle = (1+\hat{T}_1+\hat{T}_2+\frac{1}{2}\hat{T}_1^2+\hat{T}_1\hat{T}_2+\frac{1}{2}\hat{T}_2^2+\frac{1}{6}\hat{T}_1^3+\frac{1}{2}\hat{T}_1^2\hat{T}_2+\frac{1}{2}\hat{T}_1\hat{T}_2^2+\frac{1}{6}\hat{T}_2^3+\dots)\,|\Phi\rangle \quad (2.59)$$

Because the energy is dependent on states with an excitation level of 2, the resulting energy equation would be

$$E = \langle\Phi|\hat{H}(1+\hat{T}_2+\frac{1}{2}\hat{T}_1^2)|\Phi\rangle \quad (2.60)$$

and the amplitudes, t_a^i and t_{ab}^{ij}, are

$$t_a^i = (\mathcal{E}_a^i)^{-1}\,\langle\Phi_i^a|\hat{H}(\hat{T}_1+\hat{T}_2+\frac{1}{2}\hat{T}_1^2+\hat{T}_1\hat{T}_2+\frac{1}{6}\hat{T}_1^3)|\Phi\rangle \quad (2.61)$$

$$t_{ab}^{ij} = (\mathcal{E}_{ab}^{ij})^{-1}\,\langle\Phi_{ij}^{ab}|\hat{H}(1+\hat{T}_1+\hat{T}_2+\frac{1}{2}\hat{T}_1^2+\hat{T}_1\hat{T}_2+\frac{1}{6}\hat{T}_1^3+\frac{1}{2}\hat{T}_2^2+\frac{1}{2}\hat{T}_1^2\hat{T}_2+\frac{1}{24}\hat{T}_1^4)|\Phi\rangle \quad (2.62)$$

As the truncation of the ansatz decreases, the terms needed to calculate the energy and amplitudes increases drastically. Because the double excitations are the most important for calculating the energy, truncation schemes will included at least $\hat{T}_2$ and often $\hat{T}_1$. While t_{ab}^{ij} does rely on the quadruple excitations, their contribution is still approximately treated due to the presence of the $\hat{T}_2^2$ term. This also addresses the size consistency issue of truncated CI; a double excitation on each of two separated monomer would be included in the CC wave function.

2.3.3 Perturbative Excitations

While CC theory provides an excellent level of accuracy, even when truncated, it suffers from the same issues as FCI with regards to feasibility. Even at the CCSDT level, only calculations on small molecules with moderate basis sets can be finished in a reasonable amount of time. A commonly used method of addressing this issue

is to treat higher-order excitation contributions perturbatively.[17] For example, in a well-behaved system, the expected contributions of triple excitations would be small, as they don't directly contribute to the energy of the system; however, the number of matrix elements required to explicitly include triple excitations makes approximating them an attractive prospect. When a level of excitations is treated perturbatively, it is denoted by enclosing the corresponding letter in parentheses, as in CCSD(T). The perturbative triples correction can be calculated using RSPT as

$$\Delta E_T = \sum_t^T \frac{|\langle\Psi|\hat{V}|\Psi_t\rangle|^2}{E_0 - E_t} = \sum_s^{S+D}\sum_t^T\sum_u^D \frac{a_s V_{st} V_{tu} a_u}{E_0 - E_t} \tag{2.63}$$

where V corresponds to the perturbation operator (in this case, the correlation Hamiltonian), t sums over triple excitations, s sums over all single and double excitations, u sums over only double excitations, and a_i is the converged wave function coefficient for excitation i. The denominator here is the excitation energy of the triply excited state given by the Fock Hamiltonian.

2.4 Vibrational Frequencies

Molecular vibrations play an important role in several aspects of computational and theoretical chemistry. Perhaps most notably, calculated frequencies can be used for identification in spectroscopic data such as IR or Raman spectra. Additionally, they are important in identifying stationary points on a potential energy surface and are necessary for transition state searches. Even in thermodynamics, the vibrational degrees of freedom play an important role in calculating the entropy and free energy of a system. Calculating these frequencies requires the potential of a system which can be written as

$$V(\mathbf{x}) = V_0 + \sum_i^{3N-6} \frac{\partial V}{\partial x_i} x_i + \frac{1}{2!}\sum_{ij}^{3N-6} \frac{\partial^2 V}{\partial x_i \partial x_j} x_i x_j + \frac{1}{3!}\sum_{ijk}^{3N-6} \frac{\partial^3 V}{\partial x_i \partial x_j \partial x_k} x_i x_j x_k + \ldots \tag{2.64}$$

which is a typical Taylor expansion of the potential in the $3N-6$ dimensional (or $3N-5$ dimensional for linear molecules) space of a molecule's internal coordinates. Often the first derivative terms are not included because a stationary state lying in a potential well would have a first derivative of 0 with respect to all dimensions. Often, the harmonic approximation is made in which the potential expansion is truncated at the second order terms as

$$V(\mathbf{x}) = \frac{1}{2}\sum_{ij}^{3N-6} \frac{\partial^2 V}{\partial x_i x_j} x_i x_j \tag{2.65}$$

where V_0 is arbitrarily set to 0.

2.4.1 The GF Matrix Method

The GF matrix method seeks to calculate harmonic vibrational frequencies in internal coordinates. This is accomplished by solving the eigenvalue problem

$$(\mathbf{GF})\mathbf{L} = \mathbf{L}(\boldsymbol{\mu}\boldsymbol{\Lambda}) \tag{2.66}$$

where the eigenvalues give the square of the angular frequencies ($\omega_i = \sqrt{\mu_i \lambda_i}$). This process simultaneously solves the kinetic and potential energy eigenvalue problems.

$$\mathbf{L}^{-1}\mathbf{G}(\mathbf{L}^{-1})^{\mathrm{T}} = \boldsymbol{\mu} \tag{2.67}$$

$$\mathbf{L}^{\mathrm{T}}\mathbf{F}\mathbf{L} = \boldsymbol{\Lambda} \tag{2.68}$$

In these equations, the matrix $\mathbf{G}$ contains structural information about the molecule and is related to the internal coordinates. The elements of the $\mathbf{G}$ are calculated as

$$G_{ij} = \sum_n \frac{B_n^i B_n^j}{m_n} \tag{2.69}$$

where i and j refer to internal coordinates, n corresponds to the $3N$ Cartesian coordinates, m_n is the mass of the atom associated with coordinate n, and B_n^i is the first-order B-matrix element that is defined as the derivative of the internal coordinate i with respect to the Cartesian coordinate n.

$$B_n^i = \frac{\partial S_i}{\partial x_n} \tag{2.70}$$

The matrix $\mathbf{F}$ is the Hessian, a second-order force constant matrix, which can be calculated analytically (when available for a given level of theory) or numerically via finite differences of gradients or energies. Finally, the matrix $\mathbf{L}$ can be used to transform between the internal coordinates ($\mathbf{s}$) and the normal coordinates ($\mathbf{Q}$).

$$\mathbf{s} = \mathbf{LQ} \tag{2.71}$$

The $\mathbf{GF}$ matrix is not a symmetric matrix, but eq 2.66 can be manipulated to become a symmetric eigenvalue problem by using the substitution $\mathbf{L}' = \mathbf{G}^{-1/2}\mathbf{L}$ which gives

$$(\mathbf{GF})\mathbf{G}^{1/2}\mathbf{L}' = \mathbf{G}^{1/2}\mathbf{L}'(\boldsymbol{\mu}\boldsymbol{\Lambda}) \tag{2.72a}$$

$$(\mathbf{G}^{1/2}\mathbf{F}\mathbf{G}^{1/2})\mathbf{L}' = \mathbf{L}'(\boldsymbol{\mu}\boldsymbol{\Lambda}) \tag{2.72b}$$

The symmetric matrix $\mathbf{G}^{1/2}\mathbf{F}\mathbf{G}^{1/2}$ can be diagonalized, and a back-transformation by $\mathbf{G}^{1/2}$ would return $\mathbf{L}$.

2.4.2 Vibrational Perturbation Theory

Often, the harmonic approximation is not sufficient to accurately describe the vibrational motion of a molecule. An anharmonic treatment of molecular vibrations benefits from the inclusion of higher-order terms of the potential expansion. Once

again, perturbation theory can be employed by treating these terms as a perturbation to the harmonic oscillator wave function[18]

$$\hat{V}_{anh} = \frac{1}{3!}\sum_{ijk}\phi_{ijk}\hat{q}_i\hat{q}_j\hat{q}_k + \frac{1}{4!}\sum_{ijkl}\phi_{ijkl}\hat{q}_i\hat{q}_j\hat{q}_k\hat{q}_l + ... \tag{2.73}$$

where the position variables, x_i, have been replaced by the normal coordinates, $\hat{q}_i$, of the harmonic oscillator and ϕ_{ijk} is the force constant corresponding to the normal modes i, j, k. The full anharmonic perturbation additionally includes the vibrational angular momentum operator ($\hat{H}_{cor}$) and the Watson pseudopotential ($\hat{U}$)

$$\hat{V} = \hat{V}_{anh} + \hat{H}_{cor} + \hat{U} \tag{2.74}$$

$$\hat{H}_{cor} = \sum_{\tau,i<j}\left[\left(\frac{\omega_i^2+\omega_j^2}{\omega_i\omega_j}\right)B_e^\tau(\zeta_{ij}^\tau)^2\right]\hat{q}_i^2\hat{q}_j^2 \tag{2.75}$$

$$\hat{U} = -\frac{1}{4}\sum_{\tau}B_e^\tau \tag{2.76}$$

where ω_i is the frequency of mode i, B_e^τ is the rotational constant corresponding to the axis τ, and ζ_{ij}^τ is the Coriolis constant that couples the normal coordinates $\hat{q}_i$ and $\hat{q}_j$ about the axis τ. The process is referred to as vibrational perturbation theory and this discussion will be limited to second-order (VPT2) which truncates $\hat{V}_{anh}$ at the quartic terms.

Using eqs 2.33 and 2.38, the total ground state VPT2 energy can be written as

$$E_i = \epsilon_i + \langle i|\hat{V}|i\rangle + \sum_{i\neq i'}\frac{|\langle i|\hat{V}|i'\rangle|^2}{\epsilon_i - \epsilon_{i'}} \tag{2.77}$$

where i is the ground harmonic oscillator wave function, i' is an excited state of state i, and ϵ_i is the harmonic oscillator energy of state i. This equation can be greatly simplified due to the properties of the involved integrals which restrict what level of excitation is allowed for each type of position operator.

$$E_i = \epsilon_i + \langle i|\frac{1}{24}\sum_{ijkl}\phi_{ijkl}\hat{q}_i\hat{q}_j\hat{q}_k\hat{q}_l + \hat{H}_{cor} + \hat{U}|i\rangle + \sum_{i\neq i'}\frac{|\langle i|\frac{1}{6}\sum_{ijk}\phi_{ijk}\hat{q}_i\hat{q}_j\hat{q}_k|i'\rangle|^2}{\epsilon_i - \epsilon_{i'}} \quad (2.78)$$

The total VPT2 energy of a molecule in wavenumbers can be expressed using anharmonicity constants which are derived from the previous equation. This energy expression is written as

$$E(\mathrm{v}) = G_0 + \sum_i \omega_i\left(\mathrm{v}_i + \frac{1}{2}\right) + \sum_{i\leq j}\chi_{ij}\left(\mathrm{v}_i + \frac{1}{2}\right)\left(\mathrm{v}_j + \frac{1}{2}\right) \quad (2.79)$$

where the ω_i is the frequency of mode i, v_i is the quantum number associated with mode i, and the anharmonicity constants χ_{ij} are defined as

$$\chi_{ii} = \frac{1}{16}\phi_{iiii} - \frac{1}{32}\sum_j \phi_{iij}^2\left(\frac{1}{2\omega_i + \omega_j} + \frac{4}{\omega_j} - \frac{1}{2\omega_i - \omega_j}\right) \quad (2.80)$$

$$\begin{aligned}\chi_{ij} = \frac{1}{4}\phi_{iijj} - \frac{1}{4}\sum_k \frac{\phi_{iik}\phi_{jjk}}{\omega_k} - \frac{1}{8}\sum_k \phi_{ijk}^2\left(\frac{1}{\omega_i + \omega_j + \omega_k} + \frac{1}{-\omega_i + \omega_j + \omega_k}\right. \\ \left. + \frac{1}{\omega_i - \omega_j + \omega_k} - \frac{1}{\omega_i + \omega_j - \omega_k}\right) + \sum_\tau B_e^\tau(\zeta_{ij}^\tau)^2\left(\frac{\omega_i}{\omega_j} + \frac{\omega_j}{\omega_i}\right)\end{aligned} \quad (2.81)$$

The G_0 term contains additional terms not related to the quantum number v_i. The fundamental frequency of mode i, ν_i can be calculated by taking the difference of this equation when v_i is 1 and when all quantum numbers are 0

$$\nu_i = \omega_i + 2\chi_{ii} + \frac{1}{2}\sum_{i\neq j}\chi_{ij} \quad (2.82)$$

2.5 Kinetics

Rates and rate constants can be calculated in a relatively straightforward manner via canonical transition state theory (CTST). For CTST, a simple rigid rotor, harmonic oscillator (RRHO) partition function of an ideal gas is used to describe the transition state and reactants in the reaction. This allows for separability of the par-

tition function into the translational, rotational, vibrational, and electronic partition functions.

$$q = q_{trans} q_{rot} q_{vib} q_{el} \tag{2.83}$$

In general a partition function can be written as

$$q = \sum_i e^{-\epsilon_i / k_B T} \tag{2.84}$$

where the index i corresponds to the states of the molecule, k_B is the Boltzmann constant, and T is the temperature in Kelvin. Using the energy level equation for an energy mode gives the partition function for that mode.

The translational partition function uses the energy equation of a particle in a 3-dimensional cubic box

$$E_i = \frac{h^2}{8mL^2}(n_x^2 + n_y^2 + n_z^2) \tag{2.85}$$

where h is Planck's constant, m is the mass of the particle, L is the length of the sides of the box, and n_α is the quantum number for the motion in the α-axis. Inserting this into eq 2.84 gives

$$\begin{aligned} q_{trans} &= \sum_i e^{-h^2(n_x^2+n_y^2+n_z^2)/8mL^2 k_b T} \\ &= \sum_i \left(e^{-h^2 n_x^2/8mL^2 k_b T}\right)\left(e^{-h^2 n_y^2/8mL^2 k_b T}\right)\left(e^{-h^2 n_z^2/8mL^2 k_b T}\right) \end{aligned} \tag{2.86}$$

Because this summation includes all states, and thus all the possible combinations of indices for n_x, n_y, and n_z, it can be rewritten using the quantum numbers as indices

$$\begin{aligned} q_{trans} &= \sum_{n_x=1} e^{-h^2 n_x^2/8mL^2 k_b T} \sum_{n_y=1} e^{-h^2 n_y^2/8mL^2 k_b T} \sum_{n_z=1} e^{-h^2 n_z^2/8mL^2 k_b T} \\ &= \left(\sum_{n=1} e^{-h^2 n^2/8mL^2 k_b T}\right)^3 \end{aligned} \tag{2.87}$$

and can be grouped together because the sums for each quantum number are equivalent. Because translational energy levels are so close in energy to one another, the sum can be approximated as an integral

$$q_{trans} \approx \left(\int_0^\infty e^{-h^2 n^2 / 8mL^2 k_b T} dn \right)^3 \tag{2.88}$$

which has the form of the known integral

$$\int_0^\infty e^{-\alpha x^2} dx = \frac{1}{2}\sqrt{\frac{\pi}{\alpha}} \tag{2.89}$$

where $\alpha = h^2/8mL^2k_BT$. Evaluating this integral gives the final translational partition function of an ideal gas which can be simplified by redefining the equation using the volume of the cube, V, rather than the length

$$q_{trans} = \left(\frac{1}{2}\sqrt{\frac{8\pi mL^2 k_B T}{h^2}} \right)^3 = \left(\frac{2\pi m k_B T}{h^2} \right)^{3/2} V \tag{2.90}$$

This is often simplified further by defining the de Broglie wavelength, Λ, as

$$\Lambda = \left(\frac{2\pi m k_B T}{h^2} \right)^{-1/2} \tag{2.91}$$

rewriting the translational partition function to

$$q_{trans} = \frac{V}{\Lambda^3} \tag{2.92}$$

This partition function is very simple to calculate for any molecule, and is only dependent on its mass and the temperature.

The next partition function to consider is the rigid rotor rotational partition function, q_{rot}, which uses the energy expression

$$E_J = \frac{\hbar^2}{2I} J(J+1) \tag{2.93}$$

where I is the moment of inertia of the molecule, J is the rotational quantum number, and the levels have a degeneracy of $2J+1$. Inserting this into eq 2.84 gives the the partition function

$$q_{rot} = \sum_J (2J+1) e^{-\hbar^2 J(J+1)/2Ik_BT} \tag{2.94}$$

Once again, the difference of the energy levels is small, so the sum is approximated as an integral over the values of J which can be easily solved through substitution of $u = J(J+1)$

$$q_{rot} = \int_0^\infty (2J+1) e^{-\alpha J(J+1)} dJ = \int_0^\infty e^{-\alpha u} du = \frac{1}{\alpha} = \frac{2Ik_BT}{\hbar^2} \tag{2.95}$$

where $\alpha = \hbar^2/2Ik_BT$. The rotational partition function is often written using the characteristic temperature, $\theta_{\text{rot}} = \hbar^2/2Ik_B$

$$q_{rot} = \frac{T}{\theta_{\text{rot}}} \tag{2.96}$$

Finally, an additional symmetry factor, σ, is introduced

$$q_{rot} = \frac{T}{\sigma\theta_{\text{rot}}} \tag{2.97}$$

which is 2 for homonuclear diatomic molecules and 1 for all other molecules to account for nuclear spin states.

Harmonic oscillator vibrational partition function can be more easily represented as the product of smaller partition functions for the individual modes. The harmonic

vibrational energy of mode i has a very simple energy equation

$$E_{i,\mathrm{v}} = h\nu_i \left(\mathrm{v} + \frac{1}{2}\right) \tag{2.98}$$

where ν_i and v are the frequency and quantum number of mode i, respectively. This can be easily redefined to give the energy relative to the zero-point vibrational energy (i.e. v= 0)

$$E_{i,\mathrm{v}} = h\nu_i \mathrm{v} \tag{2.99}$$

These energies can be inserted into eq 2.84 and grouped by mode to give the partition function

$$q_{vib} = \prod_i \sum_{\mathrm{v}} (e^{-h\nu_i/k_B T})^{\mathrm{v}} \tag{2.100}$$

Because the exponential in the sum will always be between 0 and 1, the sum is a geometric series which has a simple closed form

$$\sum_{i=0}^{\infty} x^i = \frac{1}{1-x} \tag{2.101}$$

The vibrational partition function then becomes

$$q_{vib} = \prod_i \frac{1}{1 - e^{-h\nu_i/k_B T}} \tag{2.102}$$

To simplify it further, the vibrational characteristic temperature, $\theta_{vib,i} = h\nu_i/k_B$, is used

$$q_{vib} = \prod_i \frac{1}{1 - e^{\theta_{vib,i}/T}} \tag{2.103}$$

The product in the vibrational partition function has a term for each vibrational mode which is simple to calculate as they only require the harmonic frequencies to be known. If the partition function were still defined relative to the electronic energy and not the zero-point energy, it would have an additional exponential term which

would scale the energy appropriately; however, this will be accounted for later in the rate equation.

The simplest partition function is the electronic partition function, which inserts into eq 2.84 the calculated electronic energy and its excitation energies. While this seems like it cannot be simplified through mathematical methods, it can be done through chemical intuition. Excited states are typically much higher in energy then the ground state, so all of the terms in the sum other than the ground state would be close to 0 and can be ignored. When the partition function is defined relative to the ground state energy, the electronic partition function simply becomes the degeneracy of the ground state.

$$q_{el} = g_0 \tag{2.104}$$

In CTST, rate constants are calculated using the Eyring equation which relates the rate constant to the reactants and transition state

$$k = \kappa \frac{k_B T}{h} K^{\ddagger} e^{-(E_{\mathrm{TS}} - E_{\mathrm{R}})/k_B T} \tag{2.105}$$

where κ is the transmission coefficient for and asymmetric Eckart potential

$$\kappa(T) = \exp\left(\frac{\Delta V_1}{RT}\right) \int_0^{\infty} \kappa(E) \exp\left(\frac{E}{RT}\right) dE \tag{2.106}$$

$K^{\ddagger}$ is the equilibrium constants of the reactants and transition state, E_{TS} and E_{R} refer to the energy of the transition state and reactants, respectively, and the $k_B T/h$ factor corresponds to the frequency of the transition state overcoming the barrier. Here, the energies used include the zero-point vibrational energy to account for the vibrational partition function being defined relative to the zero-point energy. The equilibrium constant can be written using the partition functions of each species and

the volume to represent the number density of each species.

$$K^{\ddagger} = \frac{q_{\mathrm{TS}}/V}{\prod_i^{\mathrm{R}} (q_i/V)^{\nu_i}} \tag{2.107}$$

When pre-reactive complexes are involved in the reaction, the Steady State approximation (SSA) can be used to substitute contributions from other species with those of the reactants. For the reaction

$$\mathrm{A} + \mathrm{B} \underset{k_{-1}}{\overset{k_1}{\rightleftharpoons}} \mathrm{A}\cdots\mathrm{B} \xrightarrow{k_2} \mathrm{C}^{\ddagger} \xrightarrow{k_3} \mathrm{P} \tag{2.108}$$

an overall rate constant, k_{tot}, can be defined.

$$\frac{\mathrm{d}[\mathrm{A}\cdots\mathrm{B}]}{\mathrm{dt}} = k_1\,[\mathrm{A}][\mathrm{B}] - k_{-1}\,[\mathrm{A}\cdots\mathrm{B}] - k_2\,[\mathrm{A}\cdots\mathrm{B}] = 0 \tag{2.109}$$

$$[\mathrm{A}\cdots\mathrm{B}] = \frac{k_1}{k_{-1}+k_2}\,[\mathrm{A}][\mathrm{B}] \;\approx\; \frac{k_1}{k_{-1}}\,[\mathrm{A}][\mathrm{B}] \tag{2.110}$$

$$\frac{\mathrm{d}[\mathrm{P}]}{\mathrm{dt}} = k_2[\mathrm{A}\cdots\mathrm{B}] = k_2\,\frac{k_1}{k_{-1}}\,[\mathrm{A}][\mathrm{B}] = k_2 K_c\,[\mathrm{A}][\mathrm{B}] \tag{2.111}$$

$$k_{tot} = k_2 K_c \tag{2.112}$$

The first step employs the SSA by equating the rate of change of the pre-reactive complex to 0. The next step makes the approximation that $k_{-1} >> k_2$, i.e. it is much more likely for the pre-reactive complex to disassociate rather than carry out the reaction. The third step expresses the total reaction rate using quantities related to the first step of the reaction. The final rate constant can then be written as

$$k = \kappa \frac{k_B T}{h} \frac{q_{\mathrm{TS}}/V}{\prod_i^{\mathrm{R}} (q_i/V)^{\nu_i}} e^{-(E_{\mathrm{TS}} - E_{\mathrm{R}})/k_B T} \tag{2.113}$$

where the equilibrium constant is defined by the transition state and the reactants rather than the pre-reactive complex.

Chapter 3

The Atmospheric Importance of Methylamine Additions to Criegee Intermediates [1]

[1] Mull, H.F., G.J.R. Aroeira, J.M. Turney, and H.F. Schaefer III. 2020. *Physical Chemistry Chemical Physics*. 22:22555–22566. Reprinted here with permission of the publisher.

3.1 Abstract

Criegee intermediates are important targets for study in atmospheric chemistry because of their capacity to oxidize airborne species. Among these species, ammonia has received critical attention for its presence in polluted agricultural or industrial areas and its role in forming particulate matter and condensation nuclei. Although methylamine has been given less attention than ammonia, both theoretical and experimental studies have demonstrated that the additional methyl substitution on the ammonia derivatives increases the rate constants for some systems. This suggests that the methylamine addition to Criegee intermediates could be more significant to atmospheric processes. In this work, geometries are optimized at the DF-CCSD(T)/ANO1 level for the methylamine addition reactions to the simplest Criegee intermediate and the *anti*- and *syn*-methylated Criegee intermediates. Energies for each stationary point were computed at the CCSD(T)/CBS level with corrections from the CCSDT(Q) method. Rate constants are obtained for each reaction using canonical transition state theory. Although methylamine addition proved to be a more favorable reaction relative to ammonia addition, the significantly lower concentration of atmospheric methylamine limits the prevalence of these reactions, even in the most optimal conditions. It is unlikely that the methylamine addition to Criegee intermediates will contribute significantly to the consumption of Criegee intermediates in the atmosphere.

3.2 Introduction

Criegee intermediates (CIs) have been the focus of many atmospheric chemistry studies in recent years for the wide range of potential impacts on the atmosphere. They are a class of carbonyl oxides which are formed primarily through the ozonolysis of alkenes in the atmosphere, the mechanism for which was first proposed by Rudolph

Criegee in 1949,[19] but they can also be formed through the reaction of peroxy radicals with OH,[20] Br,[21] or Cl radicals.[22] Their highly-reactive and short-lived nature make them difficult targets for experimental studies; however, laboratory techniques to produce CIs have allowed for direct and indirect measurements of CI concentrations and the rate constants of different reaction pathways.[23–32] These experimental studies have been motivated and driven by corresponding theoretical studies, and together they give valuable insight towards the fates of CIs and their effects on the atmosphere.

Part of the importance of CIs in the atmosphere comes from the increased oxidizing capacity of the air as a result of the presence of these species.[33] These reactions are particularly important at times when photochemical reactions are less likely to occur, such as at night or during winter months.[23,34,35] These contributions to the oxidation capacity can occur through a unimolecular transformation, or the intermediates can directly oxidize a variety of airborne species. A majority of the CIs formed will undergo unimolecular decomposition, generating a variety of organic gasses, radicals, and acids,[25,28,36,37] or they can isomerize to form various organic products.[38] Alternatively, the CIs can be collisionally stabilized to form stabilized Criegee intermediates (SCIs) which can survive long enough to further react.[39] A large number of both experimental and theoretical studies have been performed on a variety of atmospheric species including H_2O,[27,31,40–44] CH_4,[45] MeOH,[46] SO_2,[23–25,37,47–49] NO,[48] NO_2,[24,26] NH_3,[29,30,50,51] and $MeNH_2$.[30,52] The majority of SCIs in the atmosphere will be consumed in reactions with water; however, the reactions with other atmospheric species are still possible and are often of greater interest.[48] These sets of reactions can result in the production of particulate matter and cloud condensation nuclei, which are important factors in understanding the air quality and climate of an area.[53–55]

Previous studies of the reaction between SCIs and ammonia or ammonia derivatives show that these reactions have a negligible role in the consumption of SCIs.

Misiewicz *et al.* investigated the ammonia addition to the simplest SCI and the *anti*- and *syn*-methylated SCIs and determined that this set of reactions would not be able to effectively compete with other similar reactions with more abundant species.[50] This was further confirmed experimentally by Liu *et al.* using OH laser-induced fluorescence[29] and by Chhantyal-Pun *et al.* using cavity ring-down spectroscopy and multiplexed photo-ionization mass spectrometry.[30] However, Kumar and Francisco have recently suggested that increasing the methyl substitution on the ammonia derivative results in a decreased activation barrier.[52] This was also supported experimentally by Chhantyal-Pun *et al.* who found that the reaction between the simplest SCI and methylamine was faster than the corresponding reaction with ammonia.[30] However, Chhantyal-Pun *et al.* only explored the substituent effects of the methylamine, but did not consider the substituent effects of the SCI itself. It has been shown that barrier heights increase and reaction rates decrease with more-substituted SCIs, regardless of the species they are reacting with.[46,50,52] The methylamine addition to simple and methylated SCIs involves both the weakening of the SCI's overall reactivity from increased substitution and the compensation for that loss with the increased reactivity of more-substituted ammonia derivatives. Considering these two effects, the corresponding rates of the reaction could be enhanced to become competitive with the analogous water addition reactions.

Both SCIs and methylamine present their own unique structural challenges. One possible representation of the SCIs is the biradical form with both the terminal oxygen and central carbon having lone electrons. However, Nakajima and Endo experimentally determined the bond lengths and angles of the simplest SCI (CH_2OO) and found that the difference in C-O and O-O bond lengths (1.272 Å and 1.345 Å, respectively) suggested a greater zwitterionic character than biradical character.[32] Additionally, Taatjes *et al.* compared the *syn*- and *anti*- conformers of the methylated SCI and found that the *syn*- conformer was 4 kcal mol^{-1} lower in energy and the interconver-

sion barrier between the two was 40 kcal mol^{-1}, reflecting the zwitterionic character of the SCIs.[31] Methylamine provides a different type of challenge in that both hydrogen atoms are capable of participating in these methylamine addition reactions. This leads to two distinct reaction pathways and starting geometries. In previous work with methylamine, no distinction was made between the two reaction pathways, nor was any justification given for favoring one over the other. Here, the two reaction pathways will be referred to as equatorial and axial. The designations are based on the position of the methylamine methyl group relative to the pseudo five-membered ring formed during the transition state. Equatorial methylamine features the methyl group positioned between the *anti-* and *syn-* positions of the SCI, whereas axial geometries feature the methyl group positioned between the *anti-* position and the double-bond of the SCI (Figure 3.1). Previously, it seems only the axial addition pathway was considered in computational studies, though whether this is coincidence or by design is unclear.[30,52]

(a) Equatorial (b) Axial

Figure 3.1: The equatorial and axial reaction pathways differ by the orientation of the methylamine methyl group relative to the SCI.

In this research, we examine the methylamine addition to the simplest Criegee intermediates (CH_2OO) and the *anti-* and *syn*-methylated Criegee intermediates (CH_3CHOO), both the equatorial and axial pathways, using high-level *ab initio* methods. Energies and rate constants are obtained for each of these reactions to understand the combined effect of the substituents on each reactant and the orientation of addition. Comparing these rate constants will determine their importance in the atmosphere relative to each other as well as other atmospheric species.

3.3 Computational Methods

Each of the geometries investigated was optimized using density-fitted coupled cluster theory with single, double, and perturbative triple excitations [DF-CCSD(T)] with the ANO1 basis set from the atomic natural orbital basis set family,[56] using the ANO1 truncation scheme described by McCaslin and Stanton (C, N, O: [4s 3p 2d 1f]; H: [4s 2p 1s]).[57] Final energies were computed by using the Focal Point Approach (FPA) of Allen and coworkers.[58–60] Restricted Hartree–Fock energies and correlation energies for second-order Møller–Plesset perturbation theory (MP2), CCSD, and CCSD(T) levels of theory were calculated using the Dunning correlation consistent basis sets,[61] cc-pVXZ [X = D, T, Q, 5 for Hartree–Fock energies and X = D, T, Q for MP2, CCSD and CCSD(T)], and then extrapolated to the complete basis set limit (CBS) using a three–point fitting equation for SCF energies[62]

$$E_{\mathrm{SCF}} = A + B\,\exp(-CX) \tag{3.1}$$

and a following two–point fitting equation for correlation energies.[63]

$$E_{\mathrm{corr}} = A + BX^{-3} \tag{3.2}$$

Both the energies and the geometries were computed using the frozen core approximation.

A number of additive corrections were obtained for each of the geometries to account for higher-order correlation and approximations made during the energy computations. Zero-point vibrational energy corrections (Δ_{ZPVE}) were obtained at the DF-CCSD(T) level with the ANO1 basis set for the simple SCI reactions and the ANO0 basis set for the *anti*- and *syn*-SCI reactions. The frozen-core approximation corrective term (Δ_{CORE}) was calculated by taking the difference between the all-

electron and frozen core energies at the CCSD(T) level with a weighted core-valence cc-pwCVTZ basis set.[64]

$$\Delta_{\mathrm{CORE}} = E_{\text{AE-CCSD(T)}} - E_{\text{FC-CCSD(T)}} \tag{3.3}$$

The diagonal Born–Oppenheimer correction (Δ_{DBOC}) was calculated at the CCSD level using the ANO0 basis set.[65,66] Corrections for scalar relativistic effects (Δ_{REL}) were calculated using the spin–free X2C-1e method with an X2C-recontracted correlation consistent cc-pCVTZ basis set.[67–72]

$$\Delta_{\mathrm{REL}} = E_{\text{AE-CCSD(T)/X2C-1e}} - E_{\text{AE-CCSD(T)}} \tag{3.4}$$

Our final energies account for higher order correlation using single-point energies at the CCSDT(Q) level and the Dunning cc-pVDZ basis set[61] for the simplest SCI reactions and, due to their size, the Pople 6-31G* basis set for the *anti*- and *syn*-methylated SCI reactions. It has been shown previously by Aroeira *et al.* that for systems involving SCI's the CCSDT(Q) corrections were approximately twice as large as the CCSDTQ corrections,[46]. Their CCSD(T)/CBS, CCSDT(Q)/CBS, and CCSDTQ/CBS computed heats of formation (ΔH_f^{0K}) for the simplest SCI were 27.12, 25.72, and 26.35 kcal mol^{-1}, respectively. While the full CCSDTQ ΔH_f^{0K} matched well with the Active Thermochemical Tables reference value of 26.74 ± 0.15 kcal mol^{-1}, the CCSD(T) ΔH_f^{0K} was 0.4 kcal mol^{-1} higher and the CCSDT(Q) ΔH_f^{0K} was 1.0 kcal mol^{-1} lower. Recently, Matthews demonstrated the sensitivity of SCIs to higher order corrections by comparing the geometries, energies, and vibrational properties of the simplest SCI using the same methods as above.[73] Again, the CCSDT(Q) results underestimated the CCSDTQ total energy (including Δ_{ZPVE}) by more than 1 kcal mol^{-1}, whereas the CCSD(T) results overestimated the energy by over 2 kcal mol^{-1}. However, these energies were obtained using a structure optimized at their

respectively levels of theory, so part of the discrepancy could be due to the difference in geometries. As seen from these examples, we can consider the CCSD(T) and CCSDT(Q) energies as upper and lower bounds to the true energy, where the difference represents the uncertainty range of the computed energy. For the main purposes of this work, the averaged value will be taken as the computed energy, but these bounds will be considered for some qualitative behavior. Thus the final energy discussed here will only include half of the calculated CCSDT(Q) correction ($\Delta_{\mathrm{T(Q)}}$).

$$\Delta E = \Delta E_{\mathrm{FPA}} + \Delta_{\mathrm{ZPVE}} + \Delta_{\mathrm{CORE}} + \Delta_{\mathrm{DBOC}} + \Delta_{\mathrm{REL}} + \frac{\Delta_{\mathrm{T(Q)}}}{2} \tag{3.5}$$

Geometry optimizations and harmonic vibrational frequency calculations were performed with Psi4.[74] Single-point energies for the FPA were calculated using these geometries in the MOLPRO 2010.1 package.[75,76] Corrective terms other than Δ_{ZPVE} were computed using the CFOUR 2.0 quantum chemistry package.[77,78]

Similarly to previous studies,[46,50] these addition reactions can be represented as

$$\mathrm{SCI} + \mathrm{NH_3} \underset{k_{-1}}{\overset{k_1}{\rightleftharpoons}} \mathrm{SCI \cdots NH_3} \xrightarrow{k_2} \mathrm{P} \tag{3.6}$$

where $\mathrm{SCI \cdots NH_3}$ is a pre-reactive complex and P is the product of the reaction. By employing the Steady State Approximation (SSA),[79] as well as making the assumption of $k_2 << k_{-1}$ which is common for these systems, we can arrive at an expression for our rate constant.

$$\frac{\mathrm{d[SCI \cdots NH_3]}}{\mathrm{dt}} = k_1\,[\mathrm{SCI}][\mathrm{A}] - k_{-1}\,[\mathrm{SCI \cdots NH_3}] - k_2\,[\mathrm{SCI \cdots NH_3}] = 0 \tag{3.7}$$

$$[\mathrm{SCI \cdots NH_3}] = \frac{k_1}{k_{-1} + k_2}\,[\mathrm{SCI}][\mathrm{A}] \approx \frac{k_1}{k_{-1}}\,[\mathrm{SCI}][\mathrm{A}] \tag{3.8}$$

$$\frac{\mathrm{d[P]}}{\mathrm{dt}} = k_2[\mathrm{SCI \cdots NH_3}] = k_2\,\frac{k_1}{k_{-1}}\,[\mathrm{SCI}][\mathrm{A}] = k_2 K_c\,[\mathrm{SCI}][\mathrm{A}] \tag{3.9}$$

$$k_{tot} = k_2 K_c \tag{3.10}$$

Rate constants can then be calculated using canonical transition state theory,[80,81] with the partition functions (q_A) of each species in the reaction

$$k_2 = \kappa \frac{k_B T}{h} \frac{q_{\mathrm{TS}}}{q_{\mathrm{SCI}\cdots\mathrm{NH_3}}} \exp\left(\frac{-E_{\mathrm{TS}}}{RT}\right) \tag{3.11}$$

$$K_c = \frac{q_{\mathrm{SCI}\cdots\mathrm{NH_3}}}{q_{\mathrm{SCI}} q_{\mathrm{NH_3}}} \tag{3.12}$$

$$k_{tot} = \kappa \frac{k_B T}{h} \frac{q_{\mathrm{TS}}}{q_{\mathrm{SCI}} q_{\mathrm{NH_3}}} \exp\left(\frac{-E_{\mathrm{TS}}}{RT}\right) \tag{3.13}$$

where κ is the transmission coefficient for an asymmetric Eckhart potential energy barrier[82]

$$\kappa(T) = \exp\left(\frac{\Delta V_1}{RT}\right) \int_0^\infty \kappa(E) \exp\left(\frac{E}{RT}\right) dE \tag{3.14}$$

k_B is the Boltzmann constant, R is the universal gas constant, T is temperature, and h is Planck's constant. Canonical transition state theory assumes the high pressure limit which eliminates and pressure dependence in the model. These partition functions are approximated as rigid rotor harmonic oscillators (RRHO), allowing for their total partition functions to be separable into different degrees of freedom.

$$q = q_{trans} q_{rot} q_{vib} q_{elec} \tag{3.15}$$

3.4 Results and Discussion

3.4.1 Geometries

Optimized geometries of the simple, *anti*-, and *syn*- methylamine additions are shown in Figures 3.2, 3.3, and 3.4, respectively. Bond lengths for the pseudo five-membered ring are included and reported in Å. Both the equatorial and axial reaction pathways are shown for comparison. The pre-reactive complexes of the equatorial and axial *syn*-SCI additions (Figures 3.4a and 3.4b) have a significantly larger C-N distance compared to the simple and *anti*-SCI additions. However, the C-N distances of the

corresponding transition states (Figures 3.4c and 3.4d) are smaller than those of the simple and *anti-* counterparts. The increased structural change that is required to proceed through the reaction reflects the slower reaction rates of the *syn*-SCI addition reactions, a trend which is expected and has been observed for similar systems.[31,33,50] These geometries also support our choice of SCI representation. Our predictions closely match those of Nakajima and Endo who experimentally determined bond lengths and angles for the simple SCI and concluded that it contained more zwitterion character than biradical character.[32] Furthermore, in each of the reaction pathways, the C-O and O-O bond lengths increase as the reaction proceeds to the product, demonstrating the shift to their normal single bond lengths and further supporting the zwitterion representation.

There exist differences between the equatorial and axial reaction pathways. The largest differences are seen in the pre-reactive complexes for each pair. The positioning of the methylamine methyl group affects how it can approach a given SCI, resulting in a decreased C-N distance and an increased O-H distance for the axial pre-reactive complex compared to the equatorial pre-reactive complex. However, in the transition states for each addition pair, the C-N distance for the equatorial pathway becomes slightly smaller than that of the axial pathway. This is likely due to a smaller amount of steric interference between the methyl groups of the methylamine and the SCI in the equatorial transition states. However, the products of each pair of reactions have bond length differences smaller than 0.1 Å. This is not unexpected as the two products for a given SCI only differ by an inversion and rotation of the amino group.

3.4.2 Energetics

The FPA tables for all six reactions are presented in Tables 3.1–3.6 and good convergence towards the complete basis set limit can be observed in all cases. In all cases, the additive corrections for frozen core, Born–Oppenheimer approximation,

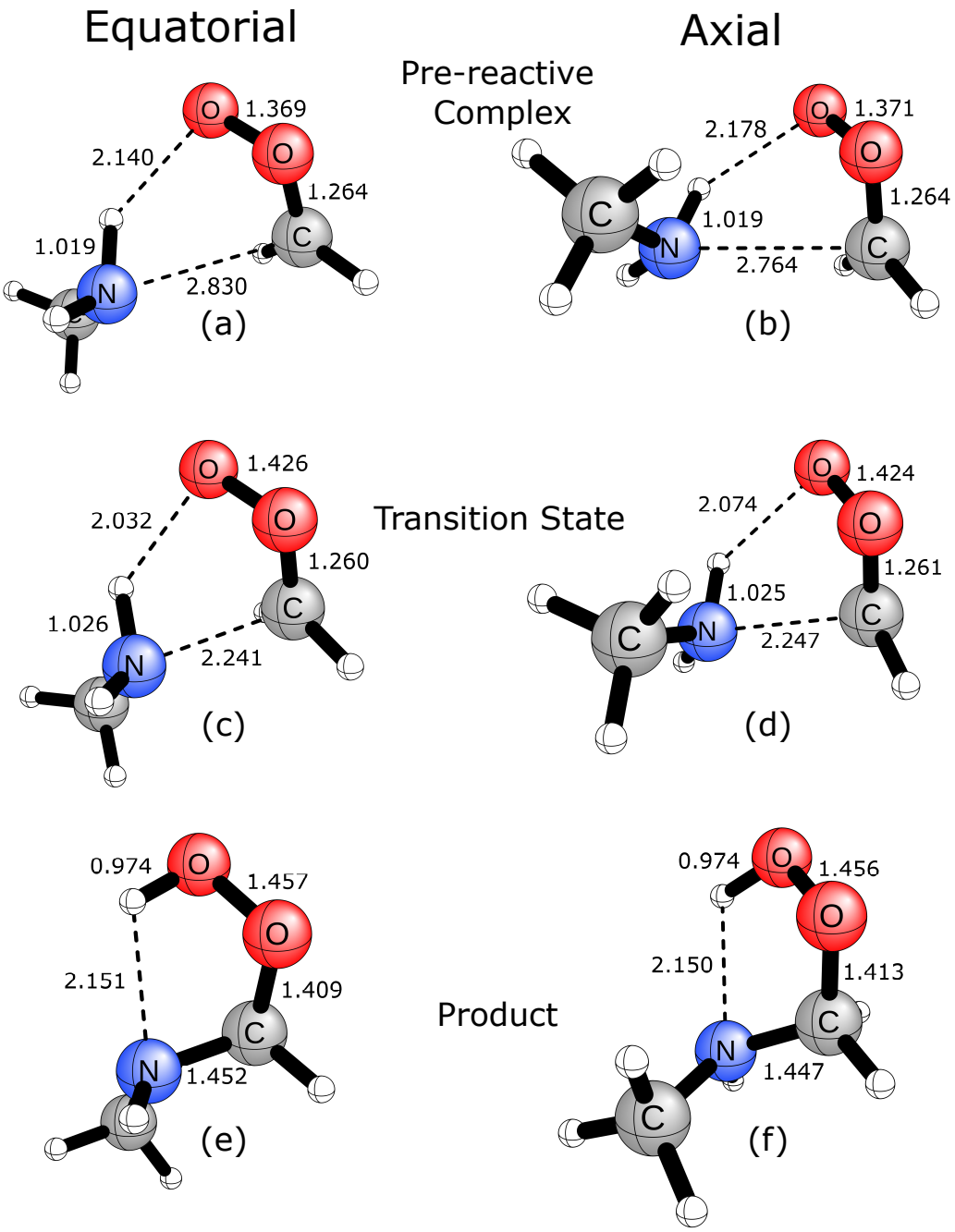

Figure 3.2: Optimized CCSD(T)/ANO1 geometries for the pre-reactive complex, transition state, and product of the methylamine addition to the simple Criegee intermediate. Both the equatorial and axial geometries are shown. Distances are given in Å.

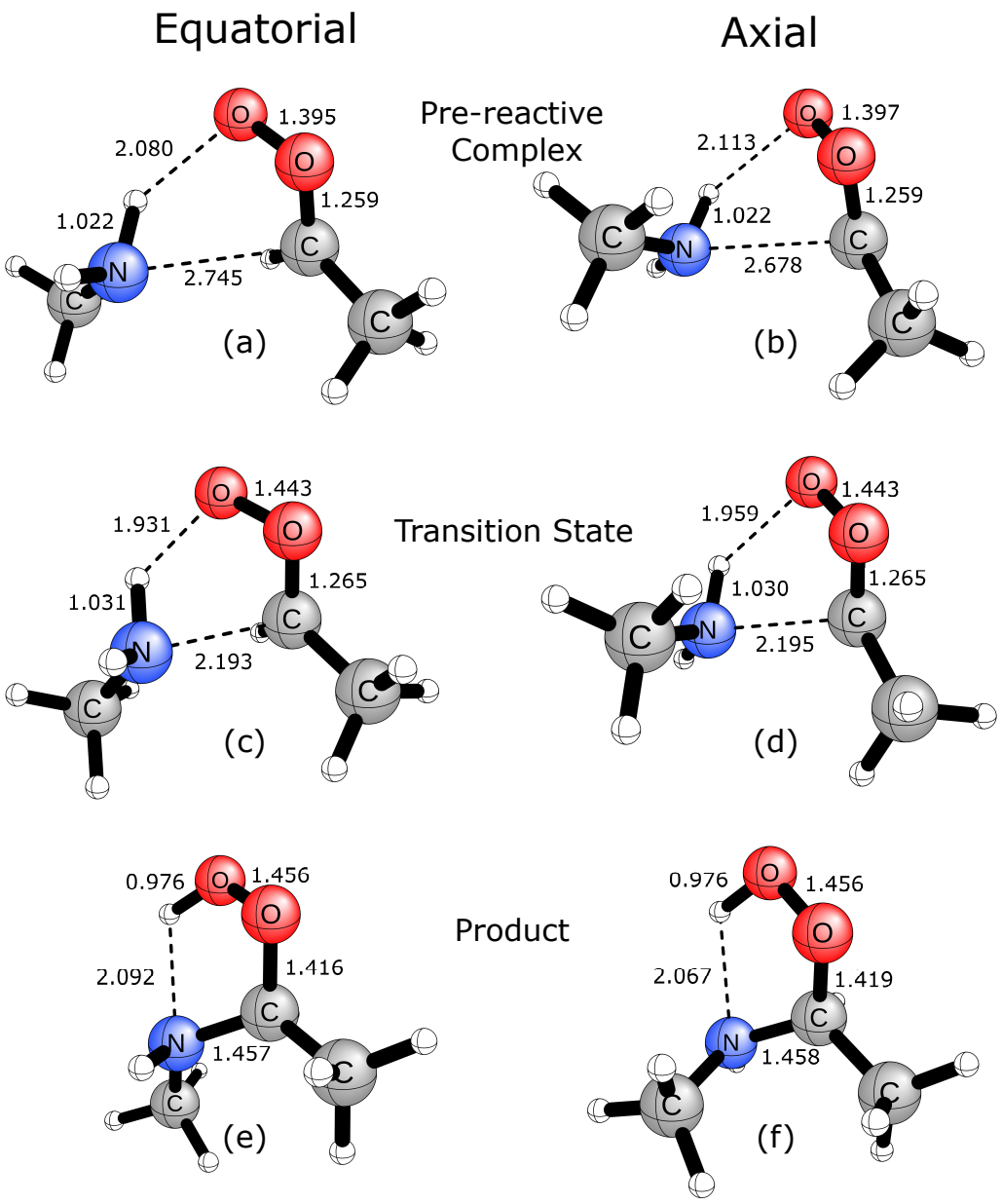

Figure 3.3: Optimized CCSD(T)/ANO1 geometries for the pre-reactive complex, transition state, and product of the methylamine addition to the *anti*- Criegee intermediate. Both the equatorial and axial geometries are shown. Distances are given in Å.

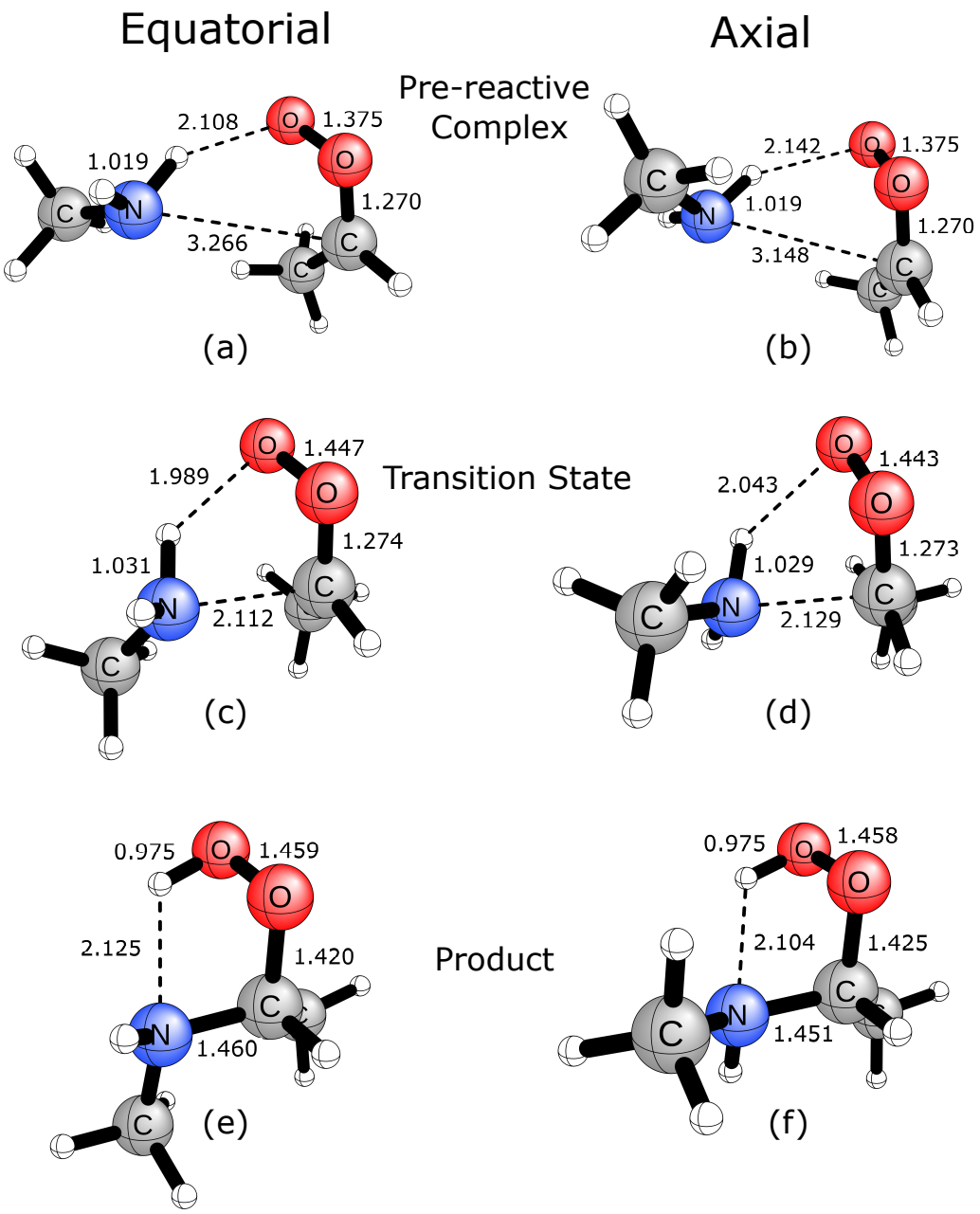

Figure 3.4: Optimized CCSD(T)/ANO1 geometries for the pre-reactive complex, transition state, and product of the methylamine addition to the *syn*- Criegee intermediate. Both the equatorial and axial geometries are shown. Distances are given in Å.

and scalar relativistic effects do not exceed 0.11 kcal mol^{-1}, validating the application of these approximations. As was previously noted, the higher-order energy corrections ($\Delta_{\mathrm{T(Q)}}$) are taken to be half of the CCSDT(Q) correction to account for the overcorrection of perturbative quadruple excitations relative to full quadruple excitations. Even with this reduction, the higher-order correction can still range from 0.11 to 0.63 kcal mol^{-1}, leading to slight qualitative changes of the potential surface. Our energies are in fairly good agreement with the work done previously by Chhantyal-Pun *et al.*[30] for the axial addition to the simplest SCI using CCSD(T)(F12*)/cc-pVQZ-F12//CCSD(T)(F12*)/cc-pVDZ-F12 energies. However there were some qualitative differences between our work and the work by Kumar and Francisco[52] using CCSD(T)/aug-cc-pVTZ//M06-2X/aug-cc-pVTZ energies, with their barrier heights being lower by at least 0.4 kcal mol^{-1} and up to 1.7 kcal mol^{-1}. If the lower bound of the energies are considered (i.e. without any higher-order correction), the barrier heights are still lower by 0.3 kcal mol^{-1} and up to 1.0 kcal mol^{-1}. Towards the upper bound, the energy differences stemming from higher-order corrections are even further exaggerated and would only increase the difference in barrier height.

The potential energy surfaces for each SCI are shown in Figures 3.5–3.7. The equatorial and axial methylamine additions to the simplest SCI have barrier heights of 1.49 kcal mol^{-1} and 1.28 kcal mol^{-1}, respectively. These values only change slightly with the addition of the methyl group at the *anti-* position of the SCI, with barrier heights of 2.13 kcal mol^{-1} and 1.78 kcal mol^{-1}, respectively. This similarity between the two SCIs is expected and has been seen in studies with other systems.[50,52] The barrier heights for the addition to the *syn*-methylated SCIs are 5.49 kcal mol^{-1} for the equatorial addition and 5.03 kcal mol^{-1} for the axial additions. With the SCI methyl group being positioned closer to the oxygen where the hydrogen transfer occurs, significantly more energy is required for the reaction to proceed. This is consistent with the geometries in Figures 3.4c and 3.4d, which have much longer

bond distances than their simple SCI and *anti*-methylated SCI counterparts. The equatorial addition to the *syn*-methylated SCI has the only non-submerged barrier of this group of reactions; however, it is only 0.45 kcal mol^{-1} and would be unlikely to significantly hinder the reaction from occurring. It is worth noting that if the full $\Delta_{T(Q)}$ correction was included, the axial addition to the *syn*-methylated SCI would no longer be submerged, but the transition state would be above the reactants only by 0.03 kcal mol^{-1} and would not significantly hinder the reaction from occurring.

3.4.3 Kinetics

Using the final energies and the theoretical frequencies, rate constants for each reaction were calculated and are presented in Table 3.7. Tunneling does not make significant contributions to these reactions, as the transmission coefficients (κ) only range from 1.044 to 1.089 (Table 3.8). For the rate constant of the axial methylamine addition to the simplest SCI, our value was in relatively good agreement with a previously calculated value from Chhantyal-Pun *et al.* of 5.6×10^{-12} cm^3 s^{-1} using a micro-canonical master equation,[30] giving us greater confidence in our calculated rate constants for the other five reactions. In the cases of the simple and *anti*-methylated SCIs, the axial addition pathway would be preferred, consistent with our calculated energies and barrier heights. The lowered barrier height and increased reaction rate is likely due to a small stabilizing attractive force between the methyl group of the methylamine and the central oxygen atom. This positions the nitrogen of the methylamine closer to the central carbon of the SCI, so the geometry of the pre-reactive complex and transition state for the axial addition are more similar that those of the equatorial addition, reducing the amount of energy needed for the reaction to proceed. Although a similar case can be made for the methylamine addition to the *syn*-methylated SCI, the small interaction is overshadowed by the additional burden of having to rotate and shift the SCI methyl group.

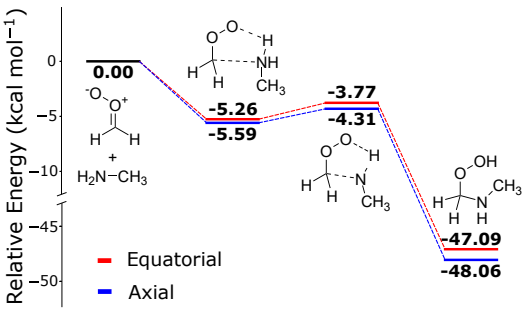

Figure 3.5: Enthalpies at 0 K for the methylamine addition to the simplest Criegee intermediate. Energies are computed at CCSD(T)/CBS//DF-CCSD(T)/ANO1 with additive corrections for the zero-point vibrational energy, frozen core approximation, diagonal Born–Oppenheimer correction, scalar relativistic effects, and perturbative quadruple excitations.

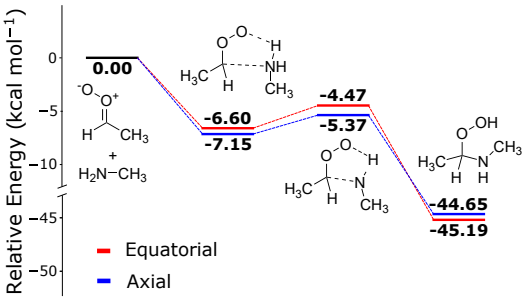

Figure 3.6: Enthalpies at 0 K for the methylamine addition to the *anti*-methylated Criegee intermediate. Energies are computed at CCSD(T)/CBS//DF-CCSD(T)/ANO1 with additive corrections for the zero-point vibrational energy, frozen core approximation, diagonal Born–Oppenheimer correction, scalar relativistic effects, and perturbative quadruple excitations.

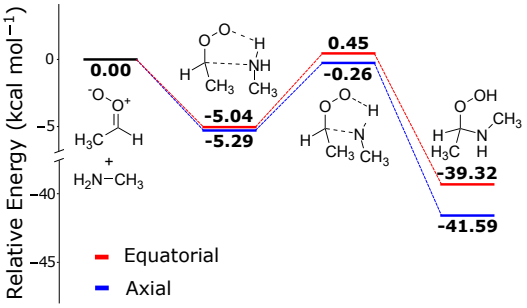

Figure 3.7: Enthalpies at 0 K for the methylamine addition to the *syn*-methylated Criegee intermediate. Energies are computed at CCSD(T)/CBS//DF-CCSD(T)/ANO1 with additive corrections for the zero-point vibrational energy, frozen core approximation, diagonal Born–Oppenheimer correction, scalar relativistic effects, and perturbative quadruple excitations.

Table 3.1: Focal point table for the equatorial addition of methylamine to the simple Criegee intermediate. Energies are given in kcal mol^{-1}. All energies are relative to their isolated reactants (methylamine and the corresponding Criegee intermediate). Final energies in kcal mol^{-1} are presented as $\Delta E = \Delta E_{\mathrm{FPA}} + \Delta_{\mathrm{ZPVE}} + \Delta_{\mathrm{CORE}} + \Delta_{\mathrm{DBOC}} + \Delta_{\mathrm{REL}} + \frac{1}{2}\Delta_{\mathrm{T(Q)}}$.

Basis Set	ΔE_e RHF	δ MP2	δ CCSD	δ CCSD(T)	ΔE_e Net
Pre-reactive Complex					
cc-pVDZ	−10.87	+2.18	+0.14	+0.96	−7.59
cc-pVTZ	−9.17	+1.04	+0.01	+0.79	−7.33
cc-pVQZ	−8.46	+0.82	−0.16	+0.69	−7.11
cc-pV5Z	−8.08	[+0.74]	[−0.22]	[+0.65]	[−6.92]
CBS	[−7.85]	[+0.65]	[−0.28]	[+0.61]	[**−6.87**]
$\Delta E = -6.87 + 1.43 + 0.00 - 0.01 + 0.01 + 0.19 = \mathbf{-5.26}$					
Transition State					
cc-pVDZ	−11.70	+3.51	+1.45	+1.49	−5.25
cc-pVTZ	−9.23	+1.08	+1.05	+1.19	−5.90
cc-pVQZ	−8.44	+0.56	+0.72	+1.00	−6.16
cc-pV5Z	−8.04	[+0.37]	[+0.61]	[+0.93]	[−6.13]
CBS	[−7.80]	[−0.18]	[+0.48]	[+0.85]	[**−6.28**]
$\Delta E = -6.28 + 2.09 + 0.04 - 0.03 + 0.01 + 0.40 = \mathbf{-3.77}$					
Product					
cc-pVDZ	−60.07	−1.14	+4.46	+3.87	−52.88
cc-pVTZ	−56.82	−3.23	+3.54	+3.53	−52.98
cc-pVQZ	−55.60	−3.32	+2.95	+3.45	−52.51
cc-pV5Z	−55.01	[−3.35]	[+2.73]	[+3.43]	[−52.20]
CBS	[−54.67]	[−3.38]	[+2.51]	[+3.40]	[**−52.14**]
$\Delta E = -52.14 + 4.44 - 0.08 - 0.04 + 0.11 + 0.63 = \mathbf{-47.09}$					

Table 3.2: Focal point table for the axial addition of methylamine to the simple Criegee intermediates. Energies are given in kcal mol^{-1}. All energies are relative to their isolated reactants (methylamine and the corresponding Criegee intermediate). Final energies in kcal mol^{-1} are presented as $\Delta E = \Delta E_{\mathrm{FPA}} + \Delta_{\mathrm{ZPVE}} + \Delta_{\mathrm{CORE}} + \Delta_{\mathrm{DBOC}} + \Delta_{\mathrm{REL}} + \frac{1}{2}\Delta_{\mathrm{T(Q)}}$.

Basis Set	ΔE_e RHF	δ MP2	δ CCSD	δ CCSD(T)	ΔE_e Net
Pre-reactive Complex					
cc-pVDZ	−10.86	+1.97	+0.20	+0.91	−7.77
cc-pVTZ	−9.14	+0.64	+0.13	+0.73	−7.64
cc-pVQZ	−8.42	+0.34	−0.01	+0.62	−7.48
cc-pV5Z	−8.05	[+0.23]	[−0.07]	[+0.58]	[−7.31]
CBS	[−7.83]	[+0.11]	[−0.12]	[+0.54]	[**−7.29**]
$\Delta E = -7.29 + 1.53 + 0.00 - 0.01 + 0.01 + 0.19 = \mathbf{-5.59}$					
Transition State					
cc-pVDZ	−11.88	+3.28	+1.45	+1.45	−5.70
cc-pVTZ	−9.42	+0.68	+1.11	+1.14	−6.49
cc-pVQZ	−8.61	+0.07	+0.81	+0.93	−6.81
cc-pV5Z	−8.21	[−0.15]	[+0.70]	[+0.85]	[−6.81]
CBS	[−7.98]	[−0.38]	[+0.59]	[+0.77]	[**−6.99**]
$\Delta E = -6.99 + 2.27 + 0.04 - 0.03 + 0.01 + 0.39 = \mathbf{-4.31}$					
Product					
cc-pVDZ	−60.71	−1.46	+4.57	+3.86	−53.74
cc-pVTZ	−57.42	−3.65	+3.70	+3.49	−53.87
cc-pVQZ	−56.14	−3.78	+3.11	+3.40	−53.41
cc-pV5Z	−55.56	[−3.83]	[+2.90]	[+3.37]	[−53.11]
CBS	[−55.22]	[−3.88]	[+2.68]	[+3.34]	[**−53.08**]
$\Delta E = -53.08 + 4.42 - 0.09 - 0.04 + 0.11 + 0.63 = \mathbf{-48.06}$					

Table 3.3: Focal point table for the equatorial addition of methylamine to the *anti*-methylated Criegee intermediate. Energies are given in kcal mol^{-1}. All energies are relative to their isolated reactants (methylamine and the corresponding Criegee intermediate). Final energies in kcal mol^{-1} are presented as $\Delta E = \Delta E_{\mathrm{FPA}} + \Delta_{\mathrm{ZPVE}} + \Delta_{\mathrm{CORE}} + \Delta_{\mathrm{DBOC}} + \Delta_{\mathrm{REL}} + \frac{1}{2}\Delta_{\mathrm{T(Q)}}$.

Basis Set	ΔE_e RHF	δ MP2	δ CCSD	δ CCSD(T)	ΔE_e Net
Pre-reactive Complex					
cc-pVDZ	−11.78	+0.39	+0.88	+0.77	−9.74
cc-pVTZ	−9.53	−0.87	+0.68	+0.52	−9.20
cc-pVQZ	−8.69	−1.01	+0.46	+0.41	−8.83
cc-pV5Z	−8.24	[−1.05]	[+0.38]	[+0.37]	[−8.54]
CBS	[−7.96]	[−1.11]	[+0.30]	[+0.32]	**[−7.12]**
$\Delta E = -8.44 + 1.65 + 0.00 - 0.02 + 0.00 + 0.20 = \mathbf{-6.60}$					
Transition State					
cc-pVDZ	−8.93	−1.45	+2.63	+0.69	−7.06
cc-pVTZ	−5.90	−3.96	+2.29	+0.25	−7.32
cc-pVQZ	−4.95	−4.31	+1.95	+0.05	−7.25
cc-pV5Z	−4.46	[−4.43]	[+1.83]	[−0.02]	[−7.08]
CBS	[−4.18]	[−4.56]	[+1.70]	[−0.09]	**[−7.12]**
$\Delta E = -7.12 + 2.31 + 0.05 - 0.04 + 0.02 + 0.31 = \mathbf{-4.47}$					
Product					
cc-pVDZ	−51.80	−8.51	+5.71	+2.60	−52.06
cc-pVTZ	−48.16	−10.47	+5.02	+2.09	−51.52
cc-pVQZ	−46.85	−10.33	+4.50	+2.02	−50.67
cc-pV5Z	−46.19	[−10.29]	[+4.32]	[+2.00]	[−50.17]
CBS	[−45.81]	[−10.24]	[+4.12]	[+1.97]	**[−49.95]**
$\Delta E = -49.95 + 4.33 - 0.05 - 0.04 + 0.10 + 0.42 = \mathbf{-45.19}$					

Table 3.4: Focal point table for the axial addition of methylamine to the *anti*-methylated Criegee intermediate. Energies are given in kcal mol^{-1}. All energies are relative to their isolated reactants (methylamine and the corresponding Criegee intermediate). Final energies in kcal mol^{-1} are presented as $\Delta E = \Delta E_{\mathrm{FPA}} + \Delta_{\mathrm{ZPVE}} + \Delta_{\mathrm{CORE}} + \Delta_{\mathrm{DBOC}} + \Delta_{\mathrm{REL}} + \frac{1}{2}\Delta_{\mathrm{T(Q)}}$.

Basis Set	ΔE_e RHF	δ MP2	δ CCSD	δ CCSD(T)	ΔE_e Net
Pre-reactive Complex					
cc-pVDZ	−11.51	−0.19	+1.04	+0.69	−9.98
cc-pVTZ	−9.23	−1.76	+0.92	+0.41	−9.66
cc-pVQZ	−8.38	−2.01	+0.74	+0.28	−9.38
cc-pV5Z	−7.95	[−2.10]	[+0.67]	[+0.23]	[−9.14]
CBS	[−7.69]	[−2.19]	[+0.61]	[+0.18]	**[−9.09]**
$\Delta E = -9.09 + 1.76 + 0.00 - 0.02 + 0.00 + 0.20 = \mathbf{-7.15}$					
Transition State					
cc-pVDZ	−9.03	−1.97	+2.73	+0.63	−7.64
cc-pVTZ	−6.00	−4.80	+2.47	+0.16	−8.18
cc-pVQZ	−5.02	−5.25	+2.16	−0.06	−8.17
cc-pV5Z	−4.54	[−5.41]	[+2.06]	[−0.14]	[−8.04]
CBS	[−4.26]	[−5.57]	[+1.94]	[−0.22]	**[−8.12]**
$\Delta E = -8.12 + 2.43 + 0.04 - 0.04 + 0.02 + 0.30 = \mathbf{-5.37}$					
Product					
cc-pVDZ	−50.73	−9.06	+5.82	+2.58	−51.38
cc-pVTZ	−46.99	−11.13	+5.19	+2.03	−50.90
cc-pVQZ	−45.64	−11.09	+4.69	+1.94	−50.10
cc-pV5Z	−44.99	[−11.07]	[+4.51]	[+1.91]	[−49.64]
CBS	[−44.60]	[−11.05]	[+4.33]	[+1.87]	**[−49.46]**
$\Delta E = -49.46 + 4.39 - 0.07 - 0.05 + 0.11 + 0.42 = \mathbf{-44.65}$					

Table 3.5: Focal point table for the equatorial addition of methylamine to the *syn*-methylated Criegee intermediate. Energies are given in kcal mol^{-1}. All energies are relative to their isolated reactants (methylamine and the corresponding Criegee intermediate). Final energies in kcal mol^{-1} are presented as $\Delta E = \Delta E_{\mathrm{FPA}} + \Delta_{\mathrm{ZPVE}} + \Delta_{\mathrm{CORE}} + \Delta_{\mathrm{DBOC}} + \Delta_{\mathrm{REL}} + \frac{1}{2}\Delta_{\mathrm{T(Q)}}$.

Basis Set	ΔE_e RHF	δ MP2	δ CCSD	δ CCSD(T)	ΔE_e Net
Pre-reactive Complex					
cc-pVDZ	-8.43	-0.59	$+0.50$	$+0.35$	-8.18
cc-pVTZ	-6.46	-1.45	$+0.41$	$+0.16$	-7.35
cc-pVQZ	-5.68	-1.50	$+0.27$	$+0.09$	-6.82
cc-pV5Z	-5.31	$[-1.52]$	$[+0.22]$	$[+0.06]$	$[-6.54]$
CBS	$[-5.09]$	$[-1.54]$	$[+0.17]$	$[+0.04]$	$[\mathbf{-6.42}]$
$\Delta E = -6.42 + 1.29 - 0.01 - 0.02 + 0.01 + 0.11 = \mathbf{-5.04}$					
Transition State					
cc-pVDZ	-4.36	-0.87	$+2.34$	$+0.65$	-2.24
cc-pVTZ	-1.21	-3.35	$+1.95$	$+0.31$	-2.31
cc-pVQZ	-0.28	-3.68	$+1.62$	$+0.13$	-2.21
cc-pV5Z	$+0.13$	$[-3.79]$	$[+1.51]$	$[+0.06]$	$[-2.09]$
CBS	$[+0.36]$	$[-3.91]$	$[+1.39]$	$[+0.00]$	$[\mathbf{-2.16}]$
$\Delta E = -2.16 + 2.24 + 0.08 - 0.04 + 0.02 + 0.30 = \mathbf{0.45}$					
Product					
cc-pVDZ	-47.82	-6.36	$+4.80$	$+2.81$	-46.59
cc-pVTZ	-44.23	-7.78	$+3.99$	$+2.46$	-45.55
cc-pVQZ	-42.96	-7.58	$+3.49$	$+2.43$	-44.62
cc-pV5Z	-42.38	$[-7.51]$	$[+3.31]$	$[+2.42]$	$[-44.16]$
CBS	$[-42.06]$	$[-7.43]$	$[+3.12]$	$[+2.41]$	$[\mathbf{-43.96}]$
$\Delta E = -43.96 + 4.19 - 0.03 - 0.03 + 0.10 + 0.41 = \mathbf{-39.32}$					

Table 3.6: Focal point table for the axial addition of methylamine to the *syn*-methylated Criegee intermediate. Energies are given in kcal mol^{-1}. All energies are relative to their isolated reactants (methylamine and the corresponding Criegee intermediate). Final energies in kcal mol^{-1} are presented as $\Delta E = \Delta E_{\mathrm{FPA}} + \Delta_{\mathrm{ZPVE}} + \Delta_{\mathrm{CORE}} + \Delta_{\mathrm{DBOC}} + \Delta_{\mathrm{REL}} + \frac{1}{2}\Delta_{\mathrm{T(Q)}}$.

Basis Set	ΔE_e RHF	δ MP2	δ CCSD	δ CCSD(T)	ΔE_e Net
Pre-reactive Complex					
cc-pVDZ	-8.54	-0.74	$+0.53$	$+0.31$	-8.44
cc-pVTZ	-6.46	-1.69	$+0.47$	$+0.12$	-7.55
cc-pVQZ	-5.63	-1.76	$+0.34$	$+0.05$	-7.01
cc-pV5Z	-5.25	$[-1.79]$	$[+0.29]$	$[+0.02]$	$[-6.73]$
CBS	$[-5.03]$	$[-1.82]$	$[+0.24]$	$[-0.01]$	$[\mathbf{-6.62}]$
$\Delta E = -6.62 + 1.24 - 0.01 - 0.02 + 0.01 + 0.11 = \mathbf{-5.29}$					
Transition State					
cc-pVDZ	-5.08	-0.59	$+2.19$	$+0.67$	-2.81
cc-pVTZ	-2.01	-3.17	$+1.85$	$+0.32$	-3.01
cc-pVQZ	-1.06	-3.54	$+1.54$	$+0.14$	-2.93
cc-pV5Z	-0.65	$[-3.68]$	$[+1.43]$	$[+0.07]$	$[-2.83]$
CBS	$[-0.43]$	$[-3.82]$	$[+1.31]$	$[+0.00]$	$[\mathbf{-2.93}]$
$\Delta E = -2.93 + 2.32 + 0.07 - 0.04 + 0.02 + 0.29 = \mathbf{-0.26}$					
Product					
cc-pVDZ	-50.14	-6.18	$+4.88$	$+2.83$	-48.62
cc-pVTZ	-46.51	-7.60	$+4.09$	$+2.48$	-47.54
cc-pVQZ	-45.19	-7.44	$+3.57$	$+2.45$	-46.61
cc-pV5Z	-44.62	$[-7.38]$	$[+3.39]$	$[+2.43]$	$[-46.17]$
CBS	$[-44.30]$	$[-7.31]$	$[+3.20]$	$[+2.42]$	$[\mathbf{-45.99}]$
$\Delta E = -45.99 + 3.97 - 0.05 - 0.04 + 0.10 + 0.41 = \mathbf{-41.59}$					

Table 3.7: Pseudo-first order rate constants for methylamine, ammonia, water, and water dimer addition reactions with Criegee intermediates. Values are calculated at 298 K and under the RRHO approximation. Ammonia is assumed to be at a concentration of 2.5 ppm(v). The mass ratio of methylamine to ammonia is assumed to be 0.026.[83] The water concentration comes from 50% humidity, 298 K and 1 atm. The ratio of water dimer to water is assumed to be 8×10^{-4}.[41] k_{tot} values are presented with units of $cm^3\ s^{-1}$ and k'_{tot} values are presented with units of s^{-1}

	NH_2CH_3 (Eq)	NH_2CH_3 (Ax)	NH_3[a]	H_2O[b]	$(H_2O)_2$[b]
			k_{tot}		
Simple	1.54×10^{-12}	7.34×10^{-12}	5.36×10^{-14}	2.40×10^{-16}	6.60×10^{-12}
anti	4.50×10^{-12}	1.52×10^{-11}	2.73×10^{-14}	1.30×10^{-14}	4.40×10^{-13}
syn	2.59×10^{-15}	2.44×10^{-15}	2.70×10^{-18}	1.98×10^{-19}	2.56×10^{-14}
			k'_{tot}		
Conc.	1.57×10^{-9}	1.57×10^{-9}	1.10×10^{-7}	6.31×10^{-4}	5.05×10^{-7}
Simple	2.42×10^{-21}	1.15×10^{-20}	5.90×10^{-21}	1.51×10^{-19}	3.33×10^{-18}
anti	7.06×10^{-21}	2.38×10^{-20}	3.00×10^{-21}	8.20×10^{-18}	2.22×10^{-19}
syn	4.06×10^{-24}	3.83×10^{-24}	2.97×10^{-25}	1.25×10^{-22}	1.29×10^{-20}

[a]Ref 50; [b]Refs 42–44

Table 3.8: Transmission coefficients (κ) for each addition pathway

Pathway	Simple	*anti*	*syn*
Equatorial	1.047	1.044	1.089
Axial	1.043	1.054	1.087

The effects of methyl substitution can be clearly seen when comparing the rate constants of the methylamine additions to the analogous ammonia addition reactions. Rate constants for the preferred axial addition pathway, ammonia addition reactions,[50] water additions, and water dimer additions are compared in Table 3.7. In all cases, the rate constants for the methylamine addition are significantly greater than those for ammonia and are even comparable to the catalysed water dimer reactions.[43,44]

In order to assess the importance of these addition reactions in the atmosphere, it is helpful to treat these reactions as pseudo-first order reactions. These reactions

can all be described by the rate law

$$\text{rate} = k_{tot}[\text{A}][\text{SCI}] \tag{3.16}$$

However, if we assume that the concentration of species A remains constant in the atmosphere, which is reasonable considering the small concentration of SCIs in the atmosphere, we can then use the pseudo-first order rate law

$$\text{rate}' = k'_{tot}[\text{SCI}] \tag{3.17}$$

which more accurately describes the consumption of SCIs in the atmosphere. Here, an ammonia concentration of 2.5 ppm(v) is assumed based on the work of Jørgenson and Gross[51] with rate constants calculated by Misiewicz *et al.*[50] The mass ratio of methylamine to ammonia is assumed to be 0.026 which is based on high-resolution modeling of atmospheric amines in chemical-industrial regions in China.[83] The water concentration is calculated by assuming 50% humidity with a water dimer to water ratio of 8×10^{-4}.[41] From this, we can see that while the pseudo-first order rate constants for methylamine are greater than those of ammonia by approximately an order of magnitude, they still would not be able to effectively compete with the removal of SCIs by just water alone.

If we were to consider the lower bound of our uncertainty range, where the barrier heights are smaller which result in faster reaction rates, the rate constants for the simple, *anti*-, and *syn*-SCIs are 2.02×10^{-20}, 3.95×10^{-20}, and 6.24×10^{-24} respectively. The methylamine to ammonia ratio used here is on the higher end of the spectrum and is considerably lower in other areas such as agricultural regions with a ratio of 0.0011. Because of this, it is unlikely that a more sophisticated treatment of the kinetics would increase the rate constants significantly to the point that these addition reactions could effectively compete with more common reactions.

3.5 Conclusion

In this study, we used high-level *ab initio* methods to investigate the addition of methylamine to simple Criegee intermediates and *anti*- and *syn*-methylated Criegee intermediates. Geometries for pre-reactive complexes, transition states, and products were obtained at the DF-CCSD(T)/ANO1 level of theory. Energies for these structures were extrapolated to the CBS limit and included additive corrections for the zero-point vibrational energy, frozen-core approximation, diagonal Born–Oppenheimer correction, scalar relativistic corrections, and higher-order energy corrections. Rate constants for these reactions were calculated using canonical transition state theory and the Steady State Approximation in order to assess the importance of these reactions in the atmosphere.

Of the two reaction pathways that exist for methylamine addition, the axial reaction pathway was found to be preferred. The stationary point geometries were typically lower in energy and the energy barriers were slightly smaller. This was likely due to a small stabilizing interaction between the methyl group of the methylamine and the SCI which is only possible due to the axial orientation of the methylamine. Additionally, it resulted in a more similar pre-reactive complex and transition state than the equatorial counterpart, therefore requiring less energy to proceed with the reaction.

The rate constants for methylamine addition demonstrated how increasing the methyl substitution of the ammonia derivatives positively affects the rate of reaction, increasing by a few orders of magnitude. However, pseudo-first order rate constants which account for the concentration of reactive species in the atmosphere allow for a more direct comparison of the various atmospheric species. These pseudo-first order rate constants, while still larger than those of ammonia, are still significantly less than those for water or the water dimer, and would likely fall short of most

other atmospheric species. Even in the most optimal conditions, it is unlikely for methylamine to significantly affect the concentration of SCIs in the atmosphere.

Chapter 4

The Kinetic Stability of Pentazole [1]

[1]Mull, H.F., J.M. Turney, G.E. Douberly, and H.F. Schaefer III. 2021. *The Journal of Physical Chemistry A*. 125:9092–9098. Reprinted here with permission of the publisher.

4.1 Abstract

The utility of high energy density materials (HEDMs) comes from their thermodynamic properties which arise from specific structural features that contribute to energy storage. Studies of such structural features seek to increase our understanding of these energy storage mechanisms in order to further enhance their properties. High nitrogen containing HEDMs are of particular interest because they are less toxic than traditional HEDMs. Pentazole is the largest of the nitrogen rings which has been synthesized and considered for an HEDM, but few experimental studies exist due to the difficulty involved in the synthesis, and most previous theoretical studies employed composite methods where lower level geometries were used with higher level methods. Here, the decomposition reaction of pentazole is studied. Geometries, fundamental frequencies, and energies for each of the stationary points of the decomposition pathway are computed using *ab initio* methods up to CCSDT(Q). Decomposition rates are calculated over a range of temperatures using canonical transition state theory in order to determine the kinetic stability of pentazole. Based on the present results, it would be difficult for pentazole to act as an HEDM, requiring temperatures close to 200 K to achieve a suitable level of stability.

4.2 Introduction

High energy density materials (HEDMs) are a loose classification of compounds characterized by the capability to release large amounts of energy. The energy is typically released through the relaxation of structural strain or oxidation of the carbon backbone.[84] Consequently, the most common HEDMs are increasingly complex nitrogen-containing heterocycles. Early HEDMs such as TNT (trinitrotoluene) and its chemical successors, RDX (Royal Demolition Explosive) and HMX (High Melting Explosive), embody these characteristics to a small extent.[85] Modern HEDMs

like CL-20[86] and octanitrocubane[87] (ONC) have expanded on these ideas and are considerably more potent (see Figure 4.1).

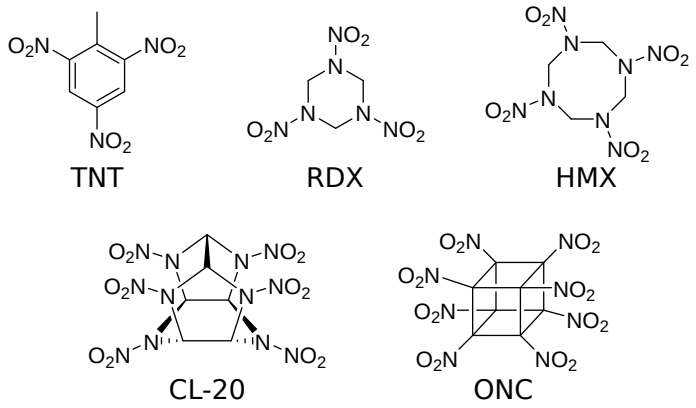

Figure 4.1: Examples of high energy density materials.

These and other HEDMs have been suggested and used for a variety of purposes, including demolition explosives, propellants, and pyrotechnics.[87–92] The issue presented by these types of HEDMs is their toxicity, largely due to the presence of C-NO_X groups (e.g. nitro, nitroso) on both the compounds themselves as well as their decomposition products.[84] Because of these concerns, finding green alternatives for these HEDMs is of particular interest.[90] One current area of focus is in high nitrogen containing HEDMs, such as azoles and azines, which provide a few advantages over conventional HEDMs. Combustion and decomposition of high nitrogen containing HEDMs produce more gas products than other HEDMs, primarily nitrogen and methane gas, and release large amounts of energy due to the presence of multiple nitrogen single and double bonds.[93] While less studied, pentazole (Figure 4.2) has also been proposed as a green HEDM which carries all of these advantages.

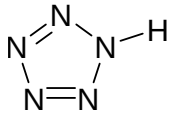

Figure 4.2: Structure of neutral pentazole

The synthesis of pentazoles has faced many challenges over the last century. After repeated failures,[94,95] the first reported synthesis[96] in 1915 was quickly discredited,[97]

and it was only in 1956 when Huisgen and Ugi reported their arylpentazole synthesis.[98] Nearly half a century later, the parent pentazole (R = H) was synthesized in 2003 by Butler, Stephens, and Burke.[99] Since then, the synthesis of pentazole and its derivatives has seen significant advances with crystal structures of pentazole-containing compounds[100–103] and the synthesis of the pentazole anion in solution.[104]

Theoretical studies of pentazole are also important for informing the direction of the synthetic process, particularly so for the purpose of investigating its potency as an HEDM.[105,106] Many theoretical investigations of pentazole focused solely on its characterization (NMR,[107,108] IR[108]), due to the difficulty in synthesizing and subsequent detection of these compounds. Pentazole, as well is its ions, have been previously investigated as potential HEDMs,[89,109–113] though they have also been shown useful for alternative purposes such as an energetic ionic liquid.[114] Only a few smaller pentazole derivatives have been explored using coupled cluster methods, but theoretical studies are often based on composite methods which use high-level methods on DFT geometries so that large substituents (e.g. R = Ph) can be included. Composite methods are able to provide qualitative, and sometimes quantitative, results for geometries and energetics, but it has be shown that small differences in bond distances (e.g. 0.01 Å) can lead to energy differences greater than 1 kcal mol^{-1} with respect to high-level *ab initio* geometries and energies extrapolated to the CBS limit, especially for transition states.[115–117] Burke and Fazen demonstrated this with the two breaking bonds for the pentazole decomposition where the bond differences between CCSD(T) and B3LYP were 0.041 and 0.012 Å.[118] In this case, the energy reported for the parent pentazole only differed by 0.538 kcal mol^{-1}, but these energies were calculated with the same level of theory as they were optimized and not with the full treatment of a composite method or CBS extrapolation which would likely exacerbate the difference. Bo *et al.* report barrier heights for pentazole decomposition in a study of the global potential energy surface of N_5H using the composite methods CBS-QB3 (19.16 kcal mol^{-1}),

G4 theory (18.87 kcal mol^{-1}), and W1BD (19.88 kcal mol^{-1}).[119] While these energies seem to agree with Burke and Fazen, their CCSD(T) value likely only included a ZPVE correction, though it is never explicitly stated, and can be further improved. These differences, as well as the large range over which they span, pose a significant problem when it comes to investigating kinetic properties such as decomposition rates and half-lives, both important to determining the kinetic stabilities of potential HEDMs.

Using canonical transition state theory (CTST), kinetic rates (and by extension, half-lives) are obtained using activation energies and harmonic vibrational frequencies.[80,81] Consequently, the calculated CTST rate constant will be heavily reliant on the level of theory and basis set choice. While the differences in these values may seem small, their effects on the rate constant are exacerbated due to the exponential relationship. At 273 K, a 1 kcal mol^{-1} difference in barrier heights results in a 5-fold difference in rate constant, while a 2 kcal mol^{-1} difference gives a 40-fold difference. It has been suggested that an ideal HEDM would have a free-energy activation barrier of $\sim$30 kcal mol^{-1} with a half-life of $\sim$35 years at room temperature.[89] Recently, it has been proposed via CBS-QB3 calculations that it is possible to achieve this level of kinetic stability for arylpentazole by substituting lewis acids at the *ortho*-positions of the aryl ring.[120] While this has yet to be accomplished experimentally and the size of the molecules makes them cost prohibitive to study with high-level *ab inito* methods, it would significantly increase the utility of pentazole derivatives by making them safer and easier to work with and store. However, this would be difficult to achieve for the parent pentazole or one of its simpler derivatives without external influences, though it is possible that a pentazole compound could become moderately stable at a lower temperature. Previous theoretical studies have reported quantitatively inconsistent barrier heights for pentazole. In order to help direct and inform the synthesis of HEDMs, accurate thermochemical data is required.

In this study, the decomposition pathway of pentazole is explored using high-level *ab initio* methods. Energies and rate constants are computed to determine the overall potency of pentazole as an HEDM, in addition to their kinetic stability, both of which are important to determine their utility as an HEDM.

4.3 Computational Methods

Each of the stationary points investigated was optimized using coupled cluster theory with single, double, and perturbative triple excitations [CCSD(T)] with the cc-pVTZ basis set from the Dunning correlation consistent basis set family.[61,121] Final energies were computed by using the Focal Point Approach (FPA) of Allen and coworkers.[58–60] Restricted Hartree–Fock (RHF) energies and correlation energies from second-order Møller–Plesset perturbation theory (MP2), CCSD, CCSD(T), and CCSDT levels of theory were computed using the cc-pVXZ basis sets [X = D, T, Q, 5 for RHF, MP2, CCSD and CCSD(T); X = D, T, Q for CCSDT], and then extrapolated to the complete basis set limit (CBS) using a three–point fitting equation for SCF energies[62]

$$E_{\mathrm{SCF}} = A + B\,\exp(-CX) \tag{4.1}$$

and a two–point fitting equation for correlation energies.[63]

$$E_{\mathrm{corr}} = A + BX^{-3} \tag{4.2}$$

Both the energies and the geometries were predicted using the frozen core approximation.

A number of additive corrections were obtained for each of the geometries to account for higher-order correlation and approximations made during the energy computations. Harmonic vibrational frequencies were obtained at the CCSD(T)/cc-pVTZ level of theory. Anharmonic corrections to the harmonic frequencies were calculated

using finite differences VPT2. Zero-point vibrational energy corrections (Δ_{aZPVE}) were obtained using the anharmonic fundamental frequencies. The frozen-core approximation corrective term (Δ_{CORE}) was calculated by taking the difference between the all-electron and frozen core energies at the CCSD(T) level with a weighted core-valence cc-pwCVTZ basis set.[122]

$$\Delta_{\mathrm{CORE}} = E_{\text{AE-CCSD(T)}} - E_{\text{FC-CCSD(T)}} \tag{4.3}$$

The diagonal Born–Oppenheimer correction (Δ_{DBOC}) was calculated at the CCSD level using the cc-pVTZ basis set.[65,66] Corrections for scalar relativistic effects (Δ_{REL}) were calculated using the spin–free X2C-1e method with an X2C-recontracted correlation consistent cc-pCVTZ basis set.[67–72]

$$\Delta_{\mathrm{REL}} = E_{\text{AE-CCSD(T)/X2C-1e}} - E_{\text{AE-CCSD(T)}} \tag{4.4}$$

Higher order correlation is accounted for using single-point energies at the CCSDT(Q) level and the Dunning cc-pVTZ basis set.[61]

$$\Delta_{\mathrm{T(Q)}} = E_{\mathrm{CCSDT(Q)}} - E_{\mathrm{CCSDT}} \tag{4.5}$$

Our final energies are calculated by summing the FPA energies with all of the above additional terms.

$$\Delta E = \Delta E_{\mathrm{FPA}} + \Delta_{\mathrm{aZPVE}} + \Delta_{\mathrm{CORE}} + \Delta_{\mathrm{DBOC}} + \Delta_{\mathrm{REL}} + \Delta_{\mathrm{(Q)}} \tag{4.6}$$

All geometry optimizations, single-point energies, corrective term calculations, and frequency calculations were performed using the CFOUR 2.0 quantum chemistry package.[77,78]

This parent pentazole decomposition reaction can be described by the first order reaction:

$$N_5H \xrightarrow{k} N_3H + N_2 \tag{4.7}$$

and the rate constant, k, can be evaluated using canonical transition state theory (CTST):[80,81]

$$k = \kappa(T)\frac{k_B T}{h}\frac{q_{TS}}{q_{N_5H}} \exp\left(\frac{-(E_{TS} - E_{N_5R})}{RT}\right) \tag{4.8}$$

where $\kappa(T)$ is the transmission factor for an asymmetric Eckart potential:[82]

$$\kappa(T) = \exp\left(\frac{\Delta V_1}{RT}\right)\int_0^\infty \kappa(E) \exp\left(\frac{E}{RT}\right) dE \tag{4.9}$$

k_B is the Boltzmann constant, R is the gas constant, T is temperature, h is Planck's constant, and q_A is the partition function for species A. These partition functions are approximated as rigid rotor harmonic oscillators (RRHO), allowing for their total partition functions to be separable into different degrees of freedom:

$$q = q_{trans}q_{rot}q_{vib}q_{elec} \tag{4.10}$$

CTST assumes the high pressure limit, which eliminates any pressure dependence in the model.

4.4 Results and Discussion

4.4.1 Geometries

The bond distances for pentazole and its decomposition pathway are shown in Figure 4.3. Previous studies of pentazole have used a variety of levels of theory and basis sets. There is currently no consensus on whether diffuse functions are necessary for pentazole and its derivatives. Many previous studies did not use diffuse functions for

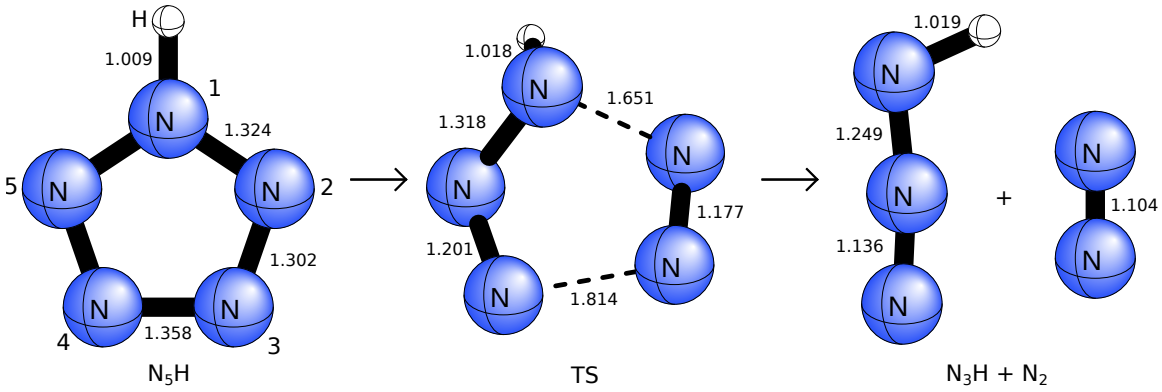

Figure 4.3: The asymmetric pentazole decomposition pathway is shown with bond distances given in Angstroms

their optimizations,[89,113,119,123] and those that did gave no justification for why they were included or necessary.[105,110,114,118] Our re-optimization using the aug-cc-pVTZ Dunning basis set did not result in significant differences of the geometry parameters or the energy relative to the products. Bond distances only changed by 0.002 Å at most and bond angles were identical to 0.1° (see Table S1). Our geometries also did not qualitatively differ from previously reported geometries.[113,118,119]

Pentazole shares a similar level of aromaticity as its anionic counterpart and the π-bonds are largely delocalized over the entire ring. NICS(1.0) index values were calculated for the two species using the ORCA 4.0 program[124,125] and pentazole was found to have a value of -15.519 which was only slightly smaller than the anion's value of -15.954. Natural bond orders were calculated for pentazole and its transition state geometries using the NBO 7.0 program[126] and are shown in Table 4.1. These bond orders reflect the delocalization of the double bonds in the initial pentazole before the breaking and formation of new π-bonds occurs.

4.4.2 Energetics

Energies computed through focal point analysis of the transition state and the products of decomposition relative to pentazole are shown Table 4.2. Including the additive corrections listed previously, the relative enthalpies are 18.80 and -40.17 kcal mol^{-1},

Table 4.1: Natural bond orders for pentazole and its transition state

Parameter	Pentazole	Transition State
N1-N2	1.32	0.75
N2-N3	1.50	2.21
N3-N4	1.29	0.66
N4-N5	1.50	2.06
N5-N1	1.32	1.28

respectively. These energies are plotted in Figure 4.4. While the energies converge smoothly with respect to increasing basis set size, increasing the level of theory gives results which are less well-behaved.

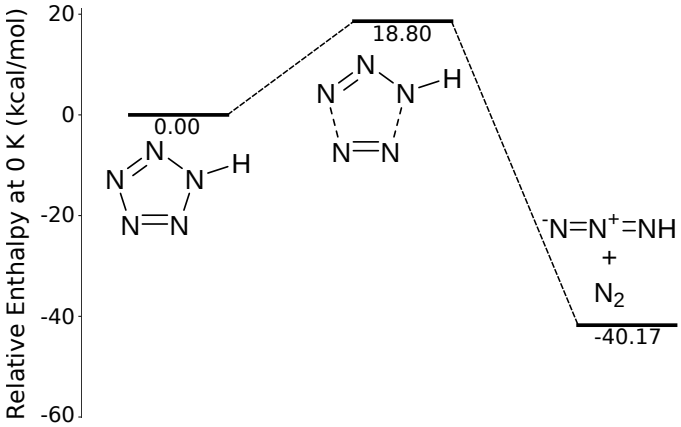

Figure 4.4: Enthalpies at 0 K for the asymmetric pentazole decomposition. Energies are computed at the CCSDT/CBS//CCSD(T)/cc-pVTZ level of theory with additive corrections for the zero-point vibrational energy, frozen-core approximation, diagonal Born–Oppenheimer correction, scalar relativistic effects, and perturbative quadruple excitations

Previously, the most accurate theoretical calculations for these molecules were reported by Bo *et al.* in their study of the N_5H potential energy surface. Using several composite methods, they report the barrier height as 19.16 kcal mol^{-1}, 18.87 kcal mol^{-1}, and 19.88 kcal mol^{-1}for CBS-QB3, G4, and W1BD, respectively. While these composite methods use DFT geometries, they also use CCSD(T) for the energy calculations with additive corrections. However, while CCSD(T) is often touted as the "golden standard" of *ab initio* quantum chemistry methods, it can be seen from

Table 4.2: Focal point tables for the asymmetric pentazole decomposition. Energies are given in kcal mol^{-1}. Final energies are presented as $\Delta E = \Delta E_{\mathrm{FPA}} + \Delta_{\mathrm{aZPVE}} + \Delta_{\mathrm{CORE}} + \Delta_{\mathrm{DBOC}} + \Delta_{\mathrm{REL}} + \Delta_{(\mathrm{Q})}$. Energies in brackets indicate values which have been extrapolated.

Basis Set	ΔE_e RHF	δ MP2	δ CCSD	δ CCSD(T)	δ CCSDT	ΔE_e Net
Transition State						
cc-pVDZ	+36.30	−17.44	+4.02	−4.03	+0.25	+19.10
cc-pVTZ	+37.33	−17.20	+4.69	−4.40	+0.37	+20.79
cc-pVQZ	+37.77	−16.60	+4.95	−4.51	+0.39	+22.00
cc-pV5Z	+37.89	−16.50	+5.05	−4.56	[+0.51]	[+22.39]
CBS	[+37.93]	[−16.40]	[+5.16]	[−4.60]	[+0.63]	[+22.72]
$\Delta E = 22.72 - 2.86 + 0.36 + 0.03 - 0.21 - 1.24 =$ **18.80**						
Products						
cc-pVDZ	−45.63	+7.85	−1.10	+1.76	−0.61	−37.73
cc-pVTZ	−48.42	+11.60	−2.35	+2.52	−0.76	−37.41
cc-pVQZ	−48.45	+13.14	−2.49	+2.75	−0.81	−35.86
cc-pV5Z	−48.48	+13.87	−2.50	+2.86	[−1.06]	[−35.31]
CBS	[−48.49]	[+14.62]	[−2.52]	[+2.96]	[−1.32]	[−34.75]
$\Delta E = -34.75 - 4.81 - 0.19 + 0.03 - 0.19 - 0.26 =$ **−40.17**						

our FPA tables that this is not necessarily the case for this reaction.

With the additive corrections, our computed energy would agreed very well with the G4 energy of Bo *et al.*, but this includes correlation energy that is not explicitly accounted for by the G4 method. The large magnitude of the −1.24 kcal mol^{-1} higher order correction suggests that the energy has yet to converge with respect to the level of theory. If it were not cost prohibitive, the FPA table would ideally extend further out to ensure convergence, or at the very least that the CCSDT(Q) energy captures most of the CCSDTQ correlation energy. Additionally, the CCSDT(Q) correction with the cc-pVDZ basis set is larger −1.05 kcal mol^{-1}, so it is likely that the magnitude of the higher order correction would continue to increase with the basis set size, though only a small change would be expected.

The decomposition products see a similar situation, though the relatively small magnitude of the 0.24 kcal mol^{-1} higher order correction indicates that the energy is better converged with respect to level of theory than that for the transition state.

With the cc-pVDZ basis set, the full CCSDTQ contribution only differs from the CCSDT(Q) contribution by 0.10 kcal mol^{-1}, giving further assurance that the energy has nearly converged. However, the CCSD(T) energy still does not present an accurate description of these products. Stopping at this level overestimates the energy by 1.32 kcal mol^{-1} relative to the full CCSDT energy. Fortunately, this difference has less of an effect on the properties of this reaction since the decomposition rates do not depend on this energy. Additionally, the pentazole geometry was re-optimized at the CCSDT/cc-pVTZ level, but again the bond distances only differed by 0.002 Å at most and bond angles were identical to 0.1°.

This behavior is likely due to these molecules having slight multireference character. CASSCF calculations were performed to assess to what extent this multireference character affected the resulting energies. Due to the size of the molecules, a full-valence active space was not achieved, but getting near that limit still provided useful information. For the pentazole minimum, a CASSCF(16,16) calculation found seven terms in the CI vector with coefficients greater than 0.05. For the transition state, a CASSCF(20,15) calculation found nine terms in the CI vector with coefficients greater than 0.05. These coefficients are shown in Table 4.3. The reference wavefunction configuration vastly outweighs any other determinant; the latter which individually only contribute ∼1% or less to the overall wavefunction. While these and other more minor determinants do not have significant effects by themselves, their large quantities indicates that these molecules have non-trivial dynamic correlation. Thus, it is important to consider higher excitations in the coupled cluster energy in order to capture a more complete correlation energy.

4.4.3 Kinetics

The rate constants for pentazole decomposition was calculated using CTST with RRHO partition functions from 150 K to 300 K and are plotted in Figure 4.5. As

Table 4.3: CI coefficients with their corresponding electron configurations for CASSCF calculations from pentazole and its transition state. The determinants listed are only those whose contributions are greater than 0.05.

Pentazole		Transition State	
Coefficient	Determinant[a]	Coefficient	Determinant[b]
0.9277	$1b_1^2\ 6b_2^2\ 2b_1^2\ 1a_2^2$	0.9055	$15a_1^2\ 16a_1^2\ 17a_1^2\ 18a_1^2$
−0.1116	$1b_1^2\ 6b_2^2\ 2b_1^2\ 3b_1^2$	−0.1308	$15a_1^2\ 16a_1^2\ 17a_1^2\ 19a_1^2$
−0.0937	$1b_1^2\ 6b_2^2\ 1a_2^2\ 2a_2^2$	−0.1137	$15a_1^2\ 16a_1^2\ 18a_1^2\ 20a_1^2$
−0.0617	$1b_1^2\ 6b_2^2\ 2b_1^\alpha\ 1a_2^\beta\ 3b_1^\beta\ 2a_2^\alpha$	−0.1115	$15a_1^2\ 17a_1^2\ 18a_1^2\ 21a_1^2$
−0.0617	$1b_1^2\ 6b_2^2\ 2b_1^\beta\ 1a_2^\alpha\ 3b_1^\alpha\ 2a_2^\beta$	−0.0574	$16a_1^2\ 17a_1^2\ 18a_1^2\ 22a_1^2$
−0.0603	$6b_2^2\ 2b_1^2\ 1a_2^2\ 3b_1^2$	0.0536	$15a_1^2\ 16a_1^\alpha\ 17a_1^\beta\ 18a_1^2\ 21a_1^2$
−0.0594	$1b_1^2\ 6b_2^2\ 2b_1^2\ 2a_2^2$	−0.0536	$15a_1^2\ 16a_1^\beta\ 17a_1^\alpha\ 18a_1^2\ 21a_1^2$
		0.0515	$15a_1^\alpha\ 16a_1^2\ 17a_1^2\ 18a_1^\beta\ 19a_1^\beta\ 22a_1^\alpha$
		0.0515	$15a_1^\beta\ 16a_1^2\ 17a_1^2\ 18a_1^\alpha\ 19a_1^\alpha\ 22a_1^\beta$

[a]The orbitals $7a_1^2\ 8a_1^2\ 5b_2^2\ 9a_1^2$ are also included in the active space
[b]The orbitals $9a_1^2\ 10a_1^2\ 11a_1^2\ 12a_1^2\ 13a_1^2\ 14a_1^2$ are also included in the active space

stated earlier, while it has been suggested that an ideal HEDM would have a half-life of at least 35 years at room temperature,[89] this standard is only achievable for pentazole at 180 K or below. At room temperature, pentazole has a half-life of approximately 1 second, and at 0 °C the half-life is only increased to approximately 24 seconds. Even a half-life of 1 year is only reached at 193 K. Pentazole, on its own, would likely not be stable enough for most applications.

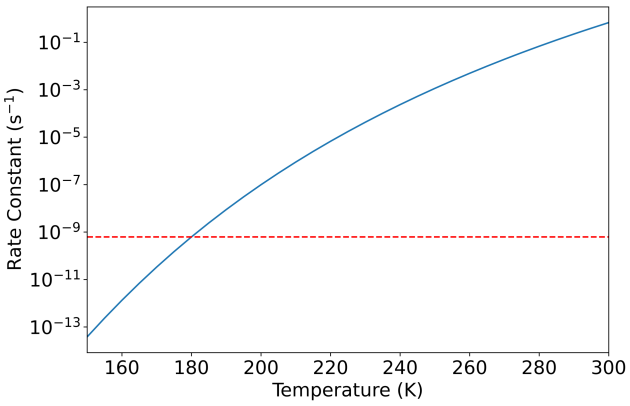

Figure 4.5: The rate constants (s^{-1}) of pentazole decomposition are plotted as a function of temperature (K) using CTST. Anything below the dashed red line indicates a rate constant which corresponds to a half-life of at least 35 years.

CTST is a basic level of transition state theory that neglects more nuanced considerations such as torsional conformers and multi-path transition states. However, these more advanced treatments would not be able to account for the factor of 10^9 which would be required to bring the 298 K rate constant near the magnitude for the desired half-life. Further improving pentazole's prospects as an HEDM would most likely require external assistance. These rate constants and energies assume a gas phase system comprised only of pentazole, but most modern HEDMs would be used in a solid form in a mix with other components for stabilization. It is also possible, in principle, to improve the barrier height through lowering the energy of the pentazole via substitution of the hydrogen. This has been studied previously[100,105,113,118] and the greatest success was seen with large aryl substituents which could draw electron density from the pentazole rings. Unfortunately, these systems would be cost prohibitive to study at the same level of theory presented here.

4.5 Conclusion

The decomposition of the parent pentazole (N_5H) has been studied using high-level *ab initio* techniques. Geometries have been optimized for the minimum structure, transition state, and decomposition products. From these geometries, we computed energies through focal point analysis and obtained anharmonic fundamental frequencies via VPT2. The decomposition rate constant was then calculated as a function of temperature using canonical transition state theory to determine the value of pentazole as an HEDM.

The geometries we obtained were not significantly different from those reported previously. Additionally, we found that there were not significant differences when diffuse functions were included in the basis set which was a decision that was not consistent throughout previous theoretical studies.

Computing the electronic energy of pentazole is a more difficult task than initially anticipated due to the multireference character that arises through the breaking and forming of multiple π-bonds throughout the reaction. It was found that CCSD(T) was not a sufficient treatment of the correlation energy to achieve chemical accuracy. Even with a CCSDT(Q)/cc-pVDZ correction, the energy still changed by more than 1 kcal mol^{-1} for the transition state to give a barrier of activation of 18.8 kcal mol^{-1}. Because this energy agreed with previous composite method results, this study can act as a benchmark and give further confidence in future results; however, care must be take to account for the higher order correlation that is not inherently address with those methods.

Calculating the rate of decomposition over a range of temperatures showed that pentazole would only be moderately kinetically stable close to 200 K. CTST does not provide the most accurate evaluation of a rate constant; however, more extensive treatments like VTST would likely not be able to adjust these calculations enough to make a significant difference. This also assumes a gas phase molecule by itself and would not perfectly describe the kinetic properties of a prepared HEDM, which would be solid and also likely include additional compounds as a mixture. Further theoretical studies on substituted pentazole would be desirable, but is cost prohibitive at this level of electronic structure theory.

Chapter 5

Four Isomers of In_2H_2: A Careful Comparison Between Theory and Experiment [1]

[1]Mull, H.F., P.R. Franke, C. Sargent, G.E. Douberly, J.M. Turney, and H.F. Schaefer III. 2021. *Molecular Physics*. 119:e1979675. Reprinted here with permission of the publisher.

5.1 Abstract

Four constitutional isomers of diindium dihydride have been studied utilizing rigorous quantum mechanical methods. Geometries were optimized with the CCSD(T) method using the aug-cc-pwCVTZ basis set and a small-core pseudopotential for the indium atoms. Relative energetics were determined at the CCSD(T)/CBS level of theory, and the higher order δT(Q) contributions are also computed. The monobridged and vinylidene-like isomers lie 10.8 and 13.6 kcal mol^{-1} above the planar dibridged isomer, respectively. At 0 K, the *trans* isomer is the least favored energetically, differing from the dibridged isomer by 16.6 kcal mol^{-1}. Anharmonic vibrational frequencies were predicted to provide theoretical insight into future experimental studies. Very detailed comparisons are made to the matrix isolation experiments from the group of Downs and the group of Andrews. Numerous agreements and disagreements were found and addressed.

5.2 Introduction

Group 13 hydrides have proven to be challenging systems to study experimentally. This is commonly due to their thermal instability, as noted in important review articles by Downs, Pulham, and Aldridge.[127,128] Although difficult, successful syntheses are motivated by two areas of broader impact. First, the propensity for group 13 hydrides to thermally decompose is the same ability which makes them favorable options for precursors of thin metal films, especially useful in deposition processes for semiconductors.[127] Their thermal fragility and aptitude to deliver the pure metal makes them preferred compounds when compared to conventional organometallics. Secondly, these compounds are useful in synthesis, as they can form complexes with Lewis bases, and can also act as reducing agents.[127] Interest also heightened specifically for dihydride complexes and their use in catalytic hydrogenation reactions.[128–137]

Various *ab initio* techniques have been used to study the dihydrides of aluminum and gallium, Al_2H_2 and Ga_2H_2, valence isoelectronic to In_2H_2. In Figure 5.1, the (a) planar dibridged, (b) monobridged, (c) vinylidene-like, and (d) *trans* structures have been identified as minima for Al_2H_2[138,139] and Ga_2H_2[140] using the CCSD(T) method with different basis sets. Studies have revealed that the relative ordering of the isomer energies for both Al_2H_2 and Ga_2H_2 coincide, with the planar dibridged structures being the lowest in energy. Additionally, these studies have revealed that the vinylidene-like isomers are the next lowest energy minima, followed by the monobridged isomers and finally the *trans* isomers.[138–140] Indium has a larger atomic radius than gallium, perhaps decreasing confidence in the viability of these diindium dihydrides. However, the existing experimental and theoretical evidence provide some hope for locating minima corresponding to these four isomers on the potential energy surface of In_2H_2.

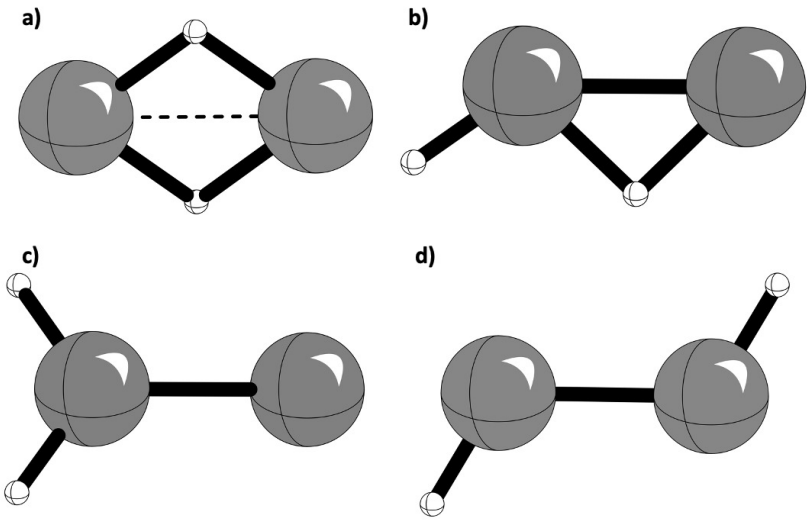

Figure 5.1: Four constitutional isomers of M_2H_2 (M = Al, Ga, In): (a) planar dibridged, (b) monobridged, (c) vinylidene-like, and (d) *trans*.

The synthesis of solid indane $(InH_3)_n$ has been fairly controversial. In 1957, Wiberg claimed to prepare solid $(InH_3)_n$, along with Ga_2H_6 and $(GaH_3)_n$.[141] Fewer

than ten years later, multiple studies had discredited these syntheses.[142–144] Ga_2H_6 and $(GaH_3)_n$ were unable to be synthesized, even after careful effort to reproduce the procedure of Wiberg.[141,143] Additionally, pseudo-equilibrium mass spectrometric studies concluded that InH_3 is less thermodynamically stable than either GaH_3 or AlH_3, and certainly less so than Wiberg claimed.[141,142] No evidence was found for thermal stability of In_2H_6 in the gas phase or the solid phase in a theoretical study by Hunt and Schwerdtfeger employing second-order Møller–Plesset perturbation theory (MP2).[145]

While indium hydrides are rare, there has been experimental evidence of In_2H_2. Within solid argon matrices at 12 K, and irradiated with ultraviolet light (λ= 365 nm), a planar dibridged structure In(μ-H)$_2$In was identified by Himmel, Manceron, Downs, and Pullumbi in 2002.[146,147] Isomerization from the planar dibridged structure to the *trans* structure HInInH apparently occurs with irradiation of visible light, at wavelengths greater than 450 nm. These isomers were interrogated by comparing infrared spectra with theoretical calculations utilizing MP2 and B3PW91 and B3LYP density functionals.[146] In 2004, Wang and Andrews presented an independent spectroscopic study of indium hydrides which concluded that the dibridged isomer In(μ-H)$_2$In was formed through photolysis in both solid hydrogen and solid neon. Weak spectroscopic bands served as evidence for the synthesis of the vinylidene-like $InInH_2$ isomer, different from the *trans* HInInH isomer proposed by Downs and coworkers.[146,148,149] Wang and Andrews' computational results, obtained with B3LYP, suggest that the $InInH_2$ isomer lies lower in energy than HInInH.[148] These conflicting experimental studies, along with the excellent but limited existing theoretical work, demonstrate the need for more rigorous *ab initio* studies of these diindium dihydride species.

Apart from the work of Downs and coworkers noted above, in 1993 Treboux and Barthelat[150] used an *ab initio* SCF + CI method with effective core potentials to investigate monohydrides and dihydrides of group 13. Part of their work included

the four In_2H_2 isomers of interest. To study the isomerization reactions and kinetic stability of the In_2H_2 isomers, Moc and Wierzejewska[151] in 2004 employed MP2 to obtain equilibrium structures and harmonic vibrational frequencies of the four isomers, subsequently using CCSD(T) for energetic studies.[151]

In the present research, we have used high level *ab initio* methods to determine minima on the potential energy surface of In_2H_2. We have used such minima to determine enthalpies of formation at 0 K and also provide vibrational frequencies to address experimental controversy and to aid future spectroscopic research.

5.3 Computational Methods

Equilibrium geometries and fundamental vibrational frequencies were determined using the CFOUR2.0 software.[77,78] Specifically, equilibrium geometries of each isomer were optimized using coupled cluster theory with single, double, and perturbative triple excitations [CCSD(T)] and the aug-cc-pwCVTZ-PP basis set.[152–157] Small-core pseudopotentials (PPs), or effective core potentials (ECPs), were used to reduce the number of explicitly treated electrons on the indium atom by describing 28 core electrons, [Ar]$3d^{10}$. Harmonic vibrational frequencies were obtained through finite differences of analytic gradients at the same level of theory in order to confirm that stationary points represented energy minima. Anharmonic vibrational frequencies and intensites were then determined using VPT2 for all minima at the CCSD(T)/aug-cc-pwCVTZ-PP level of theory with the CFOUR module, GUINEA, which performs VPT2 and VPT4 computations via numerical sum-over-states.[77,78,158] Anharmonic resonances were treated with the VPT2+K polyad approach, also available in GUINEA.[159,160]

Electronic energies at equilibrium geometries were determined using the Focal Point Analysis (FPA) of Allen and coworkers[161–164] Basis sets up to quintuple-zeta (In: aug-cc-pwCVXZ-PP; H: aug-cc-pVXZ, X=D,T,Q,5) were used for Restricted

Hartree–Fock energies, and basis sets up to quadruple-zeta were used for the MP2, CCSD, and CCSD(T) methods.[152–157] These energies were then extrapolated to the complete basis set limit (CBS) using a three-point fitting equation for Hartree–Fock energies

$$E_{HF} = A + Be^{-CX} \tag{5.1}$$

and a two-point fitting equation for correlation energies.

$$E_{corr} = A + BX^{-3} \tag{5.2}$$

Additive corrections were appended to the CCSD(T)/CBS energies to correct for effects not included in the computations. Obtained from our anharmonic vibrational frequencies, the zero-point vibrational energies (aZPVE) were added to account for the vibrational energy of the ground state for each isomer and determine the relative enthalpies of formation at zero kelvin ($\Delta_f H^{0K}$). Higher-order correlation effects were considered by appending the CCSDT(Q) correction to the CCSD(T)/CBS energy. The CCSDT(Q) corrections were computed with aug-cc-pwCVDZ-PP basis sets in the CFOUR2.0 software package and are represented as a single higher order correlation correction ($\delta_{T(Q)}$). The final energy for each species, relative to 2 In and H_2, is given as a sum of the electronic energy with the above energy corrections.

$$\Delta E = \Delta E_{FPA} + \delta_{aZPVE} + \delta_{T(Q)} \tag{5.3}$$

These methods were benchmarked by applying them to the InH dimer and comparing to the results compiled by Herzberg.[165] The bond distance only differed by 0.0015 Å ($r_{e,Exp}$ = 1.8376; $r_{e,Theory}$ = 1.8361). Our calculated fundamental frequency only differed from the experimental value by 10 cm^{-1} ($\nu_{e,Exp}$ = 1425 cm^{-1}; $\nu_{e,Theory}$ = 1415 cm^{-1}) which is remarkable considering our use of an ECP.

5.4 Results and Discussion

5.4.1 Geometries

Four minima of In_2H_2 — dibridged, monobridged, vinylidene-like, and *trans* — were optimized. The relevant internal coordinates of these equilibrium structures are shown in Figure 5.2. As expected, due to the larger atomic radii, each of the In–In bonds are longer than the Ga–Ga bonds predicted in the theoretical study of Palagyi *et al.*[140]

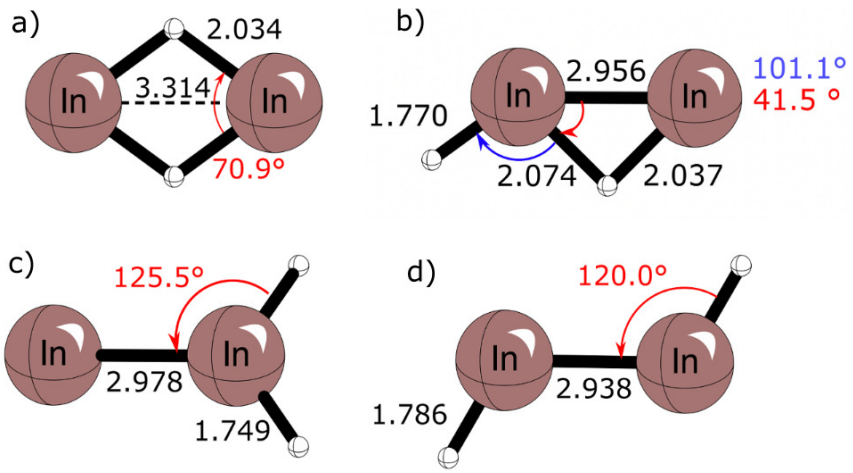

Figure 5.2: (a) Planar dibridged, (b) monobridged, (c) vinylidene-like, and (d) *trans* isomers with bond lengths in angstroms and bond angles in degrees, from CCSD(T)/aug-cc-pwCVTZ-PP.

No other structures have been suggested in previous literature, but additional isomers were investigated by rotating the In−In bond of the *trans* isomer. The *trans* orientation is an overall minimum and the *cis* orientation is an overall maximum (Figure 5.3). However, attempting to optimize the *cis* isomer as a transition state results in the structure disassociating into two InH molecules.

5.4.2 Enthalpies of Formation

The FPA results for each isomer are shown in Tables 5.1 - 5.4, and each shows good convergence to the CBS limit. All FPA tables are followed by corrections,

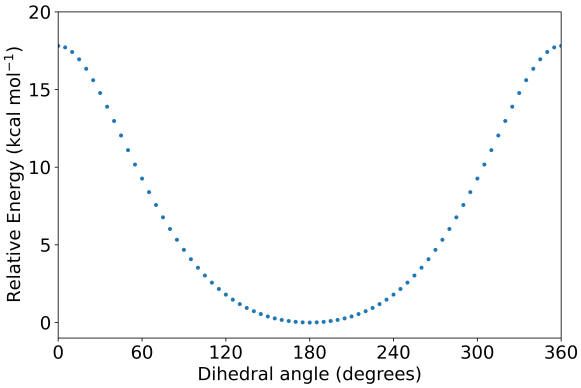

Figure 5.3: The potential energy surface of rotation around the In–In bond of the *trans* isomer. Energies are presented relative to the *trans* minimum (kcal mol^{-1}) and are calculated at the CCSD(T)/aug-cc-pwCVTZ-PP level of theory with a small core ECP.

including the higher-order effects and zero-point vibrational energies, as previously mentioned. Enthalpies of formation were calculated relative to two indium atoms and one H_2 molecule which have been treated with the same methods as our isomers where appropriate. This reference was chosen to reflect the experimental methods employed by Downs and coworkers[146] and Wang and Andrews[148] which used pure indium and hydrogen gas.

The absolute zero relative enthalpies of the isomers are shown in Figure 5.4. The dibridged structure has the lowest enthalpy, followed by the monobridged and vinylidene-like isomers, respectively. The *trans* isomer is the highest in enthalpy. The relative enthalpy difference from dibridged to monobridged is 10.8 kcal mol^{-1}. The most (dibridged) and least (*trans*) energetically favorable differ by 16.6 kcal mol^{-1}.

This relative ordering is different than Al_2H_2 and Ga_2H_2, which both have a relative ordering in increasing energy of dibridged, vinylidene-like, monobridged, and *trans*.[140,166] Though the relative ordering of the vinylidene-like and monobridged isomers are the opposite for In_2H_2 compared to Al_2H_2 or Ga_2H_2, their roughly similar energies may be noticed in Figure 5.4, and the theoretical difference is 2.8 kcal mol^{-1}. As we move from Al to Ga to In, the atomic radii increase. We suggest that the In–In

Table 5.1: Incremental focal point analysis with calculated and extrapolated (denoted by brackets) enthalpies of formation, in kcal mol^{-1}, for the planar dibridged isomer relative to 2 In + H_2. Basis set labels of the form XZ denote aug-cc-pwCVXZ-PP. Effects of anharmonic ZPVE and higher order δT(Q), both in kcal mol^{-1}, are given on the last line.

Basis Set	ΔE_e RHF	δ MP2	δ CCSD	δ CCSD(T)	ΔE_e NET
DZ	−19.75	−22.20	+0.65	−2.91	−44.20
TZ	−18.39	−25.96	+1.67	−3.29	−45.97
QZ	−18.43	−26.19	+1.98	−3.44	−46.08
5Z	−18.41	[−26.27]	[+2.09]	[−3.49]	[−46.09]
CBS	[−18.40]	[−26.36]	[+2.20]	[−3.54]	[−46.10]
$\Delta E = -46.10 - 0.09 + 0.16 = -46.03$ kcal mol^{-1}					

Table 5.2: Incremental focal point analysis with calculated and extrapolated (denoted by brackets) enthalpies of formation, in kcal mol^{-1}, for the monobridged isomer relative to 2 In + H_2. Basis set labels of the form XZ denote aug-cc-pwCVXZ-PP. Corrections for anharmonic ZPVE and higher order δT(Q), both in kcal mol^{-1}, are given on the last line.

Basis Set	ΔE_e RHF	δ MP2	δ CCSD	δ CCSD(T)	ΔE_e NET
DZ	−7.89	−21.42	+0.83	−3.28	−31.75
TZ	−6.86	−25.32	+1.60	−3.68	−34.26
QZ	−6.89	−25.81	+1.90	−3.87	−34.66
5Z	−6.87	[−25.98]	[+2.01]	[−3.93]	[−34.79]
CBS	[−6.87]	[−26.17]	[+2.12]	[−4.00]	[−34.92]
$\Delta E = -34.92 - 0.43 + 0.09 = -35.26$ kcal mol^{-1}					

Table 5.3: Incremental focal point analysis with calculated and extrapolated (denoted by brackets) enthalpies of formation, in kcal mol^{-1}, for the vinylidene-like isomer relative to 2 In + H_2. Basis set labels of the form XZ denote aug-cc-pwCVXZ-PP. Corrections for anharmonic ZPVE and higher order δT(Q), both in kcal mol^{-1}, are given on the last line.

Basis Set	ΔE_e RHF	δ MP2	δ CCSD	δ CCSD(T)	ΔE_e NET
DZ	−12.21	−14.40	−0.51	−2.34	−29.46
TZ	−10.91	−18.03	−0.59	−2.50	−32.03
QZ	−10.90	−18.60	−0.42	−2.64	−32.57
5Z	−10.89	[−18.81]	[−0.36]	[−2.70]	[−32.75]
CBS	[−10.88]	[−19.02]	[−0.29]	[−2.75]	[−32.94]
$\Delta E = -32.94 + 0.30 + 0.22 = -32.42$ kcal mol^{-1}					

Table 5.4: Incremental focal point analysis with calculated and extrapolated (denoted by brackets) enthalpies of formation, in kcal mol^{-1}, for the *trans* isomer relative to 2 In + H_2. Basis set labels of the form XZ denote aug-cc-pwCVXZ-PP. *Ab initio* corrections for anharmonic ZPVE and higher order δT(Q), both in kcal mol^{-1}, are given on the last line.

Basis Set	ΔE_e RHF	δ MP2	δ CCSD	δ CCSD(T)	ΔE_e NET
DZ	−2.77	−19.21	+0.27	−3.29	−25.00
TZ	−1.59	−22.57	+0.86	−3.62	−26.92
QZ	−1.61	−23.02	+1.13	−3.80	−27.30
5Z	−1.59	[−23.18]	[+1.22]	[−3.86]	[−27.41]
CBS	[−1.58]	[−23.35]	[+1.33]	[−3.93]	[−27.54]
$\Delta E = -27.54 - 0.68 - 1.20 = -29.42$ kcal mol^{-1}					

bond in the vinylidene-like isomer is weaker than the corresponding metal–metal bond in the gallium and aluminum analogues, and the hydrogen bridge in the monobridged HIn(μ-H)In provides necessary stability to make the monobridged isomer lower in energy than the vinylidene-like isomer. This can be seen from an orbital analysis of the monobridged isomer. The molecular orbital that corresponds the most to the 1s orbital of the hydrogen bridge is lower in energy than that of the terminal hydrogen and shows bonding character by mixing with the terminal hydrogen 1s orbital and similar s-orbitals of the indium atoms.

As previously mentioned, the relative energies of the vinylidene-like and *trans* In_2H_2 isomers have been a point of interest in experimental studies. Our results are broadly consistent with existing studies in the sense that the vinylidene-like isomer lies lower in energy than the *trans* isomer.[146,148,150,151] However, the more rigorous level of theory applied in this paper suggests that their energies differ by only 3 kcal mol^{-1} rather than 7 kcal mol^{-1} as previously determined by Downs and coworkers.[146]

5.4.3 Fundamental Vibrational Frequencies

In the course of computing the anharmonic frequencies, several Fermi resonances were recognized.[167] One Fermi resonance was identified in the vinylidene-like isomers, and

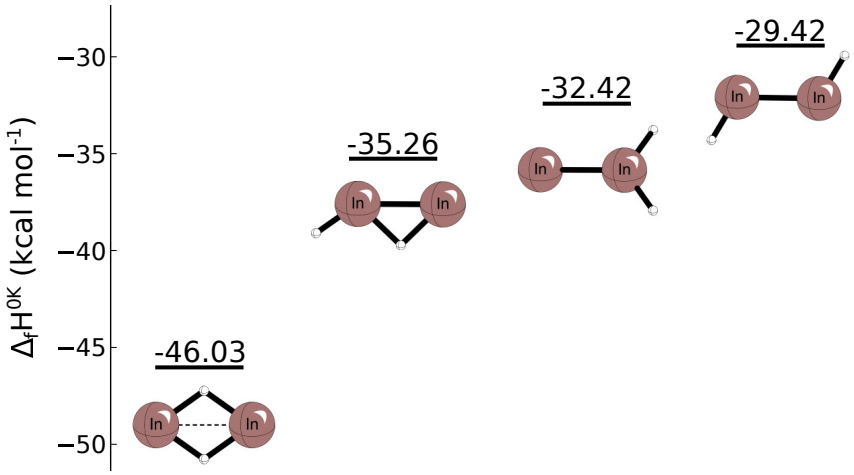

Figure 5.4: Enthalpies of formation at 0 K for the four isomers of In_2H_2 – dibridged, monobridged, vinylidene-like, and *trans* – relative to 2In and H_2. Enthalpies of formation were determined at the CCSD(T)/CBS level of theory and include anharmonic zero-point vibrational energies and δT(Q) effects.

two Fermi resonances were identified in the monobridged isomers (except for the perdeuterated case). Consequently, one of the fundamentals of each vinylidene-like isotopologue was treated in a Fermi dyad. The two Fermi resonances in the monobridged isomers share a normal coordinate and may be described as connected.[160] One fundamental is treated as a Fermi dyad, and another is treated in a triad. The relationship between the two Fermi resonances in the monobridged isomers is identical to that of the resonances of ethylene, which has been discussed by Martin *et al.*[167] All multiple-excited states for which these resonances manifest are also treated in polyads, allowing for reasonable anharmonic frequencies and intensities to be obtained.

Tables 5.5, 5.6, and 5.7 present our raw theoretical predictions. In Table 5.8 we report theoretical vibrational frequencies and infrared intensities for the In_2H_2 structures with comparison to experiment.[146,148] A very large VPT2 intensity associated with a small harmonic intensity would usually reflect strong, untreated resonance effects. In this study, the large VPT2 intensities that you see are also large at the harmonic level. In fact, we find that the anharmonic effects nearly always lower the intensity of the strong transitions in In_2H_2. The large harmonic intensity can

be rationalized by an analogy to proton-bound dimers, for which the antisymmetric proton stretching (sometimes called shuttling) fundamental is always very intense in experimental spectra.[168,169] Shuttling is a "soft" vibrational mode and the associated harmonic intensity is also very high. The shuttling motion involves motion of the positively- and negatively-charged parts of the molecular ion against one-another, inducing large changes in the dipole moment. For dibridged In_2H_2, the strongest fundamental (b_{3u}) is similar in character to the proton-shuttle. Although this is a neutral system, the hydrogen and indium atoms carry substantial partial charges. Based on the Mulliken populations, the hydrogens are each $-1/3$ charged, and the indiums are each $+1/3$ charged.

We begin with comparisons to the argon matrix isolation experiments of Himmel, Manceron, Downs, and Pullumbi.[146] Their most intense infrared feature was found at 955 cm^{-1}. Our most intense theoretical fundamental is predicted at 988 cm^{-1} for the dibridged structure. Its theoretical IR intensity of 2148 km mol^{-1} is about an order of magnitude greater than the next strongest transition, in accord with the experimental relative intensities. Further, the experimental feature at 955 cm^{-1} does not agree well with any of the predicted fundamentals of the vinylidene-like, *trans*, or monobridged isomers of In_2H_2.

Wang and Andrews[148] observed similarly intense features at 983 cm^{-1} (in neon) and 980 cm^{-1} (in solid hydrogen), in good agreement with our theoretical prediction of 988 cm^{-1}. The theoretical value, computed for a single molecule in the gas phase, is greater than the neon matrix value, which is greater than the hydrogen matrix value, which is greater than the argon matrix value. This is the typical pattern of matrix shifts, with argon usually giving the greatest red-shifts relative to gas phase or high-level theoretical predictions. In addition to relative intensity arguments and the close agreement between theoretical and neon matrix values, the fact that these transitions align with the expected matrix shifts provides additional support for assignment to

Table 5.5: Fundamental vibrational frequencies (cm^{-1}) and intensities (km mol^{-1}) for isomers of In_2H_2 with their corresponding irreducible representations. For resonant fundamentals, the transition with the greatest character of each fundamental is given in the table with other transitions as footnotes.

In(μ-H)$_2$In D_{2h}	In(μ-H)InH C_s	InInH$_2$ C_{2v}	HInInH C_{2h}
1089 (0, a_g)	1532 (796, a')	1616 (391, b_2)	1509 (1272, b_u)
988 (2148, b_{3u})	983[a] (180, a')	1610 (601, a_1)	1492 (0, a_g)
824 (0, b_{1g})	699 (465, a')	655[c] (268, a_1)	396 (0, a_g)
810 (276, b_{2u})	337[b] (2, a')	314 (77, b_1)	157 (36, a_u)
258 (2, b_{1u})	197 (12, a'')	157 (30, b_2)	121 (28, b_u)
128 (0, a_g)	109 (5, a')	133 (8, a_1)	92 (0, a_g)

[a]Member of Fermi triad: other transitions at (1060, 1112) cm^{-1} with (147, 58) km mol^{-1}

[b]Member of Fermi dyad: other transition at 414 cm^{-1} with 3 km mol^{-1}

[c]Member of Fermi dyad: other transition at 608 cm^{-1} with 105 km mol^{-1}

Table 5.6: Fundamental vibrational frequencies (cm^{-1}) and intensities (km mol^{-1}) for isomers of In_2D_2 with their corresponding irreducible representations. For resonant fundamentals, the transition with the greatest character of each fundamental is given in the table with other transitions as footnotes.

In(μ-D)$_2$In D_{2h}	In(μ-D)InD C_s	InInD$_2$ C_{2v}	DInInD C_{2h}
781 (0, a_g)	1110 (423, a')	1162 (207, b_2)	1087 (640, b_u)
718 (1160, b_{3u})	761 (195, a')	1156 (309, a_1)	1073 (0, a_g)
598 (0, b_{1g})	575 (281, a')	466[a] (115, a_1)	285 (0, a_g)
582 (141, b_{2u})	280 (2, a')	226 (38, b_1)	104 (18, a_u)
182 (2, b_{1u})	171 (6, a'')	131 (9, a_1)	92 (15, b_u)
131 (0, a_g)	111 (7, a')	115 (14, b_2)	92 (0, a_g)

[a]Member of Fermi dyad: other transition at 439 cm^{-1} with 74 km mol^{-1}

Table 5.7: Fundamental vibrational frequencies (cm^{-1}) and intensities (km mol^{-1}) for isomers of In_2HD with their corresponding irreducible representations. For resonant fundamentals, the transition with the greatest character of each fundamental is given in the table with other transitions as footnotes.

In(μ-H)(μ-D)In C_{2v}	In(μ-D)InH C_s	In(μ-H)InD C_s	InInHD C_s	HInInD C_s
998 (69, a_1)	1531 (775, a')	1104 (447, a')	1611 (507, a')	1504 (643, a')
924 (1366, b_2)	736[a] (158, a')	1039[c] (191, a')	1160 (248, a')	1083 (309, a')
641 (225, b_2)	515 (247, a')	695 (453, a')	567[e] (209, a')	345 (3, a')
636 (142, a_1)	331[b] (2, a')	246[d] (6, a')	273 (58, a'')	139 (27, a'')
223 (2, b_1)	176 (15, a'')	162 (3, a'')	134 (17, a')	112 (19, a')
129 (0, a_1)	107 (6, a')	107 (5, a')	131 (10, a')	94 (1, a′)

[a]Member of Fermi triad: other transitions at (845, 884) cm^{-1} with (13, 16) km mol^{-1}
[b]Member of Fermi dyad: other transition at 371 cm^{-1} with 5 km mol^{-1}
[c]Member of Fermi triad: other transitions at (921, 1010) cm^{-1} with (52, 118) km mol^{-1}
[d]Member of Fermi dyad: other transition at 340 cm^{-1} with 2 km mol^{-1}
[e]Member of Fermi dyad: other transition at 531 cm^{-1} with 79 km mol^{-1}

Table 5.8: Theoretical and observed vibrational transitions (cm^{-1}) for two isomers of In_2H_2.

Dibridged In(μ-H)$_2$In			*trans* HInInH		
State	Theory	Expt.	State	Theory	Expt.
$\nu_1 + \nu_6$	2065	2021[c]	ν_5	1509	1537[a], (1530,1528)[b], 1518[c]
$\nu_2 + \nu_6$	1113	1079[c]		-	629[b]
ν_6	988	983[a], 980[b], 955[c]		-	-
ν_3	824	848[c]		-	-
ν_5	810	800[c]		-	-

[a]in neon, Ref. 148; [b]in hydrogen, Ref. 148; [c]in argon, Ref. 146

the b_{3u} fundamental of the dibridged isomer. This is also consistent with previous assignments.[146,148]

Downs and coworkers[146] in their Table 3, observed weaker features at 800, 848, 1079, and 2021 cm^{-1}. On the basis of these features' similar response to different forms of irradiation as the 955 cm^{-1} feature, these were also associated with dibridged In_2H_2. The agreement with our predicted transitions is acceptable. We emphasize that these four experimental features also do not coincide with any of our predicted fundamentals for the vinylidene-like, *trans*, or monobridged isomers. Differences between theory and the argon matrix values for these transitions are 10, -24, 34, and 44 cm^{-1}, respectively. Notable is the weak 848 cm^{-1} transition, which is blueshifted relative to the theoretical prediction. This corresponds to an infrared inactive b_{1g} symmetry fundamental, made active by isotopic substitution of one ^{115}In atom with the less abundant ^{113}In, lowering the point group symmetry to C_{2v}.[146] We did not compute frequencies specifically for this mixed indium isotopologue. When considering transitions of any symmetry, of up to three quanta, for the main isotopologue, the predicted 824 cm^{-1} b_{1g} fundamental is the only one reasonably close to the 848 cm^{-1} experimental value. Compared to the next nearest predicted transitions in either direction, the experimental transition is 48 cm^{-1} to the blue and 90 cm^{-1} to the red.

Downs and coworkers[146] assigned one feature (1518 cm^{-1}) to the *trans* HInInH isomer, as it had a markedly different response to irradiation and annealing compared to the dibridged transitions. This fits very well with our theoretical feature of highest IR intensity (1272 km mol^{-1}) at 1509 cm^{-1}. The predicted spectrum of the *trans* isomer is dominated by this single fundamental, the antisymmetric In–H stretch, the other infrared active fundamentals being about two orders of magnitude weaker. Based on the signal-to-noise ratio of the 1518 cm^{-1} band, the other fundamentals would not have been detectable in Downs and coworkers' experiment.[146]

Wang and Andrews[148] tentatively assigned hydrogen matrix features at 1530 and

1528 cm^{-1} to the vinylidene-like isomer $InInH_2$. They also detected these transitions in neon, where they appeared as a single feature at 1537 cm^{-1}. Our symmetric and antisymmetric In−H stretching frequencies are predicted at 1610 and 1616 cm^{-1}, respectively, significantly higher than the 1537 cm^{-1} neon matrix transition, to which they should agree most closely. On the basis of this nearly 80 cm^{-1} disagreement, we are skeptical of this assignment. Wang and Andrews also observed a transition at 629 cm^{-1}, in the hydrogen matrix experiments, which they determined to have the same carrier as the 1530 and 1528 cm^{-1} stretching transitions. We predict two transitions of the vinylidene-like isomer at 655 and 608 cm^{-1}, resulting from a strong Fermi Type I resonance between a bending fundamental and the overtone of a lower frequency bend. These have similar intensity, and bookend the 629 cm^{-1} feature, which appears in Wang and Andrews' Figure 7 as a doublet. Although the 629 cm^{-1} transition can be adequately explained, the disagreement in the stretches does not allow for a satisfying assignment of the secondary In_2H_2 isomer as vinylidene-like.

We propose the following explanation: the 629 cm^{-1} feature does not in fact have the same carrier as the stretching transitions at 1530 and 1528 cm^{-1}, which arise not from the vinylidene-like isomer but from the *trans* isomer. This is supported by the absence of a corresponding low frequency feature in the neon matrix experiments and the fact that the 629 cm^{-1} feature appears to be present immediately after deposition in the hydrogen matrix experiments, in contrast with the stretching features. (See Wang and Andrews Figure 7.)[148] Moreover, the trend in matrix shifts is reasonable, as the 1518 cm^{-1} stretching band of *trans* In_2H_2 in argon is lower than the 1528/1530 cm^{-1} doublet in hydrogen which is lower than the 1537 cm^{-1} band in neon. However, this implies a 28 cm^{-1} blueshift of the neon matrix transitions relative to theory, which is fairly unusual. It is also not clear how the doublet splitting of the hydrogen matrix transition arises; although, this could very well be due to site effects (i.e., inhomogeneity of the matrix environment).

Let us consider the possibility that the monobridged isomer is the identity of the secondary isomer(s) of In_2H_2 produced in these experiments. As noted above, the monobridged structure is predicted to lie energetically *below* the vinylidene-like and *trans* structures. Monobridged In_2H_2 is predicted to have a strong transition at 1532 cm^{-1}, one about half as strong at 699 cm^{-1} and three weaker transitions at 983, 1060, and 1112 cm^{-1}. Although the high-frequency stretching transition provides the best agreement out of the four isomers with the neon matrix 1537 cm^{-1} band, the strong predicted bending transition at 699 cm^{-1} agrees poorly with the 629 cm^{-1} transition in hydrogen and was not observed in neon. Thus, despite the issues with assignment to the *trans* isomer, the disagreement between the predicted transitions and the various matrix values is far lower than for either the vinylidene-like isomer (where its stretches disagree greatly) or the monobridged isomer (where the bending frequency disagrees greatly).

Downs and coworkers[146] reported infrared features for In_2D_2 in argon. For comparisons with experiment, see Table 5.9. For the dibridged structure, they observed the strongest (b_{3u}) transition at 693 cm^{-1}, in reasonable agreement with our prediction of 718 cm^{-1}. The next strongest transition was observed at 582 cm^{-1}, which agrees precisely with the theoretical value. A combination band was observed at 815 cm^{-1}, analogous to the 1079 cm^{-1} transition in dibridged In_2H_2. The corresponding prediction is 847 cm^{-1}. Similar to In_2H_2, a very weak transition was observed for In_2D_2 at 612 cm^{-1} and assigned to an a_g fundamental, allowed in mixed indium isotopologues. Our prediction for this transition is 598 cm^{-1}, 14 cm^{-1} to the red of experiment. Downs and coworkers again assigned one feature to the antisymmetric In–H stretch of the *trans* isomer, this time at 1081 cm^{-1}. This is in agreement with our prediction of 1087 cm^{-1}.

Wang and Andrews[148] observed the strongest transition of the dibridged In_2D_2 isomer at 710 cm^{-1} in hydrogen and 712 cm^{-1} in neon. As expected, these are

Table 5.9: Theoretical and observed vibrational transitions (cm^{-1}) for two isomers of In_2D_2.

Dibridged $In(\mu\text{-}D)_2In$			*trans* DInInD		
State	Theory	Expt.	State	Theory	Expt.
$\nu_2 + \nu_6$	847	815[c]	ν_5	1087	1105[a], (1103,1099)[b], 1081[c]
ν_6	718	712[a], 710[b], 693[c]		-	456[b]
ν_3	598	612[c]		-	-
ν_5	582	582[c]		-	-

[a]in neon, Ref. 148; [b]in hydrogen, Ref. 148; [c]in argon, Ref. 146

higher than the corresponding transition in argon and agree excellently with the 718 cm^{-1} prediction. They observed In–D stretching transitions at 1103 and 1099 cm^{-1} in hydrogen and at 1105 cm^{-1} in neon. As with In_2H_2, they also associated a bending transition at 456 cm^{-1} in hydrogen with the same carrier. They proposed that these were transitions of the vinylidene-like In_2D_2 isomer. However, these are better explained as the antisymmetric In–D stretch of the *trans* isomer, with the 456 cm^{-1} feature arising from some other indium hydride species or a contaminant. A strong bending transition at 575 cm^{-1} is predicted for the monobridged isomer but is not observed by Wang and Andrews, ruling it out as the identity of the secondary isomer. For the vinylidene-like isomer, its predicted In–D stretches are 50 cm^{-1} higher than the neon matrix transition, ruling it out.

Finally, in Table 5.10 we present comparisons between theory and experiment for monodeuterated diindium dihydride–specically for the dibridged $In(\mu\text{-}H)(\mu\text{-}D)In$ and *trans* HInInD isomers. In their experiments with HD in argon, Downs and coworkers observed a strong transition at 900 cm^{-1} and two weak transitions at 630 and 605 cm^{-1}.[146] The strong transition clearly corresponds to the strongest b_2 fundamental of the dibridged isomer, predicted at 924 cm^{-1}. The weaker transitions at 630 and 605 cm^{-1} are best assigned to the 641 cm^{-1} b_2 and 636 cm^{-1} a_1 fundamentals, respectively. Both have about one order of magnitude lower intensity than the 924 cm^{-1} transition.

Table 5.10: Theoretical and observed vibrational transitions (cm^{-1}) for two isomers of In_2HD.

Dibridged In(μ-H)(μ-D)In			*trans* HInInD		
State	Theory	Expt.	State	Theory	Expt.
ν_4	924	923[a], 918[b], 900[c]	ν_1	1504	1535[a], 1529[b]
ν_5	641	630[c]	ν_2	1083	1107[a], 1101[b]
ν_2	636	605[c]		-	-

[a]in neon, Ref. 148; [b]in hydrogen, Ref. 148; [c]in argon, Ref. 146

Wang and Andrews observed the strong dibridged transition at 918 cm^{-1} in hydrogen and 923 cm^{-1} in neon, which agree well with the *ab initio* prediction.[146]

Wang and Andrews observed In–H stretches at 1529 and 1535 cm^{-1} and In–D stretches at 1101 and 1107 cm^{-1} in hydrogen and neon, respectively.[146] These local-mode stretching fundamentals of the mixed HD isotopologue are shifted by only a few wavenumbers relative to the normal-mode antisymmetric stretching fundamentals of the pure isotopologues. The predicted stretching fundamentals are 1504 cm^{-1} and 1083 cm^{-1} for *trans* In_2HD. These are again somewhat red-shifted relative to the experimental values in the least perturbative matrix environment, neon. Wang and Andrews did not report a low frequency bending transition, as with In_2H_2 and In_2D_2.[148]

5.5 Conclusion

In this study, four isomers of In_2H_2 were characterized using high-level *ab initio* methods. Equilibrium geometries were optimized with CCSD(T)/aug-cc-pwCVTZ-PP using a small core pseudopotential. Energies were extrapolated to the CBS limit and included anharmonic zero-point vibrational energy and higher-order energy corrections up to CCSDT(Q). Finally, fundamental vibrational frequencies were obtained for all four isomers for spectroscopic comparisons.

Of the four isomers, the planar dibridged is the most favored at 0 K, followed by

the monobridged isomer at 10.8 kcal mol^{-1}. The vinylidene-like is the next lowest in energy (13.6 kcal mol^{-1}), and the *trans* isomer is last, lying at 16.6 kcal mol^{-1} compared to the dibridged structure. Our high-level calculations have confirmed the reported observations of the dibridged and *trans* structures of In_2H_2 by Downs and coworkers.[146] We argued that the features assigned to the stretches of the vinylidene-like isomer by Wang and Andrews correspond instead to the *trans* isomer. The monobridged isomer, lying energetically higher than only the dibridged structure, remains to be observed in the laboratory. A high-level *ab initio* study of the In_2H_2 isomers on the low-lying triplet surface would be a valuable supplement to this study, in addition to singlet diindane, In_2H_6, to which Wang and Andrews assigned numerous spectroscopic features.[145,148]

Chapter 6

Conclusion

Many areas of chemistry already benefit from quantum chemistry methods and use theoretical results to further support their experimental evidence. The examples given here demonstrate how these methods can be used to investigate the properties of molecules, even before experimental data is gathered. Such data can be used to inform and direct future experimental discovery, allowing experimentalists to focus their time and effort on the avenues of discovery that have the highest chances of success.

The addition pathways of atmospheric methylamine to stabilized Criegee intermediates were found have rate constants at least an order of magnitude larger than the analogous ammonia, water, or water dimer addition. The orientation of the methylamine was also found to affect the kinetics of the reaction, with the axial addition pathway giving rate constants at least three times as large as the equatorial pathways in all cases except for the *syn*-methylated Criegee intermediates which saw comparable rate constants for each pathway. While the results were as expected for the second order rate constants, treating the reactions as pseudo-first order reactions showed that the methylamine reaction pathways would still be unlikely to significantly contribute to the consumption of Criegee intermediates. Even in this case, these results can still be used for large-scale kinetic modeling, where hundreds of concurrent reactions are all competing with each other, or for atmospheric studies in areas with artificially inflated levels of methylamine.

Pentazole was studied for its potential as a green high-energy-density material, but it was found to have an energy barrier of 18.8 kcal mol^{-1} which is much lower than the desired barrier of 30 kcal mol^{-1}. Under the restraints of canonical transition

state theory, an energy barrier of this size is only attainable at temperatures near or below 180 K. Our results matched those found by some previous studies, but this was only with the inclusion of perturbative quadruple excitations. These results give confidence that those composite methods would give reliable results for pentazole derivatives, molecules which would be much too large to study with the same level of theory. HEDMs are inherently dangerous molecules, but theoretical studies like these mitigate some of the danger through their thermochemical predictions.

Fundamental frequencies for four In_2H_2 isomers were calculated via the VPT2+K method and compared to previous experimental assignments. Here, we suggested that the 629 cm^{-1} peak which was attributed to the vinylidene-like isomer by Wang and Andrews[148] should instead be attributed to the trans structure. Aside from this, all other feature assignments matched well with our *ab initio* predictions. Our energy calculations also suggested that the energy difference between the vinylidene-like and trans isomers is only about half the magnitude of what was previously reported by Downs and coworkers[146]. These discrepancies highlight the need for high-level *ab initio* calculations to verify the results of less rigorous methods. Any future gas phase experimental studies will be able to use this data as a reference for their feature assignments.

Experimental studies have much to gain by utilizing the tools of theoretical quantum chemistry. Not only can they save time and effort by screening potential reactions in a more cost-efficient manner, they can also serve as further verification of experimental data. Quantum chemistry tools can reveal properties of reactions which are difficult to observer through conventional experimental means. Theoretical *ab initio* quantum chemistry clearly is a useful tool and experimentalists gain many benefits from it, but experiment is also necessary for theoretical chemistry as well. Without experimental verification, many theoretical results may only exist as suggestions and possibilities rather than fact.

References

[1] Ozaki, Y.; Beć, K. B.; Morisawa, Y.; Yamamoto, S.; Tanabe, I.; Huck, C. W.; Hofer, T. S. Advances, challenges and perspectives of quantum chemical approaches in molecular spectroscopy of the condensed phase. *Chem. Soc. Rev.* **2021**, *50*, 10917–10954.

[2] Puzzarini, C.; Stanton, J. F.; Gauss, J. Quantum-chemical calculation of spectroscopic parameters for rotational spectroscopy. *Int. Rev. Phys. Chem.* **2010**, *29*, 273–367.

[3] Bühl, M.; van Mourik, T. NMR spectroscopy: quantum-chemical calculations. *Wiley Interdiscip. Rev. Comput. Mol. Sci.* **2011**, *1*, 634–647.

[4] Fortenberry, R. C. Quantum astrochemical spectroscopy. *Int. J. Quantum Chem.* **2017**, *117*, 81–91.

[5] Lahm, M. E.; Kitzmiller, N. L.; Mull, H. F.; Allen, W. D.; Schaefer, H. F. I. Concordant Mode Approach for Molecular Vibrations. *J. Am. Chem. Soc.* **2022**, *144*, 23271–23274.

[6] Shi, S. Advances in modeling hydrocarbon cracking kinetic predictions by quantum chemical theory: A review. *Int. J. Energy Res.* **2018**, *42*, 3164–3181.

[7] Zádor, J.; Taatjes, C. A.; Fernandes, R. X. Kinetics of elementary reactions in low-temperature autoignition chemistry. *Prog. Energy Comb. Sci.* **2011**, *37*, 371–421.

[8] Gao, J.; Truhlar, D. G. QUANTUM MECHANICAL METHODS FOR ENZYME KINETICS. *Annu. Rev. Phys. Chem.* **2002**, *53*, 467–505.

[9] Foster, J. M.; Boyes, S. F. Quantum Variational Calculations for a Range of CH_2 Configurations. *Rev. Mod. Phys.* **1960**, *32*, 305–307.

[10] Bender, C. F.; Schaefer, H. F. New Theoretical Evidence for the Nonlinearity of the Triplet Ground State of Methylene. *J. Am. Chem. Soc.* **1970**, *92*, 4984–4985.

[11] Rothenberg, S.; III, H. F. S. Self-consistent-field wave functions, energies, multipole moments, diamagnetic susceptibility and shielding tensors, and electric field gradient tensors for nitrogen dioxide and ozone. *Mol. Phys.* **1971**, *21*, 317–327.

[12] Schwenzer, G. M.; O'Neil, S. V.; Schaefer, H. F.; Baskin, C. P.; Bender, C. F. Geometries of the excited electronic states of HCN. *J. Chem. Phys.* **1974**, *60*, 2787–2793.

[13] Schaefer, H. F. The Silicon-Carbon Double Bond: A Healthy Rivalry between Theory and Experiment. *Acc. Chem. Res.* **1982**, *15*, 283–290.

[14] Szabo, A.; Ostlund, N. S. *Modern Quantum Chemistry*; Dover Publications, Inc., 1996.

[15] *Molecular Electronic-Structure Theory*; John Wiley & Sons, Ltd., 2000.

[16] McQuarrie, D. A. *Statistical Mechanics*; University Science Books, 2000.

[17] Raghavachari, K.; Trucks, G. W.; Pople, J. A.; Head-Gordon, M. A fifth-order perturbation comparison of electron correlation theories. *Chem. Phys. Lett.* **1989**, *157*, 479–483.

[18] Franke, P. R.; Stanton, J. F.; Douberly, G. E. How to VPT2: Accurate and Intuitive Simulations of CH Stretching Infrared Spectra Using VPT2+K with

Large Effective Hamiltonian Resonance Treatments. *The Journal of Physical Chemistry A* **2021**, *125*, 1301–1324.

[19] Criegee, V. R.; Wenner, G. Die Ozonisierung des 9,10-Oktalins. *Liebigs Ann. Chem.* **1949**, *564*, 9–15.

[20] Assaf, E.; Sheps, L.; Whalley, L.; Heard, D.; Tomas, A.; Schoemaecker, C.; Fittschen, C. The Reaction between CH_3O_2 and OH Radicals: Product Yields and Atmospheric Implications. *Environ. Sci. Technol.* **2017**, *51*, 2170–2177.

[21] Shallcross, D. E.; Leather, K. E.; Bacak, A.; Xiao, P.; Lee, E. P.; Ng, M.; Mok, D. K.; Dyke, J. M.; Hossaini, R.; Chipperfield, M. P.; Khan, M. A. H.; Percival, C. J. Reaction between CH_3O_2 and BrO Radicals: A New Source of Upper Troposphere Lower Stratosphere Hdroxyl Radicals. *J. Phys. Chem.* **2015**, *119*, 4618–4632.

[22] Jungkamp, T.; Kukui, A.; Schindler, R. Determination of Rate Constants and Product Branching Ratios for the Reactions of CH_3O_2 and CH_3O with Cl Atoms at Room Temperature. *Ber. Bunsenges. Phys. Chem.* **1995**, *99*, 1057–1066.

[23] Sarnela, N. et al. Measurement-model comparison of stabilized Criegee intermediate and highly oxygenated molecule production in the CLOUD chamber. *Atmos. Chem. Phys.* **2018**, *18*, 2363–2380.

[24] Welz, O.; Savee, J. D.; Osborn, D. L.; Vasu, S. S.; Percival, C. J.; Shallcross, D. E.; Taatjes, C. A. Direct Kinetic Measurements of Criegee Intermediate (CH_2OO) Formed by Reaction of CH_2I with O_2. *Science* **2012**, *335*, 204–207.

[25] Smith, M. C.; Chao, W.; Takahashi, K.; Boering, K. A.; Lin, J. J.-M. Unimolecular Decomposition Rate of the Criegee Intermediate $(CH_3)_2COO$ Measured Directly with UV Absorption Spectroscopy. *J. Phys. Chem.* **2016**, *120*, 4789–4798.

[26] Ouyang, B.; McLeod, M. W.; Jones, R. L.; Bloss, W. J. NO_3 radical production from the reactino between the Criegee intermediate CH_2OO and NO_2. *Phys. Chem. Chem. Phys.* **2013**, *15*, 17070–17075.

[27] Hasson, A. S.; Chung, M. Y.; Kuwata, K. T.; Converse, A. D.; Krohn, D.; Paulson, S. E. Reaction of Criegee Intermediates with Water Vapor - An Additional Source of OH Radicals in Alkene Ozonolysis? *J. Phys. Chem.* **2003**, *107*, 6176–6182.

[28] Novelli, A.; Vereecken, L.; Lelieveld, J.; Harder, H. Direct observation of OH formation from stabilised Criegee intermediates. *Phys. Chem. Chem. Phys.* **2014**, *16*, 19941–19951.

[29] Liu, Y.; Yin, C.; Smith, M. C.; Liu, S.; Chen, M.; Zhou, X.; Xiao, C.; Dai, D.; Lin, J. J.-M.; Takahashi, K.; Dong, W.; Yang, X. Kinetics of the reactino of the simplest Criegee intermediate with ammonia: a combination of experiment and theory. *Phys. Chem. Chem. Phys.* **2018**, *20*, 29669–29676.

[30] Chhantyal-Pun, R. et al. Experimental and computational studies of Criegee intermediate reactions with NH_3 and CH_3NH_2. *Phys. Chem. Chem. Phys.* **2019**, *21*, 14042–14052.

[31] Taatjes, C. A.; Welz, O.; Eskola, A. J.; Savee, J. D.; Scheer, A. M.; Shallcross, D. E.; Rotavera, B.; Lee, E. P.; Dyke, J. M.; Mok, D. K.; Osborn, D. L.; Percival, C. J. Direct Measurements of Conformer-Dependent Reactivity of the Criegee Intermediate CH_3CHOO. *Science* **2013**, *340*, 177–180.

[32] Nakajima, M.; Endo, Y. Determination of the molecular structure of the simplest Criegee intermediate CH_2OO. *J. Chem. Phys.* **2013**, *139*, 101103.

[33] Khan, M.; Percial, C.; Caravan, R.; Taatjes, C.; Shallcross, D. Criegee interme-

diates and their impacts on the troposphere. *Environ. Sci.: Processes Impacts* **2018**, *20*, 437–453.

[34] Elshorbany, Y.; Kurtenbach, R.; Wiesen, P.; Lissi, E.; Rubio, M.; Villena, G.; Gramsh, E.; Rickard, A.; Pilling, M.; Kleffman, J. Oxidation capacity of the city air of Santiago, Chile. *Atmos. Chem. Phys.* **2009**, *9*, 2257–2273.

[35] Harrison, R. et al. Measurement and modelling of air pollution and atmospheric chemistry in the U.K. West Midlands conurbation: Overview of the PUMA Consortium project. *Sci. Total Environ.* **2006**, *360*, 5–25.

[36] Horie, O.; Moortgat, G. Decomposition pathways of the excited Criegee intermediates in the ozonolysis of simple alkenes. *Atmos. Environ.* **1991**, *25*, 1881–1896.

[37] Meidan, D. M.; Holloway, J. S.; Edwards, P. M.; Dubé, W.; Middlebrook, A. M.; Liao, J.; Welti, A.; Graus, M.; Warneke, C.; Ryerson, T. B.; Pollack, I. B.; Brown, S. S.; Rudich, Y. Role of Criegee Intermediates in Secondary Sulfate Aerosol Formation in Nocturnal Power Plant Plumes in theh Southeast US. *ACS Earth Space Chem.* **2019**, *3*, 748–759.

[38] Kalinowski, J.; Räsänen, M.; Heinonen, P.; Kilpeläinen, I.; Gerber, R. B. Isomerization and Decomposition of a Criegee Intermediate in the Ozonolysis of Alkenes: Dynamics Using a Multireference Potential. *Angew. Chem. Int. Ed.* **2014**, *53*, 265–268.

[39] Nguyen, T. L.; Lee, H.; Matthews, D. A.; McCarthy, M. C. Stabilization of the Simplest Criegee Intermediate from the Reaction between Ozone and Ethylene: A High-Level Quantum Chemical and Kinetic Analysis of Ozonolysis. *J. Phys. Chem.* **2015**, *119*, 5524–5533.

[40] Ryzhkov, A. B.; Ariya, P. A. The importance of water clusters $(H_2O)_n$ (n=2,...,4) in the reaction of Criegee intermediate with water in the atmosphere. *Chem. Phys. Lett.* **2006**, *419*, 479–485.

[41] Long, B.; Bao, J. L.; Truhlar, D. G. Atmospheric Chemistry of Criegee Intermediates: Unimolecular Reactions and Reactions with Water. *J. Am. Chem. Soc.* **2016**, *138*, 14409–14422.

[42] Sheps, L.; Rotavera, B.; Eskola, A. J.; Osborn, D. L.; Taatjes, C. A.; Au, K.; Shallcross, D. E.; Khan, M. A. H.; Percival, C. J. The reaction of Criegee intermediates CH2OO with water dimer: Primary products and atmospheric impact. *Phys. Chem. Chem. Phys.* **2017**, *19*, 21970–21979.

[43] Lin, L. C.; Chang, H. T.; Chang, C. H.; Chao, W.; Smith, M. C.; Chang, C. H.; Jr-Min Lin, J.; Takahashi, K. Competition between H2O and (H2O)2 reactions with CH2OO/CH3CHOO. *Physical Chemistry Chemical Physics* **2016**, *18*, 4557–4568.

[44] Lin, L. C.; Chao, W.; Chang, C. H.; Takahashi, K.; Lin, J. J. M. Temperature dependence of the reaction of: Anti -CH3CHOO with water vapor. *Physical Chemistry Chemical Physics* **2016**, *18*, 28189–28197.

[45] Xu, K.; Wang, W.; Wei, W.; Feng, W.; Sun, Q.; li, P. Insights into the Reaction Mechanizm of Criegee Intermediate CH_2OO with Methane and Implications for the Formation of Methanol. *J. Phys. Chem.* **2017**, *121*, 7236–7245.

[46] Aroeira, G. J.; Abbot, A. S.; Elliot, S. N.; Turney, J. M.; Schaefer, H. F. The addition of methanol to Criegee intermediates. *Phys. Chem. Chem. Phys.* **2019**, *21*, 17760–17771.

[47] Li, J.; Ying, Q.; Yi, B.; Yang, P. Role of stabilized Criegee Intermediates in

the formation of atmospheric sulfate in eastern United States. *Atmos. Environ.* **2013**, *79*, 442–447.

[48] Vereecken, L.; Harder, H.; Novelli, A. The reaction of Criegee intermediates with NO, RO_2, and SO_2, and their fate in the atmosphere. *Phys. Chem. Chem. Phys.* **2012**, *14*, 14682–14695.

[49] Percival, C. J. et al. Regional and global impacts of Criegee intermediates on atmospheric sulphuric acid concentrations and first steps of aerosol formation. *Faraday Discuss.* **2013**, *165*, 45–73.

[50] Misiewicz, J. P.; Elliott, S. N.; Moore, K. B.; Schaefer, H. F. Re-examining ammonia addition to the Criegee intermediate: converging to chemical accuracy. *Phys. Chem. Chem. Phys.* **2018**, *20*, 7479–7491.

[51] Jørgensen, S.; Gross, A. Theoretical Investigation of the Reaction between Carbonyl Oxides and Ammonia. *J. Phys. Chem.* **2009**, *113*, 10284–10290.

[52] Kumar, M.; Francisco, J. S. Elucidating the molecular mechanisms of Criegee-amine chemistry in the gas phase and aqueous surface environments. *Chem. Sci.* **2019**, *10*, 743–751.

[53] Raes, F.; Dingenen, R. V. Simulations of condensation and cloud condensation nuclei from biogenic SO_2 in the remote marine boundary layer. *J. Geophys. Res. - Atmos* **1992**, *97*, 12901–12912.

[54] Charlson, R. J.; Covert, D. S.; Larson, T. V.; Waggoner, A. P. Chemical properties of tropospheric sulfur aerosols. *Atmos. Environ.* **1978**, *12*, 39–53.

[55] Ruehl, C. R.; Davies, J. F.; Wilson, K. R. An interfacial mechanism for cloud droplet formation on organic aerosols. *Science* **2016**, *351*, 1447–1450.

[56] Almlöf, J.; Taylor, P. R. General contraction of Gaussian basis sets. I.Atomic natural orbitals for first- and second-row atoms. *J. Chem. Phys.* **1987**, *86*, 4070–4077.

[57] McCaslin, L.; Stanton, J. Calculation of fundamental frequencies for small polyatomic molecules: a comparison etween correlation consistent and atomic natural orbital basis sets. *Mol. Phys.* **2013**, *111*, 1492–1496.

[58] East, A. L.; Allen, W. D. The heat of formation of NCO. *J. Chem. Phys.* **1993**, *99*, 4638–4650.

[59] Császár, A. G.; Allen, W. D.; Schaefer, H. F. In pursuit of the ab initio limit for conformational energy prototypes. *J. Chem. Phys.* **1998**, *108*, 9751–9764.

[60] Schuurman, M. S.; Muir, S. R.; Allen, W. D.; Schaefer, H. F. Toward subchemical accuracy in computational thermochemistry: Focal point analysis of the heat of formation of NCO and [H, N, C, O] isomers. *J. Chem. Phys.* **2004**, *120*, 11586–11599.

[61] Dunning, T. H. Gaussian basis sets for use in correlated molecular calculations. I. The atoms boron through neon and hydrogen. *J. Chem. Phys.* **1989**, *90*, 1007–1023.

[62] Feller, D. The use of systematic sequences of wave functions for estimating the complete basis set, full configuration interaction limit in water. *J. Chem. Phys.* **1993**, *98*, 7059–7071.

[63] Helgaker, T.; Klopper, W.; Kock, H.; Noga, J. Basis-set convergence of correlated calculations on water. *J. Chem. Phys.* **1997**, *106*, 9639–9646.

[64] Peterson, K. A.; Dunning, T. H. Accurate correlation consistent basis sets for

molecular core-valence correlation effects: The second row atoms Al-Ar, and the first row atoms B-Ne revisited. *J. Chem. Phys.* **2002**, *117*, 10548–10560.

[65] Sellers, H.; Pulay, P. The adiabatic correction to molecular potential surfaces in the SCF approximation. *Chem. Phys. Lett.* **1984**, *103*, 463–465.

[66] Handy, N.; Yamaguchi, Y.; Schaefer, H. F. The diagonal correction to the Born–Oppenheimer approximation: Its effect on the singlet–triplet splitting of CH2 and other molecular effects. *J. Chem. Phys.* **1986**, *84*, 4481–4484.

[67] Dyall, K. Interfacing relativistic and nonrelativistic methods. I. Normalized elimination of the small component in the modified Dirac equation. *J. Chem. Phys.* **1997**, *106*, 9618–9626.

[68] Kutzelnigg, W.; Liu, W. Quasirelativistic theory equivalent to fully relativistic theory. *J. Chem. Phys.* **2005**, *123*, 241102.

[69] Liu, W.; Peng, D. Infinite–order quasirelativistic density functional method based on the exact matrix quasirelativistic theory. *J. Chem. Phys.* **2006**, *125*, 044102.

[70] Iliaš, M.; Saue, T. An infinite–order two–component relativistic Hamiltonian by a simple one–step transformation. *J. Chem. Phys.* **2007**, *126*, 064102.

[71] Sikkema, J.; Visscher, L.; Saue, T.; Iliăs, M. The molecular mean-field approach for correlated relativistic calculations. *J. Chem. Phys.* **2009**, *131*, 124116.

[72] Liu, W.; Peng, D. Exact two-component Hamiltonians revisited. *J. Chem. Phys.* **2009**, *131*, 031104.

[73] Matthews, D. A. Analytic Gradients of Approximate Coupled Cluster Methods with Quadruple Excitations. *J. Chem. Theory Comput.* **2020**, *16*, 6195–6206.

[74] Parrish, R. M. et al. Psi4 1.1: An Open-Source Electronic Structure Program Emphasizing Automation, Advanced Libraries, and Interoperability. *J. Chem. Theory Comput.* **2017**, *13*, 3185–3197.

[75] Werner, H.-J.; Knowles, P. J.; Knizia, G.; Manby, F. R.; Schütz, M. Molpro: a general-purpose quantum chemistry program package. *WIREs Comput Mol Sci* **2012**, *2*, 242–253.

[76] Werner, H.-J. et al. MOLPRO, version 2019.2, a package of ab initio programs. 2019; see https://www.molpro.net.

[77] Stanton, J. F.; Gauss, J.; Cheng, L.; Harding, M. E.; Matthews, D. A.; Szalay, P. G. CFOUR, Coupled-Cluster techniques for Computational Chemistry, a quantum-chemical program package. With contributions from A.A. Auer, R.J. Bartlett, U. Benedikt, C. Berger, D.E. Bernholdt, Y.J. Bomble, O. Christiansen, F. Engel, R. Faber, M. Heckert, O. Heun, M. Hilgenberg, C. Huber, T.-C. Jagau, D. Jonsson, J. Jusélius, T. Kirsch, K. Klein, W.J. Lauderdale, F. Lipparini, T. Metzroth, L.A. Mück, D.P. O'Neill, D.R. Price, E. Prochnow, C. Puzzarini, K. Ruud, F. Schiffmann, W. Schwalbach, C. Simmons, S. Stopkowicz, A. Tajti, J. Vázquez, F. Wang, J.D. Watts and the integral packages MOLECULE (J. Almlöf and P.R. Taylor), PROPS (P.R. Taylor), ABACUS (T. Helgaker, H.J. Aa. Jensen, P. Jørgensen, and J. Olsen), and ECP routines by A. V. Mitin and C. van Wüllen. For the current version, see http://www.cfour.de.

[78] Matthews, D. A.; Cheng, L.; Harding, M.; Lipparini, F.; Stopkowicz, S.; Jagau, T.-C.; Szalay, P. G.; Gauss, J.; Stanton, J. Coupled-Cluster Techniques for Computational Chemistry: the CFOUR Program Package. *J. Chem. Phys.* **2020**, *152*, 214108.

[79] Laidler, K. J. *Pure Appl. Chem.* **1996**, *68*, 149–192.

[80] Laidler, K. J.; King, M. C. The Development of Transition–State Theory. *J. Phys. Chem.* **1983**, *87*, 2657–2664.

[81] Truhlar, D. G.; Garrett, B. C.; Klippenstein, S. J. The Current Status of Transition–State Theory. *J. Phys. Chem.* **1996**, *100*, 12771–12800.

[82] Johnston, H.; Heicklen, J. TUNNELLING CORRECTIONS FOR UNSYMMETRICAL ECKART POTENTIAL ENERGY BARRIERS. *J. Phys. Chem.* **1962**, *66*, 532–533.

[83] Mao, J.; Yu, F.; Zhang, Y.; An, J.; Wang, L.; Zheng, J.; Yao, L.; Luo, G.; Ma, W.; Yu, Q.; Huang, C.; Li, L.; Chen, L. High–resolution modeling of gaseous methylamines of a polluted regin in China: source-dependent emissions and implications of spatial variations. *Atmos. Chem. Phys.* **2018**, *18*, 7933–7950.

[84] Klapötke, T. M. New Nitrogen-Rich High Explosives. *Struct Bond* **2007**, *125*, 85–121.

[85] Hale, G. THE NITRATION OF HEXAMETHYLENETETRAMINE. *J. Am. Chem. Soc.* **1925**, *47*, 2754–2763.

[86] Nielsen, A. T.; Chafin, A. P.; Christian, S. L.; Moore, D. W.; Nadler, M. P.; Nissan, R. A.; Vanderah, D. J.; Gilardi, R. D.; George, C. F.; Flippen-Anderson, J. L. Synthesis of Polyazapolycyclic Caged Polynitramines. *Tetrahedron* **1998**, *54*, 11793–11812.

[87] Eaton, P. E.; Gilardi, R. L.; Zhang, M.-X. Polynitrocubanes: Advanced High-Density, High-Energy Materials. *Adv. Mater.* **2000**, *12*, 1143–1148.

[88] Giles, J. Collateral Damage. *Nature* **2004**, *427*, 580–581.

[89] Rahm, M.; Brinck, T. Kinetic Stability and Propelland Performance of Green Energetic Materials. *Chem. Eur. J.* **2010**, *16*, 6590–6600.

[90] Talawar, M.; Sivabalan, R.; Mukundan, T.; Muthurajan, H.; Sikder, A.; Gandhe, B.; Rao, A. S. Environmentally compatible next generation green energetic materials (GEMs). *J. Hazard. Mater* **2009**, *161*, 589–607.

[91] Singh, R.; an D. T. Meshri, R. V.; Shreeve, J. Energetic Nitrogen-Rich Salts and Ionic Liquids. *Angew. Chem. Int. Ed.* **2006**, *45*, 3584–3601.

[92] Trache, K.; Klapötke, T.; Maiz, L.; Abd-Elghany, M.; DuLuca, L. Recent advances in new oxidizers for solid rocket propulsion. *Green Chem.* **2017**, *19*, 4711–4736.

[93] Hiskey, M.; Goldman, N.; Stine, J. High=nitrogen energetic materials derived from azotetrazolate. *J. Energ. Mater.* **1998**, *16*, 119–127.

[94] Hantzsch, A. Ueber Diazoniumazide, Ar. N_5. *Ber. Dtsch. Chem. Ges.* **1903**, *36*, 2056–2058.

[95] Dimroth, O.; de Montmollin, G. Zur Kenntnis der Diazohydrazide. *Ber. Dtsch. Chem. Ges.* **1910**, *43*, 2904–2915.

[96] Lifschitz, J. Synthese der Pentazol-Verbindungen. *Ber. Dtsch. Chem. Ges.* **1915**, *48*, 410–420.

[97] Curtius, T.; Darapsky, A.; Müller, E. Die sogenannten Pentazol-Verbindungen von J. Lifschits. *Ber. Dtsch. Chem. Ges.* **1915**, *48*, 1614–1634.

[98] Huisgen, R.; Ugi, I. Zur Lösung eines klassischen Problems der organischen Stickstoff-Chemie. *Angew. Chem.* **1956**, *68*, 705–706.

[99] Butler, R.; Stephens, J.; Burke, L. First generation of pentazole (HN_5, pentazolic acid), the final azole, and a zinc pentazolate salt in solution: A new *N*-dearylation of 1-(*p*-methoxyphenyl) pyrazoles, a 2-(*p*-methoxyphenyl) tetrazole

and application of the methodology to 1-(*p*-methoxyphenyl) pentazole. *Chem. Commun.* **2003**, *3*, 1016–1017.

[100] Yang, Y.; Li, Y.; Zhang, R.; Sun, C.; Pang, S. Thermal stability of *p*-dimethylaminophenylpentazole. *RSC Adv.* **2014**, *4*, 57629–57634.

[101] Zhang, C.; Sun, C.; Hu, B.; Yu, C.; Lu, M. Synthesis and characterization of the pentazolate anion *cyclo*-N_5^- in $(N_5)_6(H_3O)_3(NH_4)_4Cl$. *Science* **2017**, *355*, 374–376.

[102] Xu, Y.; Wang, P.; Lin, Q.; Lu, M. A carbon-free inorganic-metal complex consisting of an all-nitrogen pentazole anion, a Zn(II) cation and H_2O. *Dalton Trans.* **2017**, *46*, 14088–14093.

[103] Sun, C.; Zhang, C.; Jiang, C.; Yang, C.; Du, Y.; Zhao, Y.; Hu, B.; Zheng, Z.; Christe, K. Synthesis of AgN_5 and its extended 3D energetic framework. *Nat. Commun.* **2018**, *9*, 1269.

[104] Bazanov, B.; Geiger, U.; Grinstein, D.; Welner, S.; Hass, Y. N_5^- in Solution: Isotopic Labeling and Further Details of Its Synthesis by Phenyl Pentazole Reduction. *J. Phys. Chem.* **2017**, *121*, 6727–6731.

[105] Frison, G.; G., J.; G., O. Guding the synthesis of pentazole derivatives and their mono- and di-oxides with quantum modeling. *New J. Chem.* **2013**, *37*, 611–618.

[106] Wang, Y.; Liu, Y.; Song, S.; Yang, Z.; Qi, X.; Wang, K.; Liu, Y.; Zhang, Q.; Tian, Y. Accelerating the discover of insensitive high-energy-density materials by a materials genome approach. *Nat. Commun.* **2018**, *9*, 2444.

[107] Perera, S. A.; Gregusova, A.; Bartlett, R. J. First Calculations of ^{1}5N-^{1}5N *J* Values and New Calculations of Chemical Shifts for High Nitrogen Systems: A

Comment on the Long Search for HN_5 and Its Pentazole Anion. *J. Phys. Chem. A* **2009**, *113*, 3197–3201.

[108] Burke, L. A.; Butler, R. N.; Stephens, J. C. Theoretical characterization of pentazole anion with metal counter ions. Calculated and experimental ^{1}5N shifts of aryldiazonium, -azide and -pentazole systems. *J. Chem. Soc., Perkin Trans.* **2001**, *2*, 1679–1684.

[109] Nguyen, M. T. Polynitrogen compounds 1. Structure and stability of N_4 and N_5 systems. *Coord. Chem. Rev.* **2003**, *244*, 93–113.

[110] Nguyen, M. T.; Ha, T. K. Decomposition mechanism of the polynitrogen N_5 and N_6 clusters and their ions. *Chem. Phys. Lett.* **2001**, *335*, 311–320.

[111] Yurtsever, E.; Calvo, F. Quantum Chemical View on the Growth Mechanims of Odd-Sized Nitrogen Cluster Anions. *J. of Phys. Chem. A* **2019**, *123*, 202–209.

[112] Perera, S. A.; Bartlett, R. J. Coupled-cluster calculations of Raman intensities and their application to N_4 and N_5^-. *Chem. Phys. Lett.* **1999**, *314*, 381–387.

[113] Hammerl, A.; Klapötke, T. M.; Schwerdtfeger, P. Azolylpentazoles as High-Energy Materials: A Computational Study. *Chem. Eur. J.* **2003**, *9*, 5511–5519.

[114] Pimienta, I. S.; Elzey, S.; Boatz, J. A.; Gordon, M. S. Pentazole-Based Energetic Ionic Liquids: A Computational Study. *J. of Phys. Chem. A* **2007**, *111*, 691–703.

[115] Davis, M.; Weidman, J.; Abbott, A.; Douberly, G. E.; Turney, J. M.; Schaefer, H. F. Characterization of the 2-methylvinoxy radical + O_2 reaction: A focal point analysis and composite multireference study. *J. Chem. Phys.* **2019**, *151*, 124302.

[116] Weidman, J. D.; Allen, R. T.; Moore, K. B.; Schaefer, H. F. High-level theoretical characterization of the vinoxy radical ($\bullet CH_2CHO$) + O_2 reaction. *J. Chem. Phys.* **2018**, *148*, 184308.

[117] Weidman, J. D.; Turney, J. M.; Schaefer, H. F. Energetics and mechanisms for the acetonyl radical + O_2 reaction: An important system for atmospheric and combustion chemistry. *J. Chem. Phys.* **2020**, *152*, 114301.

[118] Burke, L. A.; Fazen, P. J. Correlation Analysis of the Interconversion and Nitrogen Loss Reactions of Aryl Pentazenes and Pentazoles Derived from Aryl Diazonium and Azide Ions. *Int. J. Quantum Chem.* **2009**, *109*, 3613–3618.

[119] Bo, X. X.; Zheng, H. F.; Xin, J. F.; Ding, Y. H. A kinetically persistent isomer found for petnazole: a global potential energy surface survey. *Chem. Commun.* **2019**, *55*, 2597–2600.

[120] Bo, X.; Dong, Z.; Ding, Y. Arylpentazoles with surprisingly high kinetic stability. *Chem. Commun.* **2021**, *57*, 5310–5313.

[121] Kendall, R. A.; Dunning, T. H.; Harrison, R. J. Electron affinities of the first-row atoms revisited. Systematic basis sets and wave functions. *J. Chem. Phys.* **1992**, *96*, 6796–6806.

[122] Peterson, K. A.; Dunning, T. H. Accurate correlation consistent basis sets for molecular core-valence correlation effects: The second row atoms Al-Ar, and the first row atoms B-Ne revisited. *J. Chem. Phys.* **2002**, *117*, 10548–10560.

[123] Denis, P. A. Coupled cluster, B2PLYP and MO6-2X investigation of the thermochemistry of five-membered nitrogen containing heterocycles, furan, and thiophene. *Theor. Chem. Acc.* **2011**, *129*, 219–227.

[124] Neese, F. The ORCA program system. *Wiley Interdiscip. Rev.: Comput. Mol. Sci.* **2012**, *2*, 73–78.

[125] Neese, F. Software update: the ORCA porgram system, version 4.0. *Wiley Interdiscip. Rev.: Comput. Mol. Sci.* **2017**, *8*, 31327.

[126] Glendening, E. D.; J, K. B.; Reed, A. E.; Carpenter, J. E.; Bohmann, J. A.; Morales, C. M.; Karafiloglou, P.; Landis, C. R.; Weinhold, F. NBO 7.0. 2018.

[127] Downs, A. J.; Pulham, C. R. The hydrides of aluminium, gallium, indium, and thallium: a re-evaluation. *Chem. Soc. Rev.* **1994**, *23*, 175–184.

[128] Aldridge, S.; Downs, A. J. Hydrides of the Main-Group Metals: New Variations on an Old Theme. *Chem. Rev.* **2001**, *101*, 3305–3365.

[129] Kubas, G. J. Molecular Hydrogen Complexes: Coordination of a σ Bond to Transition Metals. *Amer. Chem. Soc.* **1988**, *28*, 120–128.

[130] Crabtree, R. H.; Hamilton, D. G. H-H, C-H, and Related Sigma-Bonded Groups as Ligands. *Adv. Organomet. Chem.* **1988**, *28*, 299–338.

[131] Crabtree, R. H. Dihydrogen complexes: some structural and chemical studies. *Accounts Chem. Res.* **1990**, *23*, 95–101.

[132] Jessop, P. G.; Morris, R. H. Reactions of transition metal dihydrogen complexes. *Coordin. Chem. Rev.* **1992**, *121*, 155–284.

[133] Heinekey, D. M.; Oldham, W. J. Coordination chemistry of dihydrogen. *Chem. Rev.* **1993**, *93*, 913–926.

[134] Crabtree, R. H. Transition Metal Complexation of σ Bonds. *Angew. Chem. Int. Edit.* **1993**, *32*, 789–805.

[135] Morris, R. H. 1995 Alcan Award Lecture New intermediates in the homolytic and heterolytic splitting of dihydrogen. *Can. J. Chem.* **1996**, *74*, 1907–1915.

[136] Esteruelas, M. A.; Oro, L. A. Dihydrogen Complexes as Homogeneous Reduction Catalysts. *Chem. Rev.* **1998**, *98*, 577–588.

[137] Sabo-Etienne, S.; Chaudret, B. Quantum Mechanical Exchange Coupling in Polyhydride and Dihydrogen Complexes. *Chem. Rev.* **1998**, *98*, 2077–2092.

[138] Stephens, J. C.; Bolton, E. E.; Schaefer, H. F.; Andrews, L. Quantum mechanical frequencies and matrix assignments to Al2H2. *J. Chem. Phys.* **1997**, *107*, 119–123.

[139] Palagyi, Z.; Grev, R. S.; Schaefer, H. F. Striking similarities between elementary silicon and aluminum compounds: monobridged, dibridged, trans-bent, and vinylidene isomers of aluminum hydride (Al2H2). *J. Am. Chem. Soc.* **1993**, *115*, 1936–1943.

[140] Palagyi, Z.; Schaefer, H. F.; Kapuy, E. Ga2H2: planar dibridged, vinylidene-like, monobridged, and trans equilibrium geometries. *Chem. Phys. Lett.* **1993**, *203*, 195 – 200.

[141] Wiberg, E.; Dittmann, O. *Z. Naturforsch B* **1957**, *12*, 57–58.

[142] Breisacher, P.; Siegel, B. Comparative Stabilities of Gaseous Alane, Gallane, and Indane. *J. Am. Chem. Soc.* **1965**, *87*, 4255–4258.

[143] Schriver, D. F.; Parry, R. W.; Greenwood, N. N.; Storr, A.; Wallbridge, M. G. H. Some Observations Relative to Digallane. *Inorg. Chem.* **1963**, *2*, 867–868.

[144] Greenwood, N.; Wallbridge, M. G. H. *J. Chem. Soc.* **1963**, *7*, 3912–3913.

[145] Hunt, P.; Schwerdtfeger, P. Are the Compounds InH3 and TlH3 Stable Gas Phase or Solid State Species? *Inorg. Chem.* **1996**, *35*, 2085–2088.

[146] Himmel, H.-J.; Manceron, L.; Downs, A. J.; Pullumbi, P. Formation and Characterization of the Gallium and Indium Subhydride Molecules Ga2H2 and In2H2: A Matrix Isolation Study. *J. Am. Chem. Soc.* **2002**, *124*, 4448–4457.

[147] Himmel, H.-J.; Manceron, L.; Downs, A. J.; Pullumbi, P. Characterization and Photochemistry of the Gallium and Indium Subhydrides Ga2H2 and In2H2. *Angew. Chem. Int. Ed.* **2002**, *41*, 796–799.

[148] Wang, X.; Andrews, L. Infrared Spectra of Indium Hydrides in Solid Hydrogen and Neon. *J. Phys. Chem. A* **2004**, *108*, 4440–4448.

[149] Andrews, L.; Wang, X. Infrared Spectra of Indium Hydrides in Solid Hydrogen and of Solid Indane. *Angew. Chem. Int. Ed.* **2004**, *43*, 1706–1709.

[150] Treboux, G.; Barthelat, J. C. X-X direct bonds versus bridged structures in group 13 X2H2 potential energy surfaces. *J. Amer. Chem. Soc.* **1993**, *115*, 4870–4878.

[151] Moc, J.; Wierzejewska, M. Interconversion of Singlet Indium Subhydride Isomers: Theoretical Study. *Internet Electronic J. Mol. Design* **2004**, *3*, 1–10.

[152] Pritchard, B. P.; Altarawy, D.; Didier, B.; Gibsom, T. D.; Windus, T. L. A New Basis Set Exchange: An Open, Up-to-date Resource for the Molecular Sciences Community. *J. Chem. Inf. Model.* **2019**, *59*, 4814–4820.

[153] Feller, D. The role of databases in support of computational chemistry calculations. *J. Comput. Chem.* **1996**, *17*, 1571–1586.

[154] Schuchardt, K. L.; Didier, B. T.; Elsethagen, T.; Sun, L.; Gurumoorthi, V.; Chase, J.; Li, J.; Windus, T. L. Basis Set Exchange: A Community Database for Computational Sciences. *J. Chem. Inf. Model.* **2007**, *47*, 1045–1052.

[155] Metz, B.; Stoll, H.; Dolg, M. Small-core multiconfiguration-Dirac-Hartree-Fock-adjusted pseudopotentials for post-d main group elements: Application to PbH and PbO. *J. Chem. Phys.* **2000**, *113*, 2563–2569.

[156] Peterson, K. A. Systematically convergent basis sets with relativistic pseudopotentials. I. Correlation consistent basis sets for the post-d group 13-15 elements. *J. Chem. Phys.* **2003**, *119*, 11099–11112.

[157] Peterson, K. A.; Yousaf, K. E. Molecular core-valence correlation effects involving the post-d elements Ga-Rn: Benchmarks and new pseudopotential-based correlation consistent basis sets. *J. Chem. Phys.* **2010**, *133*, 174116.

[158] Mills, I. In *Molecular Spectroscopy: Modern Research*; Rao, K. N., Matthews, C. W., Eds.; Academic Press, 1972; Vol. II; Chapter 1, pp 115–140.

[159] Rosnik, A. M.; Polik, W. F. VPT2+K spectroscopic constants and matrix elements of the transformed vibrational Hamiltonian of a polyatomic molecule with resonances using Van Vleck perturbation theory. *Mol. Phys.* **2014**, *112*, 261–300.

[160] Franke, P. R.; Stanton, J. F.; Douberly, G. E. How to VPT2: Accurate and Intuitive Simulations of CH Stretching Infrared Spectra Using VPT2+K with Large Effective Hamiltonian Resonance Treatments. *J. Phys. Chem. A* **2021**, *125*, 1301–1324.

[161] Császár, A. G.; Allen, W. D.; Schaefer, H. F. In pursuit of the ab initio limit for conformational energy prototypes. *J. Chem. Phys.* **1998**, *108*, 9751–9764.

[162] Schuurman, M. S.; Muir, S. R.; Allen, W. D.; Schaefer, H. F. Toward subchemical accuracy in computational thermochemistry: Focal point analysis of the

heat of formation of NCO and [H,N,C,O] isomers. *J. Chem. Phys.* **2004**, *120*, 11586–11599.

[163] Feller, D. The use of systematic sequences of wave functions for estimating the complete basis set, full configuration interaction limit in water. *J. Chem. Phys.* **1993**, *98*, 7059–7071.

[164] Helgaker, T.; Klopper, W.; Koch, H.; Noga, J. Basis-set convergence of correlated calculations on water. *J. Chem. Phys.* **1997**, *106*, 9639–9646.

[165] Herzberg, G. *Molecular Spectra and Molecular Structure*, 2nd ed.; Van Nostrand Reinhold Company: New York, 1950.

[166] Dudley, T. J.; Gordon, M. S. Theoretical study of the formation and isomerization of Al2H2. *Mol. Phys.* **2006**, *104*, 751–762.

[167] Martin, J. M. L.; Lee, T. J.; Taylor, P. R.; François, J. The anharmonic force field of ethylene, C2H4, by means of accurate ab initio calculations. *J. Chem. Phys.* **1995**, *103*, 2589–2602.

[168] Ault, B. S.; Steinback, E.; Pimentel, G. C. *The Journal of Physical Chemistry* **1975**, *79*, 615–620.

[169] Roscioli, J. R.; McCunn, L. R.; Johnson, M. A. *Science* **2007**, *316*, 249–254.